



Doctoral Thesis

Integrated Structural Monitoring using Point Clouds Obtained from Terrestrial Laser Scanning

Author(s):

Serantoni, Eugenio

Publication Date:

2020

Permanent Link:

<https://doi.org/10.3929/ethz-b-000418873> →

Rights / License:

[In Copyright - Non-Commercial Use Permitted](#) →

This page was generated automatically upon download from the [ETH Zurich Research Collection](#). For more information please consult the [Terms of use](#).

DISS. ETH No. 26773

INTEGRATED STRUCTURAL MONITORING USING
POINT CLOUDS OBTAINED FROM TERRESTRIAL
LASER SCANNING

A dissertation submitted to attain the degree of
DOCTOR OF SCIENCES OF ETH ZÜRICH
(DR. SC. ETH ZÜRICH)

presented by

EUGENIO SERANTONI
M.SC. ETH ZÜRICH
M.SC. ALMA MATER STUDIORUM - UNIVERSITÀ DI BOLOGNA

BORN ON 20.04.1989
CITIZEN OF ITALY

accepted on the recommendation of

Prof. Dr. A. Wieser, examiner
Prof. Dr. E. Chatzi, co-examiner
Prof. Ing. L. Vittuari, co-examiner

2020

Contents

Abstract	iii
Zusammenfassung	v
Riassunto	vii
Acknowledgements	ix
1 Introduction	1
1.1 Motivation and relevance	1
1.2 State of the art	4
1.3 Objectives	5
1.4 Thesis outline	6
2 Background	9
2.1 Terrestrial Laser Scanning	9
2.1.1 How TLS works	9
2.1.2 TLS error modelling	10
2.1.3 Registration of point clouds	13
2.1.4 Monitoring with TLS	14
2.2 Finite Element Method	15
3 From TLS data to material parameters	19
3.1 Workflow	20
3.2 FE model generation	22
3.3 Interpolation of nodal displacements and their covariances	26
3.3.1 Variance propagation	34
3.3.2 Log-Euclidean interpolation of the VCM	37
3.3.3 Nearest neighbour interpolation	38
3.3.4 Comparison of the interpolation approaches	38
3.4 Estimation of parameters	42
3.4.1 Integrated monitoring	42
3.4.2 Pre-elimination	47
3.4.3 Partitioning of the structure	49
3.4.4 Closed-loop validation	49
3.4.5 Monte Carlo validation	57
3.5 Considerations on calculations	59
3.5.1 Description of the Jacobian \mathbf{A}_p	59

3.5.2	Numerical precision of the Abaqus output files	61
3.5.3	Step size for the numerical derivatives of a non-linear function	62
3.5.4	Precision of the LSA implementation	64
4	Application cases	67
4.1	Numerical simulation tool	68
4.2	Simulated simply supported beam	70
4.2.1	Results for a single sensor location	72
4.2.2	Results for multiple sensor locations	75
4.3	Simulated corner-supported plate	82
4.3.1	Results	83
4.4	Cross-laminated timber slab	91
4.4.1	Modelling	91
4.4.2	Measurements	93
4.4.3	Analysis	95
4.4.4	Results for a single partition	96
4.4.5	Results for multiple partitions	99
5	Conclusion and outlook	105
A	Acronyms	109
	List of Figures	111
	List of Tables	114
	Bibliography	116
	Curriculum Vitae	129

Abstract

Terrestrial laser scanning (TLS) technology is by now a mature and widespread geodetic measurement technique, and the accuracy of the commercially available scanners is steadily increasing. TLS is particularly suitable for the task of areal deformation analysis and, despite its popular use for the tasks of structural monitoring, no consistent workflow for structural identification has been yet defined. For this reason, this thesis contributes towards the automatic determination of the material properties of structures modelled and monitored via point cloud technologies. It results in an interdisciplinary work that touches both the fields of geodetic and structural engineering, and forms part of the discipline of structural health monitoring (SHM), which plays a key role in the current engineering practice.

The main contribution of this thesis is a novel method to perform the numerical identification of structural members by using point cloud data acquired with terrestrial laser scanners in multiple epochs. The backbone of the developed method is the approach of integrated monitoring, which offers a great flexibility to merge measurements of different origins within a single framework relying on the finite element (FE) modelling of the investigated structure. The underlying criterion of this approach is to match the measured and the FE-calculated displacements by using a least squares adjustment (LSA), which includes the linearisation of the mentioned FE model. In this way, a thorough propagation of the stochastic information from the TLS data to the final estimated parameters can also be performed. The LSA is herein validated with closed-loop and Monte Carlo simulations. Additionally, a method to automatically generate the geometry of the FE model from the point cloud of the surface of the monitored object is proposed, and specific insights about the implementation of the numerical differentiation are provided.

Moreover, the observed nodal displacements and their uncertainties are derived from the TLS-based deformation analysis of the structure. Among others, this step can be carried out with three different methods: variance propagation, log-Euclidean interpolation, and nearest neighbour search. Despite being all applicable methods, the third one has proven more computationally efficient.

The method is herein implemented for the model update of beams and slabs for which the Young's modulus is estimated, with the possibility to subdivide the analysed structure in multiple partitions. Moreover, the proposed method can be readily used to estimate other material parameters or even forces, for any shape of structure, including free-form ones.

The proposed method is herein analysed and successfully employed for three application cases, of which one with real data and two with synthetically generated point clouds: a cross-laminated timber slab, a steel beam, and an alloy plate. The observations for the application cases relying on synthetic data have been generated with a self-developed point cloud generator. This generator has also been embedded

in a tool that enables the planning of TLS monitoring campaigns by predicting the influence of the sensor setup (position, resolution and accuracy) on the estimated parameters. Ultimately, the developed method successfully expands the range of capabilities of TLS, by defining an operational procedure for the numerical identification of structures.

Zusammenfassung

Das terrestrische Laserscanning (TLS) ist heute eine ausgereifte und weit verbreitete geodätische Messtechnik, und die Genauigkeit der kommerziell erhältlichen Scanner nimmt ständig zu. TLS eignet sich besonders für die Aufgabe der flächenhaften Deformationsanalyse. Trotz seiner weit verbreiteten Anwendung für die Aufgaben der Bauwerksüberwachung ist noch kein einheitlicher Verfahrensablauf für die Bauwerksidentifikation definiert worden. Aus diesem Grund trägt diese Arbeit zur automatischen Bestimmung der Materialeigenschaften von Strukturen bei, die mittels Punktwolgentechnologien modelliert und überwacht werden. Es ist eine interdisziplinäre Arbeit, die sowohl die Bereiche der Geodäsie als auch die des Bauingenieurwesens betrifft und Teil der Disziplin des Structural Health Monitoring (SHM) ist, das in der aktuellen Ingenieurpraxis eine Schlüsselrolle spielt.

Der Hauptbeitrag dieser Arbeit ist ein neuartiges Verfahren zur numerischen Identifikation von Bauwerken unter Verwendung von Punktwolkendaten, die mit terrestrischen Laserscannern in mehreren Epochen erfasst wurden. Der Hauptstrang der entwickelten Methode ist der Ansatz des integrierten Monitorings, das eine grosse Flexibilität bietet, um Messungen unterschiedlicher Herkunft in einem einzigen Modellrahmen zusammenzuführen, welcher auf der Finite-Elemente (FE)-Modellierung der untersuchten Struktur basiert. Das zugrundeliegende Kriterium dieses Ansatzes ist die Anpassung der gemessenen und der FE-berechneten Verschiebungen durch die Verwendung einer Ausgleichsrechnung nach der Methode der kleinsten Quadrate, die die Linearisierung des erwähnten FE-Modells einschliesst. Auf diese Weise kann auch eine gründliche Fortpflanzung der stochastischen Informationen aus den TLS-Daten zu den geschätzten Endparametern durchgeführt werden. Die Ausgleichsrechnung wird hier mit Closed-Loop- und Monte-Carlo-Simulationen validiert. Zusätzlich wird eine Methode zur automatischen Generierung der Geometrie des FE-Modells aus der Punktwolke der Oberfläche des überwachten Objekts vorgeschlagen. Ausserdem werden spezifische Erkenntnisse über die Implementierung der numerischen Ableitung geliefert.

Darüber hinaus werden die beobachteten Knotenverschiebungen und deren Unsicherheiten aus der TLS-basierten Deformationsanalyse der Struktur abgeleitet. Dieser Schritt kann unter anderem mit drei verschiedenen Methoden durchgeführt werden: Varianzfortpflanzung, logarithmisch-euklidische Interpolation und Suche nach dem nächsten Nachbarn. Obwohl alle Methoden anwendbar sind, hat sich die dritte Methode als rechnerisch effizienter erwiesen.

Die Methode wird hier für die Modell-Aufdatierung von Balken und Platten implementiert, deren Elastizitätsmodul mit der Möglichkeit, die analysierte Struktur in mehrere Partitionen zu unterteilen, geschätzt wird. Ausserdem kann die vorgeschlagene Methode leicht zur Schätzung anderer Materialparameter oder sogar Kräfte für jede Form der Struktur, einschliesslich Freiformstrukturen, verwendet werden.

Die vorgeschlagene Methode wird hier analysiert und erfolgreich für drei Anwendungsfälle eingesetzt, für einen mit realen Daten und für zwei mit synthetisch erzeugten Punktwolken: eine Brettsperrholzplatte, ein Stahlträger und eine legierte Platte. Die Beobachtungen für die Anwendungsfälle, die sich auf synthetische Daten stützen, wurden mit einem selbstentwickelten Punktwolkengenerator erzeugt. Dieser Generator wurde auch in ein Werkzeug eingebettet, das die Planung von TLS-Überwachungskampagnen ermöglicht, indem der Einfluss der Sensoranordnung (Position, Auflösung und Genauigkeit) auf die geschätzten Parameter vorhergesagt wird. Letztendlich erweitert die entwickelte Methode erfolgreich das Leistungsspektrum von TLS, indem sie ein operationelles Verfahren für die numerische Identifizierung von Strukturen definiert.

Riassunto

Il laser scanning terrestre (TLS) è una tecnica di misura geodetica ormai matura e diffusa, e la precisione degli scanner attualmente disponibili in commercio è in costante aumento. Il TLS è particolarmente adatto per eseguire analisi delle deformazioni di superfici. Tuttavia, nonostante il suo largo uso per i compiti di monitoraggio strutturale, non esiste ancora una procedura condivisa per i fini dell'identificazione strutturale. Pertanto, questa tesi fornisce un contributo verso l'automatizzazione della stima delle proprietà dei materiali di strutture modellate e monitorate mediante l'acquisizione di nuvole di punti. Questo è dunque un lavoro interdisciplinare, che connette i campi dell'ingegneria geodetica e strutturale, e che si colloca nella disciplina del monitoraggio strutturale, il quale è divenuto centrale nella pratica ingegneristica odierna.

Il principale contributo di questa tesi è un nuovo metodo per condurre l'identificazione numerica di strutture grazie all'uso di nuvole di punti acquisite in più epoche. Il fulcro del metodo sviluppato è l'approccio del monitoraggio integrato, che offre una grande flessibilità nel combinare misure di diversa origine all'interno di un unico processo, basandosi sulla modellazione agli elementi finiti (FE) della struttura indagata. Il criterio di base di questo approccio è la corrispondenza fra gli spostamenti misurati e gli spostamenti calcolati dal modello FE, utilizzando una compensazione ai minimi quadrati che include la linearizzazione del modello FE stesso. In questo modo è possibile propagare le incertezze dalle osservazioni effettuate col laser scanner fino ai parametri stimati. In questo lavoro, la compensazione è stata validata con simulazioni e col metodo Monte Carlo. Inoltre, è stato anche sviluppato un metodo per la generazione automatica della geometria del modello FE, a partire dalla nuvola di punti che rappresenta la superficie dell'oggetto monitorato. In aggiunta, vengono fornite indicazioni riguardo l'implementazione della derivazione numerica del modello FE.

Gli spostamenti nodali osservati e le loro incertezze sono ricavati dai dati TLS, grazie ad una analisi delle deformazioni. In particolare, questo compito può essere eseguito con tre diversi metodi: la propagazione della varianza, l'interpolazione log-Euclidea, e la ricerca *nearest neighbour*. Nonostante siano tutti questi tre metodi accettabili e funzionali, il terzo si dimostra superiore per la sua efficienza computazionale.

Questa tesi presenta l'implementazione della stima del modulo di Young per travi e piastre, con la possibilità di suddividere le strutture analizzate in più partizioni. Inoltre, il metodo è potenzialmente in grado di stimare altre proprietà meccaniche e forze applicate, anche per strutture a forma libera. Il metodo proposto viene qui analizzato e utilizzato con successo per tre casi applicativi: una trave in acciaio e una piastra in lega di alluminio le cui nuvole di punti sono state generate sinteticamente, ed una lastra in legno X-LAM monitorata nella realtà. Per quanto riguarda i casi applicativi che hanno previsto l'uso dati sintetici, è stato sviluppato un ge-

neratore di nuvole di punti, il quale è stato anche incorporato in uno strumento in grado di prevedere l'influenza delle impostazioni dello scanner (posizione, risoluzione e precisione) sui parametri stimati, utile per la pianificazione di campagne di monitoraggio TLS. In definitiva, questa tesi allarga il campo di applicazione del TLS, definendo una procedura operativa per l'identificazione strutturale a partire da nuvole di punti.

Acknowledgements

Hereby I would like to express my gratitude to all the people who encouraged and supported me during my doctoral studies.

My first thanks are for my thesis supervisor Prof. Dr. Andreas Wieser, for his support in any moment of need and for the opportunity he gave me to research in the field I desired, letting me bridge the two main fields on which I focused during my graduate studies. His constructive inputs, his rigorous feedback, and the freedom he granted me, made this work possible.

Furthermore, I would like to thank the co-examiners of my thesis, Prof. Dr. Eleni Chatzi, and Prof. Luca Vittuari for their careful reading of the thesis and for the interest in the subject they sparked in me, well before starting this PhD.

I also thank Prof. Dr. Konrad Schindler and Prof. Dr. Werner Lienhart, who provided me valuable observations and hints.

Furthermore, I would like to thank all my present and former colleagues at the Institute of Geodesy and Photogrammetry, and in particular at the Chair of Geosensors and Engineering Geodesy, who taught me something new every day, sparked interesting discussions, and listened to my doubts. I am proud to have been part of such a strong group. Particularly many thanks to Dr. Geo Boffi, Valens Frangez, Zan Gojcic, Pabitra Ray, Dr. David Salido-Monzú, Lorenz Schmid, and Dr. Caifa Zhou, for the very helpful proof-reading of this work.

A special thanks goes also to the researchers who shared a little of road with me during this PhD: Dr. Rosalba Ferrari, Marcel Muster, Dr. Ilenia Selvaggi. They are among the most enthusiastic and hard-working researchers I ever met.

I would also like to thank the technical and administrative personnel of the Institute of Geodesy and Photogrammetry for the punctual help, and the students Flurin Weber, Yang Xu, Benjamin Kramis, and Felix Piringer, who helped during some of the measurements.

A great thanks is also deserved to my friends (they are probably too many to be listed here) who motivated me and made me feel at home in Zurich since I arrived, and they made my time pass by very quickly.

Lastly, I am deeply grateful to my parents Mariarosa and Gabriele, who always supported me unconditionally, and to Sofia, who is the most positive person I know; living besides her is a reason of true joy.

1. Introduction

1.1. Motivation and relevance

As we live in the information age, the decision-making processes are driven by the knowledge and insight into the technological systems, and this holds for systems such as civil structures and infrastructures as well. In order to ensure safety and minimise the economical consequences of the undesired, yet inevitable, degradation of the built heritage, engineers should not merely react to failures, posing users and stakeholders at the mercy of extreme or catastrophic events. Instead, engineers should try to work proactively, mainly by continuously monitoring the present integrity and condition of the industrial and civil structures and infrastructures that are most critical for the citizenry. Undertaking the monitoring of civil structures and infrastructures enables to design, plan and implement maintenance measures, regulate their use according to their capacity limits, and inform the users in case of foreseen or current service disruptions. Within the engineering community, the discipline dealing with these issues is structural health monitoring (SHM). The realm of SHM is quite vast and is defined as "the process of implementing a damage identification strategy for aerospace, civil, and mechanical engineering infrastructure" (Worden et al., 2007, p. 1639). In this context, the term *identification* implies the derivation of a model of the physical system by using experimental data.

This work represents a step towards the automation of SHM with terrestrial laser scanning (TLS) data, i.e. an extension of deformation monitoring with TLS data to the direct estimation of structural parameters of the investigated structures. Since it is important to provide herein adequate context about the intended relevance of this work, the rest of this chapter describes the three main arguments behind the definition of the scope of this work.

The first motivation is the awareness that the construction industry is arguably the industry sector that underwent the least innovation in the last century. Of course, innovation is a concept difficult to quantify. However, higher productivity is the main expected effect of the introduction of innovative processes and solutions, and the historical lagging of the productivity of the construction industry with respect to other industries has been recorded for many decades. In fact, figs. 1.1 and 1.2 strikingly show that in the UK and in the USA, despite a steadily increasing trend of the overall productivity, the various economical sectors exhibited mixed perform-

Gross value added per hour worked, constant prices
Index: 100 = 1947

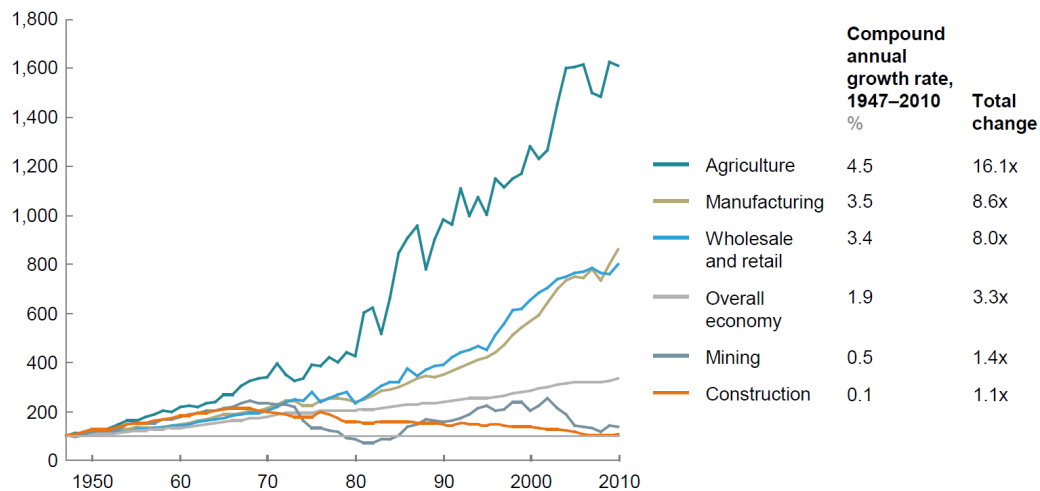


Figure 1.1: Historical productivity in the United States of America, 1947-2010, Source: McKinsey Global Institute (2017)

ances. In particular, the sectors of manufacturing and agriculture experienced the largest increase in productivity starting from the 1970s on, while the construction and mining industries did not keep the same pace. Indeed, the most impressive technological advancements of the last three decades (i.e. the pillars of the third industrial revolution, such as biotechnology, computer science, telecommunications, and robotics) affected the building industry only indirectly. For example, the concrete casting process has substantially remained the same for several decades now.

Researchers, investors, and regulators are aware of this sectorial gap in innovation and production, and direct considerable efforts towards its reduction. Thus, in the last few years the research community has been aiming for the automated construction of automatically computer-aided designed structures (Dunn, 2012). Consequently, the field of architecture is revolutionising with comprehensive free-form designs, computer-generated shapes, and delivering higher geometrically complex final products for a reduced cost. This would indeed represent a revival of free-form architectural geometries within the field of civil engineering, because engineers of the last century such as Pier Luigi Nervi and Sergio Musumeci were already optimising the design of their structures by placing materials following the isostatic lines (Bucur-Horváth and Saplacan, 2013; Neri, 2012). This way of thinking is being revived under the new name of graphic design by contemporary engineers (see Beghini et al., 2014; Oval et al., 2019). The main drive of these changes in design criteria is the economic convenience of the associated building techniques. Until the 1960's the labour work force was cheaper as opposed to the material cost. Thus, it was convenient to dedicate a larger on-site manual workforce to create complex formworks thereby reducing the total incurred cost. In the second half of the 20th century instead, the relatively cheaper installation of the pre-fabricated structural

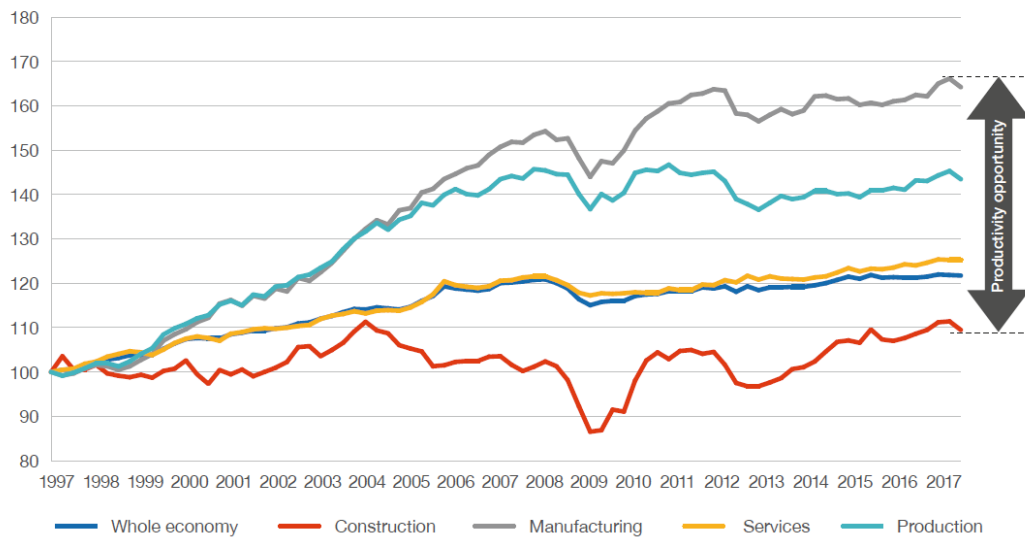


Figure 1.2: Historical productivity per worker (Index: 100=1997) in various economic sectors in the United Kingdom, 1997-2017, Source: UK Infrastructure and Projects Authority (2017)

elements and the delivery of standard-sized formworks made the use of repetitive and prismatic elements more practical. Nowadays, when building free-form structures, individual structural members are machine-produced in industrial production plants and subsequently assembled on site. In the future, it is reasonable to expect that a higher level of automation will be brought to the construction site, where robotic machinery will directly assemble and build complex structures. This will mark a big shift in the construction industry. Although robotic fabrication is a big and promising theme in research (Wangler et al., 2016), it is still expected to evolve as a more widespread technology over the next decades. For these reasons, the development of measurement techniques for the geometric monitoring of free-form objects will soon be requested by the construction industry, along with the analytical methods to automatically evaluate and assess the condition of such structures.

Another reason behind the choice of the topic is the pressing issue of ageing and deteriorating infrastructure. Indeed, the need for structural health monitoring is growing in a large part of the developed world (i.e. Europe, North America, and Japan), which experienced a large infrastructural development after the second world war and now requires major maintenance and restoration of a large part of its infrastructure.

The third strong trend that has been considered is the tremendous advancement of the available computational power, which is steadily enlarging the realm of numerical simulations of natural phenomena. In particular, a reasonable approach to get advantage of the availability of computational power is to leave the repetitive and quantitative tasks to computers, while focusing on creative tasks, such as the choice and control of the input data, and the analysis and interpretation of the results. Co-

herent with this approach, and together with the increasing availability of automatic optical measurement systems, the process of structural identification should be then transition to single manual measurements and analytic modelling into multiple automatically gathered and classified contact-less measurements (e.g. TLS), numerical modelling, and eventually to the automated interpretation of the measurements.

1.2. State of the art

A visible trend in the engineering disciplines is their progressively increasing specialisation and compartmentalisation, accompanied by the apparently contrasting overlap and convergence of the underlying mathematical methods. This thesis presents an interdisciplinary research, as different fields of engineering have been connected, namely engineering geodesy and structural engineering. Indeed, this work consists of merging and integrating several existing tools belonging to different disciplines, and demonstrating what is technically feasible in the present state-of-the-art, and it is driven by the ambition to present a small but significant contribution in each of the two subjects.

TLS is a ground-based, active sensing technology able to acquire dense 3D point clouds of opaque object surfaces, and this thesis focuses on its use for static measurements for SHM. However, it is important to note that a major branch of SHM consists in the monitoring of dynamic properties of structures i.e. stiffness-related vibration modes and frequencies (Deraemaeker and Worden, 2010; Ou et al., 2017; An et al., 2019). In fact, historically, SHM has been predominantly developed for the vibration-based damage assessment (Farrar and Worden, 2007) of the effects of phenomena such as fatigue, wear and impacts. Indeed, the applications fields of SHM are multiple, primarily including the safety control and the maintenance planning of industrial machinery and aerospace, automotive, and civil structures.

Moreover, structural monitoring can be performed with several alternative contact-less measurement systems, i.e. with geodetic sensors such as image-assisted total stations (Ehrhart, 2017), or with non-destructive techniques to assess the stiffness distribution in a body, such as by using ultrasonic or acoustic tomography (Alves et al., 2015; da Porto et al., 2003). For the periodical monitoring of extremely large structures, even satellite contactless solutions may also be viable. An extreme case is the monitoring of the Millennium Tower in San Francisco with InSAR (Desnos et al., 2017). Additionally, the sensor fusion of different contactless systems is also possible; for example, Wiedemann et al. (2017) integrated TLS and image data.

With a focus on TLS, its main applications in the geodetic field are the dimensional control (Wang et al., 2016a) and the deformation monitoring of both artificial (Sarti et al., 2009; Holst et al., 2019b; Adamson et al., 2020) and natural objects (Barbarella et al., 2017; Bienert, 2013). A more recent declination of this discipline is the parametric deformation monitoring, which is based on geometric objects such as basis splines (Schmitt et al., 2019; Harmening and Neuner, 2020) and non-uniform rational basis splines (NURBS) (Oreni et al., 2014a).

TLS is also largely used for the modelling of 3D geometries of complex technological systems such as buildings. In fact, point cloud-based acquisition methods are extremely popular for the definition of building information models (BIM). In this field, various applications have been tackled, such as the automatic generation of models (Jung et al., 2016; Tran et al., 2019), the digital preservation of cultural heritage and historic BIM (HBIM) (Oreni et al., 2014b; Antón et al., 2018; Brumana et al., 2018), and the inventory and recognition of architectural elements such as windows, doors, and furniture (Xiong et al., 2013; Valero et al., 2016). Still in connection with cultural heritage, several researchers have been also focusing on the forward modelling of the mechanical behaviour of historical masonry buildings (Barazzetti et al., 2015; Bitelli et al., 2018; Selvaggi, 2017; Selvaggi et al., 2018, 2019; Argiolas et al., 2019; Rolin et al., 2019).

Regarding other applications close to the fields of structural and construction engineering, Nguyen and Weinand (2019) performed a comparison between FE-generated deformations and TLS-measured ones, Pöchtrager et al. (2018) dealt with the reverse engineering of manufactured objects such as timber structures, and other authors investigated different structural elements, e.g. 2D facades (Truong-Hong et al., 2013) and vaults (Angjeliu et al., 2019). Other widespread uses of TLS in construction are the condition assessment of surfaces (Mukupu et al., 2017) and the damage inspection of cracks (Sánchez-Rodríguez et al., 2018). For a wider review on the use of point cloud data in construction, one can refer to (Wang and Kim, 2019)

Moving towards the specific topics treated in this thesis, other authors already devoted themselves to the structural numerical identification by integrating point clouds measurements and static finite elements (FE). For example, Riveiro et al. (2016) automatically extracted TLS-measured displacements and subsequently searched for the best parameters for a manually defined FEM to diagnose masonry arches, while Napolitano and Glisic (2019) diagnosed the most probable causes of cracks on masonry structures by using photogrammetric data. Other authors defined methods to analyse bent beams (Lee and Hyo, 2013; Yang et al., 2018; Riveiro et al., 2018), while Wu et al. (2016) proposed an approach which involves the direct inversion of the FE stiffness matrix. In addition, Jo et al. (2020) estimated the strains of a metallic plate by using a FE model to translate the out-of-plane displacements into in-plane strains.

1.3. Objectives

The aim of the present work is to develop an algorithm that combines the contactless areal monitoring of a free-form deformable structure and the numerical identification of its mechanical parameters, in the framework of an integrated deformation analysis, which is defined by Welsch (2003) as the determination of the geometrical changes (movements and distortions) of an object.

The rationale behind is maximising the use of TLS data for static SHM, by design-

ing and implementing the first method that integrates the steps of monitoring, modelling, and interpretation in a single workflow, in an attempt to exploit the spatial redundancy of the TLS point clouds.

The research questions can therefore be summarised as below:

- How can mechanical parameters of structural models be estimated using TLS areal measurements? What are the limitations?
- How to propagate the uncertainties of the scanning process to the estimated parameters?
- What is the influence of the scanner location and the scan resolution on the estimated values and their accuracy?
- How to assess if a structure is suited to be monitored with a given TLS measurement setup?

1.4. Thesis outline

This work is structured as follows.

In chapter 2, as this is an interdisciplinary project, the fundamentals of the disciplines touched by the proposed method (i.e. FEM and TLS) are provided. Regarding the TLS, special attention is given to the uncertainties involved in the acquisition of TLS point clouds, by explaining their sources and their modelling. The registration process, which is crucial in any TLS monitoring task, is also described, along with an overview of the advantage and disadvantages of TLS with respect to other remote sensing systems. As for the FEM, the basic terminology and the main underlying principles are provided.

Chapter 3 starts with a presentation of the overarching workflow of the developed method. Then, the single steps of the workflow are successively explained, beginning with the geometrical manipulations designed to convert a point cloud of the surface of the investigated structure into a FE mesh. Subsequently, three methods to interpolate the TLS-calculated displacements at the FE nodes are described and compared, in order to provide an indication about the advantages and disadvantages of each of them. Further, the integrated monitoring approach is presented in its general version, and then it is shaped to address the task of structural identification. Moreover, the integrated monitoring approach has also been modified to account for multiple partitions and for the pre-elimination of the nodes displacements that are not influenced by the measurements. Afterwards, the LSA and its output are validated by using closed-loop tests and a Monte Carlo experiment. Additionally, some insights and observations about the calculations are presented, thus providing useful suggestions, mainly about the actual implementation of the numerical differentiation within the LSA.

As for chapter 4, three application cases are presented and commented upon. Since the first two application cases have been conducted using synthetically generated

data, the developed simulation tool is described at first. Then, the setup and the results of a simulated steel beam and of an alloy plate are detailed. In fact, several analyses have been conducted, in order to evaluate the impact of varying inputs such as the accuracy of the observations and the number of the partitions on the estimated parameters and their accuracies. For the case of the steel beam, the simulation tool has been also used to estimate the sensitivity of the results depending on a variable standpoint of the laser scanner. The last part of the chapter is then dedicated to the application of the method to the monitoring of a cross-laminated timber slab, which has been performed with real data.

Finally, chapter 5 delivers a concluding outlook over the whole thesis and provides some suggestions about the possible extensions and improvements of the proposed method.

While this thesis has been designed and carried out as a monography, the author has published several of the new contributions and analyses in earlier or more concentrated version along the way (Serantoni et al., 2017, 2018; Serantoni and Wieser, 2019). These publications are cited in the corresponding subsections of the thesis. Furthermore, the author has contributed to other publications related to structural monitoring and terrestrial laser scanning beyond the integrated monitoring covered herein (Serantoni et al., 2015a,b; Ferrari et al., 2015, 2016; Serantoni and Wieser, 2016; Selvaggi et al., 2019; Frangez et al., 2020).

2. Background

2.1. Terrestrial Laser Scanning

Today, terrestrial laser scanning is a very widespread measuring technique, which is progressively getting more affordable and user-friendly. Compared to other surveying techniques, a great advantage of TLS is the shift of a good part of the invested time from the acquisition to the data analysis in the office. In fact, the acquisition of large amounts of features is cheaper, because of the reduced personnel costs on field (the TLS field operator does not need a great experience or outstanding skills) and the possibility to automatise several processing steps such as the registration of scans, their georeferencing, the recognition and the extraction of the interesting features.

2.1.1. How TLS works

This section provides an insight on the topics related to TLS that are necessary to understand and contextualise the following chapters. The fundamentals about TLS are detailed in the books by Vosselman and Maas (2010) and Shan and Toth (2018).

The TLS is an optical active remote sensing technology that permits to measure the distance of opaque surfaces in multiple directions. To determine the distance between the sensor and the target, two types of associated measurement principle are used: pulse-based scanners measure the time-of-flight of the reflected pulses, while phase-based scanners measure the phase shift between the sent amplitude-modulated continuous-wave (AMCW) and its reflection. In this work, the analysis holds for both these categories of scanners.

The terrestrial laser scanners available on the market are built in different ways, but the major part of those used for surveying purposes belongs to the category of panorama scanners, as opposed to camera scanners. The discussion herein is restricted to panorama scanners, which feature a fast rotating mirror that deflects the laser beam. More precisely, the rotation velocity of the mirror has two components: a fast rotating primary rotation axis that is typically approximately horizontal, and a much slower secondary rotation axis that is approximately vertical, assuming the instrument properly levelled. Typically, the whole housing of the instrument slowly rotates around the vertical axis. In a more formal way, if we represent the beam

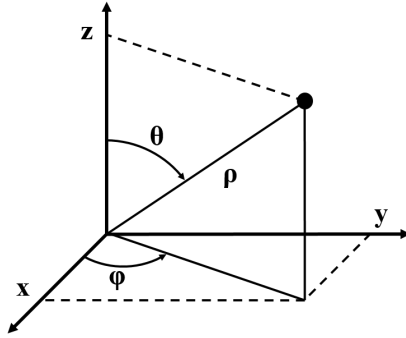


Figure 2.1: Sketch of the adopted convention for spherical coordinates.

direction in spherical coordinates (the adopted convention is shown in fig. 2.1, and the z axis is approximately aligned with the gravity vector if the scanner is properly levelled) and centre of the system of coordinates in the instrument location, the beam moves with constant angular velocities $\dot{\theta}$ and $\dot{\varphi}$, with $\dot{\theta} \gg \dot{\varphi}$.

Furthermore, the areal measurement process with TLS can be labelled as static. In fact, a repetition of a measurement can be only done in an amount of time comparable with the duration of the scan itself, seldom below 1 minute, depending on the scanner model, its resolution, and quality settings. Actually, dynamic measurements with TLS are also possible (Ferrari et al., 2015; Kim et al., 2016; Schill, 2018), but they cannot be considered really areal, since only a single profile of the structure is monitored.

2.1.2. TLS error modelling

Several contributions to the measurement deviations can be encountered when analysing laser scanner data. The angular errors of a laser scanner are caused by very similar phenomena as for total stations, i.e. by a combination of tilts and offsets of the two rotation axes and of the beam direction of propagation. The error sources involved in the range measurement process are multiple as well, and they are due either to a partially incorrect modelling of different stages of the signal involved in the measurement process (i.e. generation, propagation, reflection, acquisition, and digitisation), or to an insufficient information on the sources of variability within those (e.g. temperature distribution within the instrument).

The description of the stochastic properties of the TLS-acquired point clouds has been object of investigations of several researchers (Lichti et al., 2005; Gordon, 2008; Chaudhry et al., 2019; Holst et al., 2019a; Zámečníková et al., 2014), and multiple calibration methods have been proposed (e.g. Lichti, 2006; Medić et al., 2019). However, a universally agreed pointwise error model has not been defined yet, neither for the biases nor for the random deviations.

To my knowledge, the most comprehensive works addressing the simulation of the error distribution of TLS measured surfaces have been written by Soudarissanane

(2016) and Mill (2016).

In this work, the accuracy of the used scanners has been estimated according to the specification sheets provided by the TLS manufacturers, which express the expected measurement errors with the following indicators:

- range error, i.e. the average bias when measuring the distance of a scanned surface;
- range noise, i.e. the root mean square (RMS) of the deviations with respect to the best-fit-plane of the scanned surface;
- angular error, which is of difficult interpretation, as it is often not clear if it simply refers to the accuracy of the angular encoders or to the expected bias of the beam direction in both azimuth and elevation angles.

In tab. 2.1, some exemplary values of the specifications of some TLS systems currently on the market are provided.

Even when all of the listed specifications are available, the stated range errors apply to a very limited set of diffuse reflectance standards, i.e. standardised physical samples of quasi-Lambertian diffusive materials.

In addition, it is worth to mention that TLS techniques are able to measure only the surface of the scanned objects. Until now the penetration of the laser beam in materials is still an open issue. Some partial investigation has been conducted for porous materials such as snow (Serantoni and Wieser, 2016).

Moreover, even if the effects of the misalignments lead to biases lower than the ones stated by the manufacturer, they can be often easily spotted when analysing TLS datasets for deformation monitoring purposes, i.e. when comparing two or more point clouds acquired when repeatedly scanning the same object. Two-face measurements are useful to quantify some of these misalignments and therefore reduce the bias via on-site calibration, in a similar fashion of the index error determination when performing measurements with a total station (Holst et al., 2017).

Besides the discussion about the point-wise accuracy of TLS, the modelling of the co-variances within a TLS-acquired point cloud is a currently debated topic as well. In fact, depending on the resolution and the cross-sectional energy distribution of the laser beam, neighbouring measured points may be correlated because the respective beams' footprints may overlap. The footprint of the laser beam is the area of the sensed surface illuminated by the laser, i.e. where the reflection, and hence the surface-related distortions of the signal, take place.

In addition, a rigorous modelling of the covariances among different points belonging to the same point cloud should also take into account that the neighbouring points belonging to the same vertical profile (φ approximately constant, see fig. 2.1) are acquired in sequence. Thus, the correlation of the noise on points on the same vertical profile is likely to be larger than the correlation between other pairs of points, even if at the same elevation angle. In fact, the magnitude of systematic

Technology	Faro Focus3D X330	Leica P50	Leica RTC360 3D	Riegl VZ-400i	Surphaser 400	Z+F 5016i
Min / max range [m]	0.6 / 330	0.4 / 1000	0.5 / 130	0.5 / 800	1 / 140	0.3 / 360
Min range error (1σ)	2 mm	1.2 mm + 10 ppm	1 mm + 10 ppm	5 mm	0.07 mm	1 mm + 10 ppm
Min range noise (1σ)	0.3 mm	0.4 mm	0.4 mm	3 mm	0.07 mm	0.14 mm
Angular accuracy (1σ)	n.a.	8"	18"	n.a.	15"	14.4"
Angular step size	32.4" / 32.4"	n.a.	62"	2.5" / 5.4"	40" / 10"	0.65" / 0.94"
Field of view (φ / θ)	360° / 300°	360° / 290°	360° / 300°	360° / 100°	360° / 270°	360° / 320°

Table 2.1: Summary of the main accuracy and resolution specifications for a selection of market-available terrestrial laser scanners

errors of the angle encoders may be the same for the two rotation angles. Nevertheless, in this work no correlation among any pair of points have been assumed. Hence the question: how to exploit the redundancy of such datasets? Several solutions are possible: (i) neglect the phenomenon, (ii) identify and remove some points so that the remaining ones are uncorrelated, or (iii) take into account all the correlations among all the points belonging to a point cloud. In this work, the solution (i) has been adopted, as no unanimously accepted models exist yet. The variance-covariance matrix (VCM) of each point has been modelled, but the covariances between points have not. This topic is investigated more in depth in section 3.3.

2.1.3. Registration of point clouds

In the classical treatment of TLS data, the registration process plays a crucial role. The term *registration* denotes the translation and rotation of two or more point clouds into the same reference system. The need for registration arises when merging several quasi-simultaneously acquired point clouds to produce a larger point cloud, and when aligning two or more point clouds acquired in different epochs in order to extract the deformations among them. Even if the study of the registration process is outside the scope of this thesis, the method presented herein requires a prior inter-epochal registration.

The registration of multiple scans can be accomplished in several ways:

- with physical targets:
 - spheres, which have the advantage of having the same aspect from any point of view;
 - flat targets with geometrical patterns such as checkerboards or circular sectors (Omidalizarandi et al., 2019; Janßen et al., 2019), which can be opportunely oriented to reduce the incidence angle-based bias and whose permanent installation is generally more practical;
- point-cloud based techniques:
 - Iterative Closest Point (ICP) (Chen and Medioni, 1991; Besl and McKay, 1992);
 - 4-Points Congruent Sets (4PCS), a method for the markerless initialisation of refinement methods such as ICP (Theiler, 2015);
 - octree-based methods useful to distinguish between stable and unstable portions of the point cloud (Wujanz, 2016; Friedli and Wieser, 2016);
- feature-based techniques:
 - plane detection approaches (He et al., 2005; Dold and Brenner, 2006; Hu et al., 2019);
 - RGB-D based methods (Wagner et al., 2017), which rely on the fusion of TLS and image data into depth images;

- Feature to Feature Supervoxel-based Spatial Smoothing (F2S3), an approach that relies on the correspondences of machine-learned features (Gojcic et al., 2020);
- direct georeferencing:
 - in a similar fashion of free-stationing a total station (TS), as described by Pandžić et al. (2017);
 - directly during the fieldwork, by using an instrument that integrates both the capabilities of TS and TLS (e.g. *Leica Multistation*, *Trimble Scanning Total Station*);
 - with the help of additional navigation sensors embedded in the laser scanner, such as inertial units, accelerometers, or GNSS receivers.

The relative magnitude of the inter-epochal registration error with respect to the accuracy of the point clouds themselves depends strongly on both the registration method and the scanning setup, i.e. the scanner accuracy, its distance to the target, and the mechanical stability of the instrument. For monitoring purposes, target-based approaches are often used, because they can be placed in stable areas and their use can be very accurate if the setup of the targets (i.e. number, size, distance, and orientation) is well designed.

Within this thesis, the point clouds used for the experiments conducted with real data (see section 4.4) have been registered with the help of physical flat targets. With this solution, a good accuracy could be reached (below 1 mm) while keeping the computational effort very low.

2.1.4. Monitoring with TLS

An issue that is often encountered in practice is the choice of the most appropriate measurement system for a given monitoring task. In particular, it is interesting to know how does TLS compare with respect to other remote systems for monitoring purposes. This is important to understand the suitability of TLS for different classes of applications. A quite complete list of parameters and features of remote sensing systems has been provided by Mazzanti (2012). The list has been compiled having primarily geotechnical applications in mind:

- *precision*: repeatability of measurements;
- *data reliability and validity*: reliability of the collected measurements;
- *temporal resolution*: maximum frequency in data collection;
- *spatial resolution*: maximum resolution of pixels at the ground/structure, i.e. minimum size of the area where a deformation value is provided;
- *information density*: the density of information in terms of number of pixels and their areal distribution;
- *deformation geometry*: geometrical information of the deformation measure-

ment (e.g. unidirectional predefined, unidirectional, bidirectional, 3D, etc);

- *degree of interaction with the ground/structure*: interaction with the monitored area, which ranges from zero for the fully remote techniques, to high for techniques that require the installation of targets on the investigated object;
- *size of the monitored area*: maximum size of the area that can be monitored simultaneously by a single sensor;
- *maximum operability range*: maximum distance to which the deformation of a target (artificial or natural) can be determined;
- *atmospheric noise*: degree of sensitivity to the atmospheric noise;
- *budget*: cost required for the monitoring.

This list is very useful to compare advantages and disadvantages of different sensor systems, even if in the geodetic community, the categories *precision* and *data reliability and validity* should probably be replaced by the better-defined set of accuracy, precision, and reliability, which have a more sound mathematical definition. For an overview about the most established mathematical tools used in the field of geodetic deformation analysis, see the work of Caspary (2000) and Heunecke et al. (2013). Moreover, other two items that should be added to the list are the *minimum operability range*, a limitation that all remote systems have, and the distinction between installation and running costs. According to the presented classification criteria, compared to other techniques such as radar interferometry, digital photogrammetry, and trigonometric surveying, TLS features the strengths of high information density, no interaction with the investigated object, and the possibility to monitor large areas. On the other hand, TLS features limited operative range, and strong limitations due to the atmospheric conditions. These assessments are valid for whole classes of sensors, and they are of course quite generic. Moreover, no sensor system is intrinsically better than the others, and the aptest instrument should be chosen according to the concrete application case.

2.2. Finite Element Method

The FE method is arguably the most widespread method to numerically solve partial differential equations (PDEs). Among others, the main applications include elastostatics, structural dynamics, heat diffusion, electromagnetism, fluid dynamics. Within this work, the selection of the FEM as numerical method to link the measurements to the material properties has followed the consideration of some advantages and disadvantages:

- ⊕ The flexibility in modelling free-form structures and non-linear materials.
- ⊕ The freedom of choice of the estimated structural parameters, as long as they are contained in the stiffness matrix or in the vector of the nodal forces.

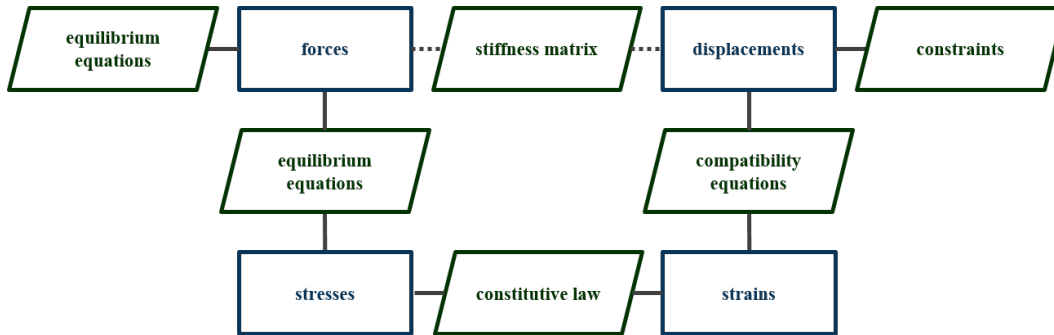


Figure 2.2: Tonti diagram of elastostatics. Figure adapted from (Tonti and Zarantonello, 2009)

- ⊕ There is no need to develop *ad hoc* analytical models for every investigated structure, as this widens the range of potential applications and makes the proposed method more general. In fact, also an analytic relationship between the observables (i.e. the deformations) and the unknown parameters would be sufficient in principle.
- ⊕ The popularity among both the technical and scientific communities of structural engineers.
- ⊖ The plausibility control of the results is still necessary, and left to the engineer's judgement.

For a thorough introduction to the FE method, see the books by e.g. Hughes (2000) and Johnson (2000). The mathematical foundation of the FE method is to avoid the need of searching for a solution to the PDE expressed in the so-called strong (or complete) form; the solution is instead searched within a finite-dimensional space, with the help of a weak (or integral) form. Intuitively, and without claiming to be complete, the weak form is a projection of the strong form on a finite base of test functions. The weak form is also termed *variational form* because it can be obtained by applying energy principles, such as the principle of virtual works or the principle of minimum energy.

The diagram displayed in fig. 2.2 shows in a compact way the relationships between stresses, mechanical properties and deformations. In the theory of linear elasticity, the displacements are connected to the forces applied on a deformable body via a chain of the fundamental mathematical relationships, i.e. the compatibility equations, the constitutive relations, and the equilibrium equations. However, the FE model links directly forces and displacements according to the following equation:

$$\mathbf{f} = \mathbf{K}\mathbf{u} \quad (2.1)$$

where \mathbf{f} is the vector of the nodal forces, \mathbf{K} is the stiffness matrix, and \mathbf{u} is the vector of the nodal displacements. In fact, both the constitutive laws and the equilibrium and compatibility equations are embedded in the stiffness matrix. Each entry of the stiffness matrix $k_{i,j}$ represents the value of the the nodal force F_j that has to be

ABAQUS Continuum Elements

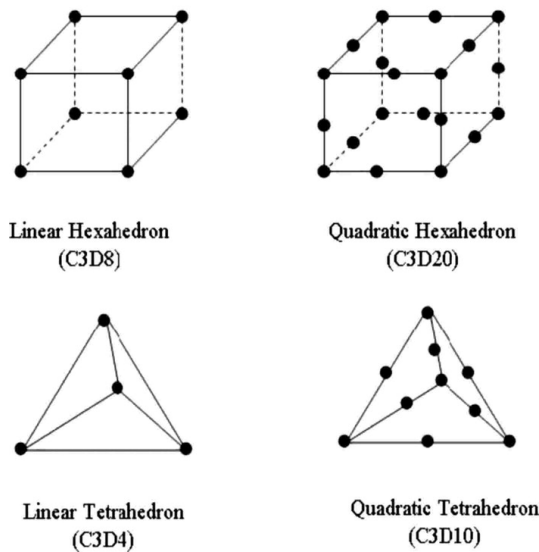


Figure 2.3: Examples of continuum finite element types available in the FE solver Abaqus, from (Holstein et al., 2009)

applied on the system to obtain a unitary displacement d_i .

The steps involved in the FE analysis are the following:

- discretisation of the analysed body in finite elements (meshing);
- definition of the shape functions, which interpolate the solution (in case of elastostatic analyses, the field of displacements) between the nodes of an element, which are often low-order polynomials;
- assembly of the global stiffness matrix according to the connections among the individual elements (direct stiffness method), i.e. the whole set of equations is defined;
- application of boundary conditions (BC), i.e. loads and constraints;
- solution of the system of equations for the primary variables at the nodes' locations, i.e the nodal displacements;
- optionally, derivation for the secondary variables, i.e. the nodal forces are obtained by back-calculation, while strain and stresses are calculated by interpolation.

The choice of the type of finite elements depends on the level of detail and complexity that the engineer aims to simulate with his model. For example, when modelling a truss structure or a 3D frame made of columns and girders, it often makes sense to employ beam elements, whereas when modelling a shell structure, the most sensible choice may be to use bi-dimensional triangular elements such as triangles. Indeed, several kinds of solid finite elements exist. Four examples of them are shown in

fig. 2.3. Furthermore, for every combination of shape and number of nodes, various strategies of integration can be employed, depending on the number and location of the integration points. For example, the C3D8 (continuous stress and displacement, 3D, 8 nodes) element can be modified to allow for reduced integration (e.g. C3D8R elements) or to reduce the shear locking¹ by adding incompatible displacements (e.g. C3D8I elements). For a wide list of finite elements, one can consult the book by Oñate (2013a).

¹an overly stiff behaviour of a finite element due non-physical constrains between the nodal displacements (Oñate, 2013b)

3. From TLS data to material parameters

As stated in section 1.3, the rationale behind this research is to exploit the areal information provided by laser scanners, and assess the potential benefits that the measurement of large amounts of points can bring in the context of SHM.

The main inspiration behind this work is the idea of extending the concept and the functionality of integrated monitoring to TLS areal surface measurements. *Integrated monitoring* is a method that combines data from various sources and sensors within a coherent and flexible framework for SHM applications. It has been formalised by Chrzanowski et al. (1991) and applied in practice by Lienhart (2007), who developed his work on the basis of the contributions of Kälber and Jäger (2000) and Jäger et al. (2004). In fact, in his dissertation, Lienhart used observations from total stations, geometric levelling, fibre optics extensometers (SOFO), inclinometers and temperature sensors to calibrate the FE model of a monolithic bridge. More details are provided in section 3.4

Moreover, this work focuses on a specific field of SHM, which is the numerical identification of material parameters of structures subject to a static loading. Welsch and Heunecke (2001) defined the system identification as the determination of a transfer function that turns the input quantities (the stresses) into the output ones (the deformations) (see fig. 3.1). According to the scheme by Welsch and Heunecke (2001), the determination of the stresses is defined as *back analysis* (inverse problem), while the determination of the deformations is named *system analysis* (direct problem). Furthermore, this work can be also classified as system identification by using a parametric model, because the deformations and the loads are known and the material parameters are determined with the help of a mechanical model.

In addition, since a numerical approach instead of an analytical one is adopted, the analytical constitutive law of the investigated materials is not explicitly modelled, but only a selection of the parameters within the stiffness matrix. Indeed, the stiffness matrix \mathbf{K} does not depend on the material parameters only, it depends on the choice of the element types and their shape functions as well.

Lastly, when dealing with FE models, the task of identification can be denoted in

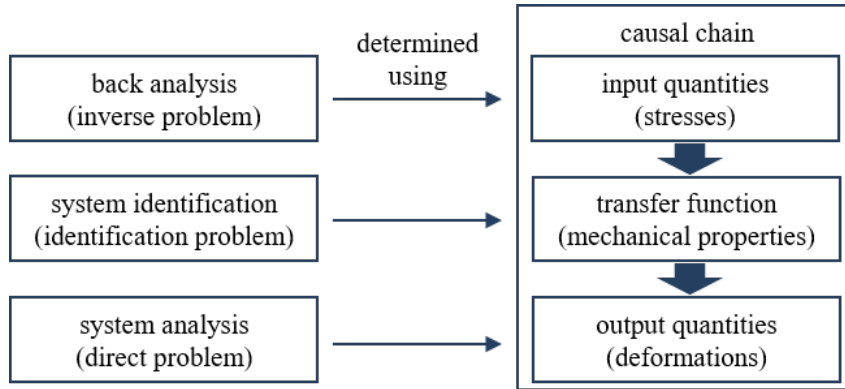


Figure 3.1: The behaviour of a system can be described by three sets of elements: input, transfer function, output. For structural systems, the three sets coincide with forces, mechanical properties and deformations, respectively. Adapted from (Welsch and Heunecke, 2001)

literature as model updating (especially in the SHM scientific community), model calibration, model tuning, or inverse finite element problem.

This chapter presents and details the conceived method for the material identification of TLS scanned structures. The main points of the chapter and especially the description of the three interpolation schemes presented in section 3.3, have been already summarised in (Serantoni and Wieser, 2019).

3.1. Workflow

The developed method is built upon three subsequent main steps: the generation of the FE mesh, the calculation of the surface nodal displacements from TLS data, and the determination of the sought parameters, under the overarching criterion that the FEM-calculated displacements shall fit to the measured ones. This method is concisely illustrated by the block diagram in fig. 3.2.

First of all, the developed algorithm takes as input data pairs of point clouds: a reference one and a test one, which respectively represent the outer surface of the structure in the states before and after the deformation, named throughout this thesis *reference* and *deformed* state, respectively. When more than two epochal measurements are available, any couple of them can be employed as input data. Of course, the input points clouds have to be registered in the same reference system of coordinates. The method of registration (see section 2.1.3) is not relevant, as long as its associated error is negligible with respect to the intrinsic accuracy of each point cloud.

If several scans from different standpoints are acquired within the same monitoring epoch, they have to be co-registered, and all the measured displacements can be used, provided that the VCM of each measured point is modelled according to the position of the associated scanner standpoint. In this work, except for the applica-

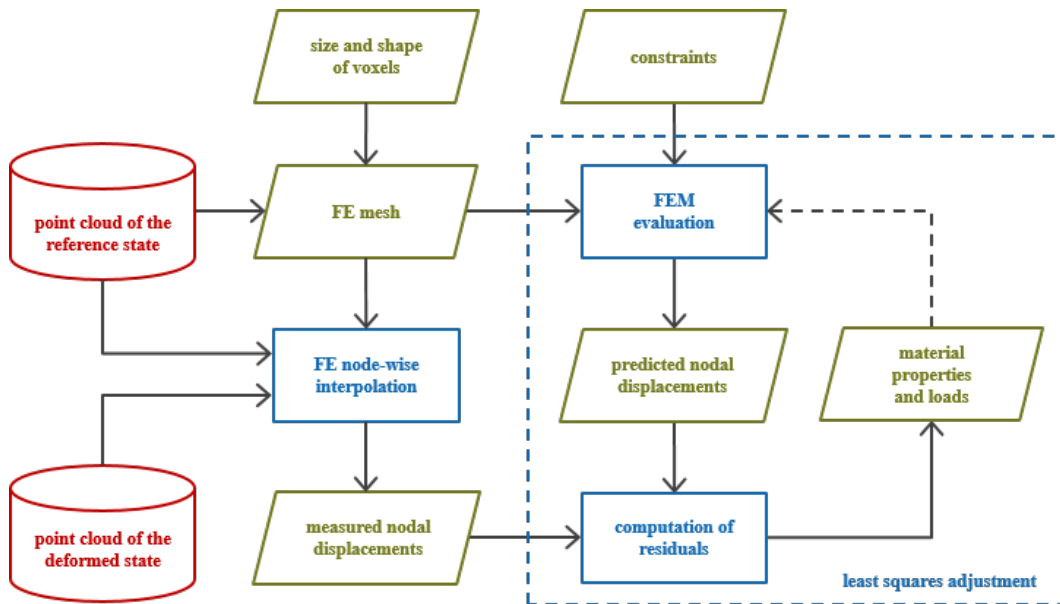


Figure 3.2: The block diagram of the proposed method

tion case described in section 4.4, a single scan is used for each material parameter determination.

Moreover, the proposed algorithm is suitable for quasi-real time monitoring, because the analysis can be performed after each acquisition epoch, as the modelling step is uncoupled with the extraction of displacements. However, given that the acquisition of the measurements and the processing take several minutes, the integration within an early warning system looks hardly feasible. In addition, the developed method is suited for problems that are linear (geometrically and materially) only.

The reference point cloud is used as input to generate the mesh of the FE model. The size and shape used for the voxelisation of the space occupied by the structure have to be chosen according to the desired level of detail. Furthermore, the engineer should also select the kind and the size of the FE elements that are employed. The process of the FE mesh generation is extensively described in section 3.2.

In order to fully define the FE model, the FE mesh is not sufficient, because loads and boundary conditions have to be formalised as well. Since the loads can be included in the set of parameters to be estimated (see section 3.4.1), they are defined according to prior knowledge on them. In fact, unless a structure is new and we can claim we can calculate the dead loads, the exact estimation of the loads is usually very difficult. The type of constraints do not belong to the set of parameters to be estimated, and they have to be defined according to the prior knowledge about the scanned structure.

The two point clouds are also used to determine the surface nodal displacements. They are calculated by first extracting the field of displacements, which is obtained

by calculating the distance between the two clouds, and then by interpolating in correspondence of the locations of the nodes of the FE mesh. Several interpolation strategies are possible; in sections 3.3.1, 3.3.2, and 3.3.3, three different ones are illustrated, and successively compared in section 3.3.4.

Once the measured nodal displacements have been derived, it is possible to search for the desired structural parameters by running a least squares adjustment (LSA). The LSA iteratively evaluates the FEM for different values of the parameters until the residuals between the FE-predicted and the measured nodal displacements are minimised (see section 3.4).

The whole implementation has been written in Matlab, except for the evaluation of the FE model, which is performed by the commercial software package Abaqus. The interaction between the Matlab code and Abaqus (Dassault Systèmes, 2013) has been enabled by wrappers that write input (.inp) files, read data (.dat) and output (.fin) files, and call the execution of Abaqus/Standard jobs with dedicated DOS commands. Because of this strategy, the method presented herein can be easily adapted to work in association with any solver. Indeed, besides Abaqus, a large number of alternative available FE solvers exist. Even if some of them can directly and explicitly deliver the stiffness matrix of the modelled structure, the followed approach treats the FE solver as a "black box" by the direct linearisation of the output (i.e. the nodal displacements) with respect to the inputs (i.e. material parameters, loads, and measurements).

All the analyses and simulations of this work have been conducted with a personal computer equipped with an *Intel Xeon E5-1650 v2* processor (3.50 GHz) and 32 GB of RAM. Matlab integrates a very transparent parallelisation of *for* loops, which has been used taking advantage of all the 6 cores of the employed processor. Parallel computations have been conducted in the following stages of processing:

- sorting the FE elements according to their coordinates, in order to define the elements belonging to each partition of the FE model;
- calculating the numerical derivatives for several partitions within the LSA;
- calculating the mean vertical displacement for points of the point cloud that are aligned along the normal of a monitored surface;
- performing Monte Carlo simulations.

3.2. FE model generation

It is important to clarify that if the FE model is already available before the scanning, there is no need to generate the mesh via voxelisation of the reference point cloud data. Although it is a quite unrealistic case in practice, this may happen when the designer has already created a FE model for design purposes beforehand, provided that the geometry of the as-built structure corresponds to the designed one within the desired accuracy. In that case, the acquired point clouds would be only used for

the dimensional control of the as-built structure. If instead no FE model is available, the generation of the FE model is made according to these subsequent steps, which are further explained below:

- definition of the volume occupied by the structure;
- voxelisation;
- choice of the FE elements;
- assignment of the material properties;
- definition of the boundary conditions.

Definition of the volume occupied by the structure

In order to have a continuous representation of the outer surface of the structure, a 3D alpha solid of the reference point cloud is used. An alpha solid is the generalisation of the alpha shape for the 3D case. Intuitively, the alpha shape of a set of points is a polytope that is uniquely determined by the set and a parameter α . It expresses the intuitive notion of shape of the point set, and α controls the level of detail reflected by the polytope (Akkiraju et al., 1995). For example, the convex hull of a set of points coincides with the alpha shape with $\alpha = +\infty$ (see fig. 3.3). For a complete exposition about 3D and n-dimensional alpha solids, see (Edelsbrunner and Mücke, 1994). The level of detail of the alpha shape is also determined by the resolution of the point cloud representing the object surface. If some parts of the surface are coarsely scanned or not scanned at all (it is often the case for the supports or the foundations), artefact concavities may be generated. To prevent such artefacts, the missing surface points have to be reconstructed using assumptions or prior knowledge.

Voxelisation

The voxelisation is an intermediate step between the definition of a bounded shape and the discretisation into multiple regular finite elements. Practically, the 3D space is first subdivided according to a 3D grid, then the centres of the potential voxels whose centre lies within the alpha solid are selected. A sketch of the discretisation process is shown in fig. 3.4.

Such voxelisation of the structure volume introduces a discretisation effect of the surface, which is especially noticeable when the actual surface of the structure is not parallel to the three principal directions of the voxels. An example is shown in fig. 3.5.

Choice of the FE elements

In this thesis, general-purpose 3D elements (i.e. hexahedron-shaped ones) have been chosen, in order to deal with generic-shaped structures. In particular, general-purpose hexahedral ones (e.g. C3D8, C3D8R, C3D8I) have been selected, because

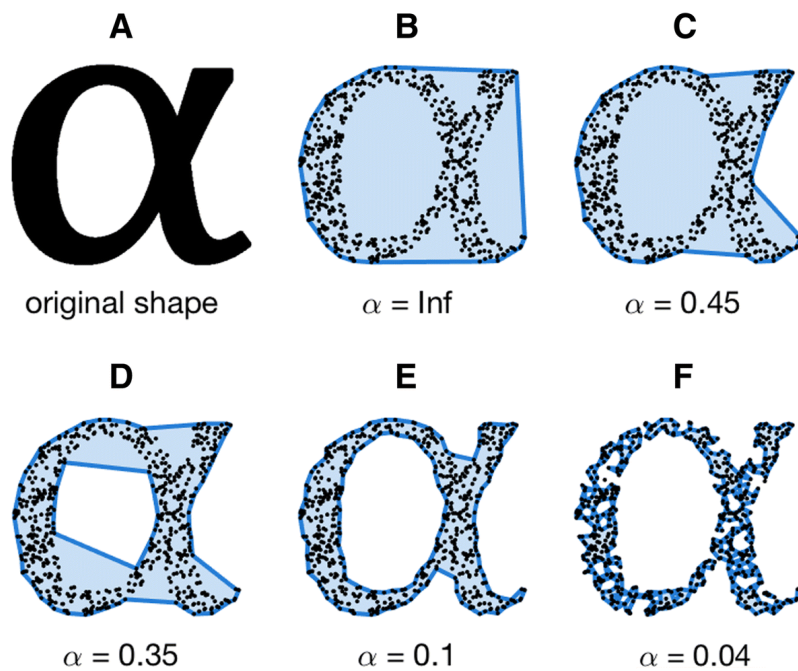


Figure 3.3: Alpha shape for a decreasing value of the parameter α . From (Gardiner et al., 2018)

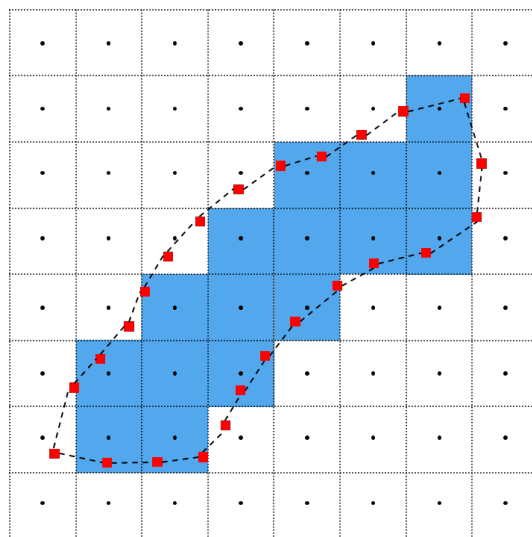


Figure 3.4: Discretisation of the structure using an alpha shape built from the scanned points (2D for graphical reasons, 3D in reality). The red square dots represent the points of the point cloud, the dashed line represents the alpha shape boundary, the black dots represent the centres of the potential voxels, while the blue hatched squares represent the voxels that have been actually selected (adapted from Serantoni et al., 2018)

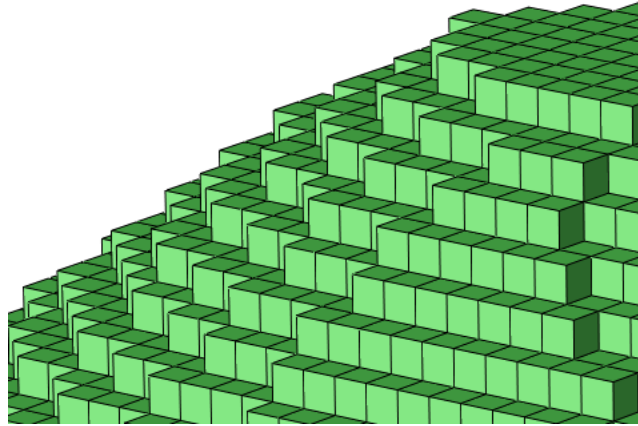


Figure 3.5: Example of the voxel discretisation effect for curved surfaces

their size can be easily set to be equal to the one of the previous voxelisation step. However, the use of hexahedron discretisation implies non-smooth FE mesh for smoothly curved objects. This issue can be overcome either by increasing the resolution of the mesh or by using alternative element types for the 3D tessellation of the volume occupied by the structure, such as tetrahedrons, irregular hexaedrons or wedge elements. Another interesting alternative for future investigation can also be the refinement of the voxel discretisation by using marching cubes (Kim et al., 2019).

Herein, the size and the shape of the voxels are selected to coincide with an integer multiple of the size of the finite elements. The choice of the size of the elements is a compromise between the spatial resolution of the predicted nodal displacements and the computational effort to perform the FE analysis. Moreover, the size of the elements should also prevent the generation of numerical errors. For example, when modelling a beam or a plate made of linear C3D8 elements and subject to bending, it is necessary to discretise the body along the directions transverse to the bending moment in multiple elements, in order to avoid shear locking effects. Alternatively, the use of C3D8R or C3D8I elements is also possible. A rigorous discussion on the topic can be found in (Hughes, 2000), while a comparison of locking effects for different FE software packages is provided by Sun (2006).

Assignment of the material properties

The material parameters are passed as input to Abaqus as (E, ν) for the orthotropic linear elastic case, or by providing the 9 independent entries of the compliance tensor \mathbf{C} (see eqn. 3.1), which are named *engineering constants* according to the Abaqus nomenclature (Dassault Systèmes, 2013). This is a very specific assumption pertaining to certain classes of materials.

$$\begin{array}{c}
\left\{ \begin{array}{l} \varepsilon_{11} \\ \varepsilon_{22} \\ \varepsilon_{33} \\ \gamma_{12} \\ \gamma_{13} \\ \gamma_{23} \end{array} \right\} = \begin{bmatrix} \frac{1}{E_1} & \frac{-\nu_{21}}{E_2} & \frac{-\nu_{31}}{E_3} & 0 & 0 & 0 \\ \frac{-\nu_{12}}{E_1} & \frac{1}{E_2} & \frac{-\nu_{32}}{E_3} & 0 & 0 & 0 \\ \frac{-\nu_{13}}{E_1} & \frac{-\nu_{23}}{E_2} & \frac{1}{E_3} & 0 & 0 & 0 \\ 0 & 0 & 0 & \frac{1}{G_{11}} & 0 & 0 \\ 0 & 0 & 0 & 0 & \frac{1}{G_{22}} & 0 \\ 0 & 0 & 0 & 0 & 0 & \frac{1}{G_{33}} \end{bmatrix} \left\{ \begin{array}{l} \sigma_{11} \\ \sigma_{22} \\ \sigma_{33} \\ \sigma_{12} \\ \sigma_{13} \\ \sigma_{23} \end{array} \right\} \\
\varepsilon \qquad \qquad \qquad \mathbf{C} \qquad \qquad \qquad \sigma
\end{array} \quad (3.1)$$

The field of validity of the presented method is bounded by some assumptions. No cracks are modelled, and the materials are assumed to be linear elastic, i.e. the yield stress is not attained anywhere in the investigated body. Nevertheless, the material is not restricted to be neither isotropic nor orthotropic. However, it is worth to note that the definition of the yield point of uniaxial tests is not unique. Among the various definitions, the yield point is often associated to a permanent strain equal to 0.2%. However, in the field of structural engineering, the yield point of mild steel can be also conservatively defined as the lowest stress for which local plasticisation occurs at the elastic-plastic transition (Dieter, 1986).

Definition of the boundary conditions

Operatively, the assignment of the boundary conditions is manual. For this task, a combination of prior knowledge and the engineering judgement is needed. However, it is also possible to model the constraints so that their definition includes parameters to be estimated, e.g. the stiffness of a support.

3.3. Interpolation of nodal displacements and their covariances

As stated in section 3.1, the main criterion underlying the whole identification process is the coincidence of the FE-simulated nodal displacements with the TLS-measured ones. Since the spatial distributions of the points of the TLS-acquired point cloud and of the nodes of the FE model are different, an interpolation strategy has to be adopted. In fact, while the locations of the nodes of the FEM depend on the choice of FE type and on the strategy adopted for meshing the object, the points of the point cloud are located where the laser beam hits a diffuse reflective surface. Therefore, their distribution depends mainly on the resolution of the scanner and its position with respect to the scanned objects. In fact, the majority of laser scanners provide point clouds whose angular resolution is constant around each rotation axis, i.e. the vertical and horizontal ones. As a result, within a single scan, the spatial density of the point cloud is inversely proportional to the square of the range between the sensor and the scanned surface (see fig. 3.6).

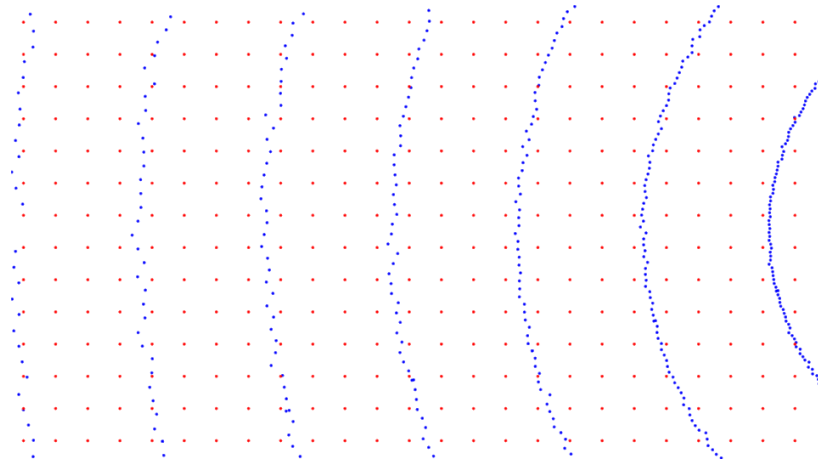


Figure 3.6: A schematic representation of the different spatial distributions of FE nodes (in red) and the measured points (in blue). The picture is a close-up of a scanned flat surface (see chapter 4)

Moreover, it is generally neither possible to directly relate the individual points of the point cloud to individual physical points on the surface, nor to measure multiple times the same locations on the structure, because of the practical impossibility to repeatedly start the scan from the same exact orientation. For this reason, the use of the point clouds is restricted to the measurements of the out-of-surface deformation components, i.e. the apparent surface changes perpendicular to the surface at the reference epoch. The approach is thus most sensitive to deformations that actually occur in that direction, e.g. to the vertical deformation of a horizontal beam loaded on top and scanned from below.

As for the modelling of the instrumental errors, in this work the random deviations have been assumed to be Gaussian distributed. Furthermore, the correction and removal of biases and artefacts such as mixed pixels and reflections has been neglected. These two kinds of artefacts can be reduced with a proper measurements setup, i.e. ensuring the absence of obstacles between the investigated object and the scanner. The presence of mixed pixels, which is often unavoidable when scanning the edges of the object's silhouette, can be strongly reduced by filtering algorithms embedded in commercially available scanners and in several post-processing software packages. A description of the causes behind the occurrence of mixed pixels and an example of implementation of a filter is provided in (Wang et al., 2016b).

Because of the different spatial distributions, in order to compare and match the nodal displacements of the FEM with the ones derived from the TLS point clouds, an interpolation strategy is needed, and when choosing on which support the interpolation is applied, the following three possibilities arise, each with advantages and disadvantages:

- (a) interpolate the TLS-measured point cloud onto the FE nodes of the reference epoch:
- ⊕ the FE nodes can be placed according to the engineer's judgement, i.e. the local mesh refinement is allowed;
 - ⊕ the interpolated values can be compared with the FEM output;
 - ⊕ when the FE model is evaluated iteratively within an optimisation algorithm that matches the simulated and the measured displacements, there is no need to perform the interpolation at every iteration step;
 - ⊕ overall simplicity;
 - ⊖ within the LSA (see section 3.4.1), the spatial distribution of the points in which the residuals are evaluated depends on the FE meshing and does not reflect the actual measurement process;
- (b) interpolate the FE nodal displacements onto the point cloud:
- ⊕ within the LSA, the spatial distribution of the points in which the residuals are evaluated reflects the measurements;
 - ⊖ the interpolation has to be performed at every iteration of the optimisation algorithm;
- (c) interpolate both the point cloud and the FE nodes onto a third support:
- ⊕ enables the use of parametric surfaces, including the use of FE methods specifically designed for parametric (i.e. NURBS) geometries instead of meshes, such as the isogeometric analysis (see Hughes et al., 2005; Cottrell et al., 2009);
 - ⊕ the number of parameters to compare can be drastically reduced, provided that the support geometry is suitably parametrised;
 - ⊖ compared to meshes, parametric surfaces (e.g. NURBS) representing complex structures are less straightforward to be automatically generated.

In light of the listed advantages and disadvantages, the chosen strategy consists in interpolating the TLS-measured point cloud onto the FE nodes, especially because of the subsequent computational economy.

The goal of this processing step is to assign a displacement to each FE node, and the available data consist in two point clouds: the reference and the deformed one. The surface of the FE model cannot be used as reference surface, because the mentioned (section 3.2) discretisation effect would reduce the precision of the acquired reference point cloud to the size of the FE elements. Indeed, the displacements of the nodes on the surface of the FE model have been calculated by computing the distance along the surface normal between the piecewise triangular interpolants of both the reference- and the deformed point clouds. Herein, the described method has been applied because the monitored objects are man-made structural

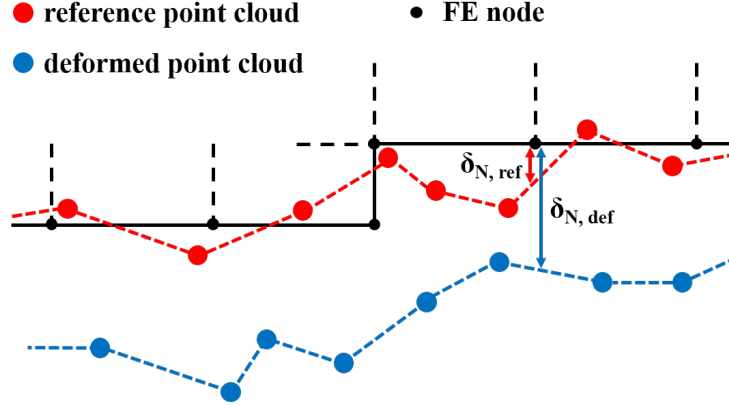


Figure 3.7: A 2D schematic representation of the reference point cloud (in red), the deformed point cloud (in blue), and the FE mesh (in black)

members, which usually feature locally smooth surfaces, and the direction along which the distance is calculated is known beforehand. However, the approach can be chosen differently, depending on the morphology of the structure's surface. Indeed, there are several different approaches to calculate the distance between two point clouds, such as cloud-to-cloud (C2C), cloud-to-mesh (C2M), mesh-to-mesh (M2M), multiscale-model-to-model-cloud comparison (M3C2). A review about them is provided by Girardeau-Montaut (2006), and Holst and Kuhlmann (2016).

As shown in fig. 3.7, the nodal displacements δ_N are calculated as follows:

$$\delta_N = \delta_{N,\text{def}} - \delta_{N,\text{ref}} \quad (3.2)$$

where $\delta_{N,\text{def}}$ and $\delta_{N,\text{ref}}$ are the distances between the nodes of the reference mesh and the triangulations of the deformed and reference point clouds, respectively. These distances can be calculated along any direction. The choice depends on the sensitivity of the measurements and the expected deformation of the structure. For example, in this thesis, all the analyses take into account the vertical component of the nodal displacements only.

Herein, a linear triangular interpolation relying on a 3D Delaunay triangulation (Amidror, 2002) has been employed. Each interpolated displacement δ_N corresponding to the FE node N is a weighted average of the z coordinates of the three points A, B, C of the point cloud, which form the triangle of the Delaunay triangulation where the node N is projected as N' (see fig. 3.8). The coefficients are the three normalised barycentric coordinates of N' within the 2D triangle ABC , according to the following formula:

$$\delta_N = \frac{A_{N'BC}}{A_{ABC}} z_A + \frac{A_{N'CA}}{A_{ABC}} z_B + \frac{A_{N'AB}}{A_{ABC}} z_C - z_N = \delta_N(x_N, y_N, z_N, \mathbf{x}) \quad (3.3)$$

$$\mathbf{x} = [x_A, y_A, z_A, x_B, y_B, z_B, x_C, y_C, z_C]^T \quad (3.4)$$

where e.g. A_{ABC} denotes the area of the triangle ABC . In eqn. 3.3 and 3.4, the coordinate system is rotated so that the displacement δ_N is aligned with the direction z .

Moreover, in order to avoid artefacts due to wrong assumptions on the spatial trend of the displacement field, no extrapolation is performed. In other words, the interpolation is limited to the 2D convex hull of the set of the projections of the measured points on the xy plane.

A further potential source of interpolation artefacts is addressed. Although the Delaunay triangulation strategy maximises the minimum internal angle of each triangle of the triangulation, if the measured points are sparsely distributed some triangle may be "skinny" ones. In this case, the interpolant presented in eqs. (3.3) and (3.4) tends to underestimate the intensity of the displacement field of bulging surfaces (Franke, 1982).

A triangle is considered skinny if the ratio between its inradius r_{inc} and its circumradius r_{circ} is lower than a certain threshold t to:

$$r_{\text{inc}}/r_{\text{circ}} < t \quad (3.5)$$

For accuracy reasons and to circumvent this effect, the affected displacements are discarded by adopting the following procedure. First, a Delaunay triangulation of the projection of the point cloud onto the FE surface is built, then the skinny triangles lying on its boundary are iteratively removed, and finally the sole displacements associated to the FE nodes located within the remaining triangulation are retained. In this way, no displacement is a product of extrapolation. A schematic representation of the skinny triangles identified by this process is provided in fig. 3.9.

The choice of t should be adapted in order to affect the skinny triangles only. An analysis of the distribution of the $r_{\text{inc}}/r_{\text{circ}}$ ratio for the whole triangulation can be helpful to set the threshold t . For example, t has been set equal to 0.02 in the simulations and in the application examples presented within this thesis.

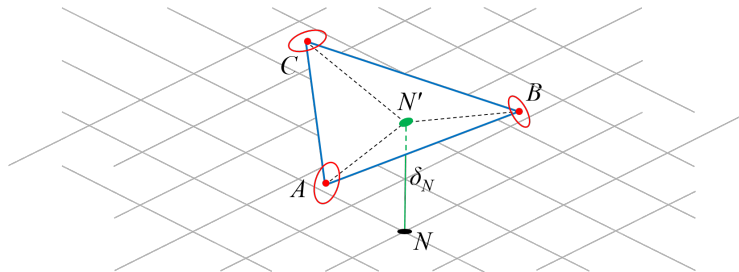


Figure 3.8: A schematic representation of the linear triangular interpolation. In black, the FE mesh and its nodes; in red, the measured point cloud and the points' error ellipsoids for each point; in blue, the interpolating triangulation; in green, an interpolated point and the calculated distance δ_N

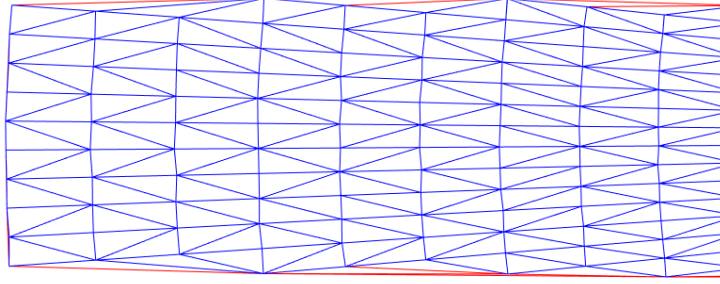


Figure 3.9: A schematic representation of the skinny triangles. The red skinny triangles at the boundary of the Delaunay triangulation of the measurement points (in blue) are iteratively removed

Along with the displacements of the FE nodes, their variances need to be calculated as well, because they are successively employed in the stochastic model of the parameter estimation (see section 3.4.1).

Irrespective of the strategy chosen to assign covariances to the points of the point clouds, the covariance assigned to the nodal displacements is derived owing to a straightforward variance propagation. The functional model is shown in eqn. 3.2, and the associated stochastic model is

$$\sigma_{\delta_N}^2 = \sigma_{\delta_{N,\text{def}}}^2 + \sigma_{\delta_{N,\text{ref}}}^2 \quad (3.6)$$

The assumption of uncorrelatedness is justified by the fact that the reference and the deformed point clouds are acquired at different times and possibly from different scanner standpoints.

In order to estimate σ_{δ_N} , if the point clouds are very dense as compared to the size of the finite elements, it might be sufficient to calculate for each node of the FE mesh the average of the measured displacements of several points in its neighbourhood, together with its associated empirical standard deviation. If instead the distribution of the scanned points is very sparse, i.e. if the average distance between points of the point cloud is much larger than the size of the finite elements, some more refined solution is necessary, possibly taking into account the expected accuracy of each measured point. In particular, the available input data are the coordinates and VCMs of the measured points, and the target coordinates of the FE nodes. A clarifying sketch is provided in fig. 3.10. In order to assign a VCM to a point obtained by interpolation, several strategies can be adopted, such as the classical variance propagation, the direct interpolation of VCMs, and the nearest-neighbour (NN) search. In the following sections 3.3.1 to 3.3.3, these three tested strategies are detailed. Among alternative schemes that are suitable for further investigations, there are methods such as collocation (Moritz, 1978), k-nearest neighbours search with distance-dependent weights (Dudani, 1976), and Kriging, which nevertheless suffers from the disadvantage of being a "global" method, i.e. the interpolant de-

depends on all the data points (Franke, 1982).

Regardless of the interpolation method chosen, the VCM Σ_P of each measured point P is defined in a quite straightforward way, i.e. employing the specifications model generally provided by the producers of laser scanners (see section 2.1.2). However, for the definition of Σ_P , the coordinates of the points of the point cloud are not enough, because the accuracy specifications of the scanner and its standpoint have to be known as well.

Concretely, the variance-covariance matrix Σ_P of each measured point is first expressed in an opportune local reference system (RS), so that its matrix representation is diagonal. Such a local RS is defined by the orthonormal triple of directions $(\hat{\rho}, \hat{t}_v, \hat{t}_h)$ (see fig. 3.11), where $\hat{\rho}$ is the radial unit vector along the line joining the instrumental centre S and the measured point P , \hat{t}_v is the tangent to the local meridian profile (i.e. with constant azimuth φ_0), and \hat{t}_h is the tangent to the local parallel profile (i.e. with constant elevation θ_0).

The three directions are determined as follows:

$$\hat{\rho} = \frac{P - S}{\|P - S\|} \quad (3.7)$$

$$\hat{t}_h = \hat{\rho} \wedge \hat{v} \quad (3.8)$$

$$\hat{t}_v = \hat{\rho} \wedge \hat{t}_h \quad (3.9)$$

where \hat{v} is the unit vector parallel to the local vertical in the standpoint S , and \wedge represents the vector product.

The local RS is a principal one for the matrix

$$\Sigma_P^L(\rho) = \begin{bmatrix} \left(\frac{\sigma_{\rho, \text{fix}} + \sigma_{\rho, \text{prop}} \rho}{\cos \alpha} \right)^2 & & \\ & (\sigma_{\varphi} \rho \cos \theta)^2 & \\ & & (\sigma_{\theta} \rho)^2 \end{bmatrix} \quad (3.10)$$

where ρ is the range (i.e. the distance between points S and P), $\sigma_{\rho, \text{fix}}$ and $\sigma_{\rho, \text{prop}}$ are respectively the constant and the distance-dependent parts of the range accuracy. α is the incidence angle, σ_{φ} and σ_{θ} are the angular accuracies of the horizontal and vertical angles, and the superscript L denotes the local RS. Here, the impact of the incidence angle alpha is modelled according to the findings of Soudarissanane (2016).

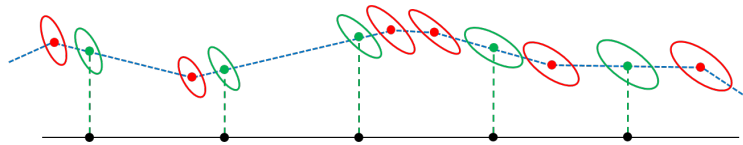


Figure 3.10: The interpolation of VCMs in correspondence to the FE nodes. The red error ellipses represent the input VCMs, while the green ones represent the interpolated ones. 2D sketch for ease of interpretation

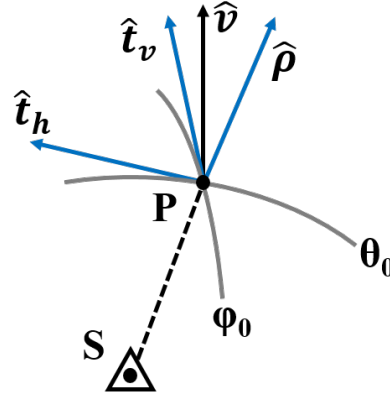


Figure 3.11: The local system of coordinates for the calculation of the VCM of a scanned point. From the scanner location S , the point P is measured. The definition of the shown symbols is provided in text

This author observed that, when scanning a flat surface, the orthogonal noise σ_{ρ_n} is approximately constant for a very wide range of incidence angles (between 0° and 80°), thus the range component of the TLS accuracy σ_ρ has been modelled as deteriorated by the factor $1/\cos \alpha$ (see fig. 3.12). In fact, since the projection of the range component of the noise onto the normal to the scanned plane σ_{ρ_n} has the following form

$$\sigma_{\rho_n} = \sigma_\rho(\rho) \cos \alpha = \text{const} \quad \forall \alpha \in [0^\circ, 80^\circ] \quad (3.11)$$

we can infer that

$$\sigma_\rho(\rho) = \frac{\sigma_{\rho,\text{fix}} + \rho \sigma_{\rho,\text{prop}}}{\cos \alpha} \quad (3.12)$$

The physical reason is the elongated footprint of the laser beam on the illuminated surface (Soudarissanane et al., 2009).

Furthermore, for short-range monitoring applications, $\sigma_{\rho,\text{prop}}$ is often negligible with respect to the total error budget, because of the short distances between the sensor and the monitored structure. In fact, for SHM applications, the measured ranges are often shorter than 10 m, and the order of magnitude of $\sigma_{\rho,\text{prop}}$ is 10 ppm.

The VCM of every point is then expressed in the global reference system G , by left and right multiplication by the rotation matrix \mathbf{R} , which features along its columns the coordinates of the orthonormal triple of directions $(\hat{\rho}, \hat{t}_v, \hat{t}_h)$, expressed in the global reference system, as follows:

$$\mathbf{R} = \left[\begin{array}{c|c|c} \hat{\rho}^G & \hat{t}_v^G & \hat{t}_h^G \end{array} \right] \quad (3.13)$$

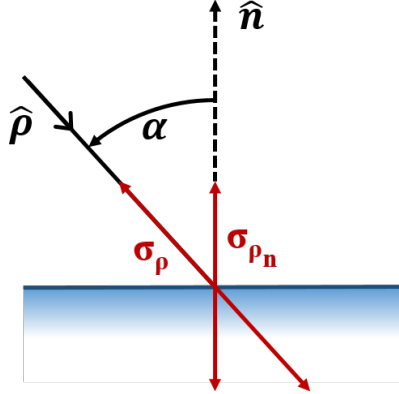


Figure 3.12: Cosine deterioration of σ_ρ , depending on the incidence angle α

$$\Sigma_P^G = \mathbf{R}\Sigma_P^L\mathbf{R}^\top \quad (3.14)$$

In reality, besides the incidence angle of the laser beam, there is a plethora of other factors affecting the accuracy of a TLS-measured point, e.g. the recorded intensity and the roughness of the target. However, no definitive quantitative models exist yet. A first step towards the quantification of the effects of the recorded intensity on the range accuracy has been proposed by Wujanz et al. (2017).

3.3.1. Variance propagation

The most straightforward approach to address the determination of the VCM of an interpolant is the classic variance propagation starting with the full VCM of the known values i.e. the observed coordinates of the points within the point cloud, including all the correlations among them. However, in this case, if the interpolant is not local (i.e. it is a function of all the known values) and the numerical derivatives required for the variance propagation cannot be derived analytically, this solution may be computationally very expensive. In fact, in this case, numerical differentiation with respect to each of the three coordinates of thousands of points may be necessary when processing TLS point cloud data.

As the interpolation strategy described by eqns. 3.3 and 3.4 is local, the variance propagation can be performed analytically by derivation of δ_N with respect to all the parameters of the vector \mathbf{x} , which contains only the coordinates of the vertices of a single triangle of the Delaunay triangulation:

$$\sigma_{\delta_N}^2 = \left(\frac{\partial \delta_N}{\partial \mathbf{x}} \right)^T \Sigma_{ABC} \left(\frac{\partial \delta_N}{\partial \mathbf{x}} \right) \quad (3.15)$$

where \mathbf{x} is defined as in 3.4, and Σ_{ABC} is a 9×9 block matrix with the three 3×3 VCMs of the vertices of the triangle ABC along its main diagonal, as follows.

$$\Sigma_{ABC} = \begin{bmatrix} \Sigma_A & \mathbf{0} & \mathbf{0} \\ \mathbf{0} & \Sigma_B & \mathbf{0} \\ \mathbf{0} & \mathbf{0} & \Sigma_C \end{bmatrix} \quad (3.16)$$

The nine derivatives $\frac{\partial \delta_N}{\partial \mathbf{x}}$ are shown in eqns.3.18 to 3.26. D is an auxiliary variable to make the notation lighter.

$$D = (x_A(y_C - y_B) + x_B(y_A - y_C) + x_C(y_B - y_A))^2 \quad (3.17)$$

$$\frac{\partial \delta_N}{\partial x_A} = \frac{[(x_N(y_C - y_B) + x_B(y_N - y_C) + x_C(y_B - y_N)) (y_A(z_C - z_B) + y_B(z_A - z_C) + y_C(z_B - z_A))]}{D} \quad (3.18)$$

$$\frac{\partial \delta_N}{\partial x_B} = \frac{[(x_N(y_C - y_B) + x_B(y_N - y_C) + x_C(y_B - y_N)) (y_A(z_C - z_B) + y_B(z_A - z_C) + y_C(z_B - z_A))]}{D} \quad (3.19)$$

$$\frac{\partial \delta_N}{\partial x_C} = \frac{[(x_N(y_A - y_B) + x_A(y_B - y_N) + x_B(y_N - y_A)) (y_A(z_B - z_C) + y_B(z_C - z_A) + y_C(z_A - z_B))]}{D} \quad (3.20)$$

$$\frac{\partial \delta_N}{\partial y_A} = \frac{[(x_N(y_B - y_C) + x_B(y_C - y_N) + x_C(y_N - y_B)) (x_A(z_B - z_C) + x_B(z_C - z_A) + x_C(z_A - z_B))]}{D} \quad (3.21)$$

$$\frac{\partial \delta_N}{\partial y_B} = \frac{[(x_N(y_A - y_C) + x_A(y_C - y_N) + x_C(y_N - y_A)) (x_A(z_B - z_C) + x_B(z_C - z_A) + x_C(z_A - z_B))]}{D} \quad (3.22)$$

$$\frac{\partial \delta_N}{\partial y_C} = \frac{[(x_N(y_A - y_B) + x_A(y_B - y_N) + x_B(y_N - y_A)) (x_A(z_C - z_B) + x_B(z_A - z_C) + x_C(z_B - z_A))]}{D} \quad (3.23)$$

$$\frac{\partial \delta_N}{\partial z_A} = \frac{-x_N y_B + x_N y_C + x_B y_N - x_B y_C - x_C y_N + x_C y_B}{-x_A y_B + x_A y_C + x_B y_A - x_B y_C - x_C y_A + x_C y_B} \quad (3.24)$$

$$\frac{\partial \delta_N}{\partial z_B} = \frac{x_N(y_C - y_A) + x_A(y_N - y_C) + x_C(y_A - y_N)}{x_A(y_B - y_C) + x_B(y_C - y_A) + x_C(y_A - y_B)} \quad (3.25)$$

$$\frac{\partial \delta_N}{\partial z_C} = \frac{-x_N y_A + x_N y_B + x_A y_N - x_A y_B - x_B y_N + x_B y_A}{-x_A y_B + x_A y_C + x_B y_A - x_B y_C - x_C y_A + x_C y_B} \quad (3.26)$$

The three derivatives of δ_N with respect to the z components of **A**, **B** and **C** coincide with the barycentric weights shown in formula 3.3. Hereby, the correlation which may occur between the interpolated displacements if the respective triangles share one, two or three vertices is neglected, as well as the correlations between the coordinates of the triangle's vertices. Both are simplifications that may be dropped in the future, in case (i) valid and numerically tractable correlation models of the coordinates in a point cloud are developed, and (ii) it turns out that taking into account the correlations is necessary for practically useful results. Recent insight in this field has been provided by Kermarrec et al. (2019), who fitted NURBS to TLS point clouds for deformation monitoring purposes. The authors hinted that the correlation among the points of the point cloud cannot be overlooked especially when the scanning geometry is not favourable (i.e. the incidence angles are large). Another recent contribution to the topic is by Schmitz et al. (2020), who showed that performing a scan with very high resolution and low accuracy settings can significantly reduce the number of uncorrelated points within the acquired point cloud.

The outcome of the actual implementation of the variance propagation performed with the outlined method showed some unexpected results. More concretely, some values of the variance propagation are lower than the expected minimum value. Indeed, restricting eqn. 3.15 to the unidimensional case (see eqn. 3.27), a lower bound for σ_{δ_N} is $\min\{\sigma_{z_A}, \sigma_{z_B}, \sigma_{z_C}\}/\sqrt{3}$, when the node N is located in the centroid of the triangle ABC and therefore all the partial derivatives $\frac{\partial \delta_N}{\partial z_A}$, $\frac{\partial \delta_N}{\partial z_B}$, and $\frac{\partial \delta_N}{\partial z_C}$ are equal to $\frac{1}{3}$.

$$\sigma_{\delta_N}^2 = \begin{bmatrix} \frac{\partial \delta_N}{\partial z_A} & \frac{\partial \delta_N}{\partial z_B} & \frac{\partial \delta_N}{\partial z_C} \end{bmatrix} \cdot \begin{bmatrix} \sigma_{z_A}^2 & 0 & 0 \\ 0 & \sigma_{z_B}^2 & 0 \\ 0 & 0 & \sigma_{z_C}^2 \end{bmatrix} \cdot \begin{bmatrix} \frac{\partial \delta_N}{\partial z_A} \\ \frac{\partial \delta_N}{\partial z_B} \\ \frac{\partial \delta_N}{\partial z_C} \end{bmatrix} \quad (3.27)$$

This problem has been observed to arise when the local normal of the Delaunay triangulation is approximately perpendicular to the direction along which the δ_N is calculated. This happens when the noise level of the measurements is large, i.e. $\sigma_\rho \geq 5$ mm for the scenario described in 4.2. A possible reason is that the derivatives $\frac{\partial \delta_N}{\partial x}$ and $\frac{\partial \delta_N}{\partial y}$ may become very large and therefore prone to yield numerical errors. Although more research is needed to find the causes of this issue, a pragmatic approach has been adopted. The nodes of which the σ_{δ_N} is smaller than the stated lower bound are simply removed from the analysis. For all the tested scen-

arios, their number is very small compared to the total amount of points available, e.g. this effect impacts less than the 0.8 % of the nodes for $\sigma_\rho = 5$ mm.

3.3.2. Log-Euclidean interpolation of the VCM

The methods based on averaging several positive-semidefinite tensors are local, and they can be adapted to triangular interpolants. Such methods have been developed especially in the field of diffusion tensor imaging (DTI)¹ for medical applications (see e.g. Hotz et al., 2010; Pusz and Woronowicz, 1975), and a review on them is provided by Yang et al. (2012). Among them, the log-Euclidean interpolation as presented by Arsigny et al. (2006) has been adopted herein, because of its particular simplicity and computational efficiency. A distinguishing characteristic of this method is the absence of the Euclidean swelling effect, which can be intuitively described as follows: when averaging two symmetric positive-definite matrices, the determinant of the result turns out to be larger than the ones of the original two matrices. More precisely, the log-Euclidean interpolation consists of a weighted average $\bar{\Sigma}$ of n VCMs, according to the following formula:

$$\bar{\Sigma} := \exp \left(\sum_{i=1}^n w_i \ln(\Sigma_i) \right) \quad (3.28)$$

where the weights w_i are suitably chosen, e.g. the normalised areal coordinates shown in formula 3.3. The natural logarithm of each VCM Σ_i is obtained by extracting the natural logarithm of each eigenvalue \mathbf{d}_{ij} and successively recomposing the positive-semidefinite matrix as follows:

$$\Sigma = \mathbf{B}^T \mathbf{D} \mathbf{B} \quad (3.29)$$

$$\tilde{\mathbf{d}}_{ij} = \begin{cases} \ln(\mathbf{d}_{ij}) & \text{if } i = j \\ 0 & \text{if } i \neq j \end{cases} \quad (3.30)$$

$$\ln(\Sigma) := \mathbf{B}^T \tilde{\mathbf{D}} \mathbf{B} \quad (3.31)$$

Here \mathbf{B} is the square matrix of the eigenvectors, while \mathbf{D} and $\tilde{\mathbf{D}}$ are the diagonal matrices of the eigenvalues of Σ and $\ln(\Sigma)$, respectively. The variances $\sigma_{\delta_N}^2$ of the interpolated perpendicular distances are then calculated by projecting the VCMs along the normal direction \mathbf{n} , which is the unit vector in the direction of the analysed displacements, as follows:

$$\sigma_{\delta_N}^2 = \mathbf{n}^T \cdot \bar{\Sigma} \cdot \mathbf{n} \quad (3.32)$$

¹In the field of DTI, the spatial distribution of anisotropic water diffusion in biological tissues is studied. For an overview, see the work of Le Bihan et al. (2001).

The result obtained with this approach is an approximation of the VCMs that is expected if the scanned points would coincide with the projections of the FE nodes onto the interpolated surface.

3.3.3. Nearest neighbour interpolation

The third investigated method to assign a VCM to the interpolated displacements is the nearest neighbour search, which is an intermediate solution between interpolating onto the nodes and onto the measured points, as the interpolation locations are actually the nodes, but only a selection of them is used, i.e. the closest ones to each measurement point, within a certain distance threshold. The NN approach is applied on a plane whose normal coincides with the direction in which the displacements are analysed. For each FE node the closest measured point is searched, and its 2D Euclidean distance is computed. Only the TLS points lying at a distance below a predetermined threshold are kept for the following computations. This threshold should be chosen in such a way that the same measured displacement is not assigned to several nodes. For example, if the FE nodes are regularly distributed on the surface of the structure, the optimal size of the circle is half the spacing of the nodes. In such a way, the number of nodes included in the interpolation is maximised, under the condition that multiple assignments are avoided.

With a NN approach, an increase of the scanning resolution generally turns into an increase in the number of FE nodes to which a deformation is assigned, until all the visible FE nodes are "monitored", i.e. are associated to a measurement. Further increases of the resolution cause a reduction of the average distance between the FE nodes and the measured points.

Moreover, if a nearest neighbour approach is employed, a preventive screening and filtering of the noise of the point cloud is recommended, because potential errors in the estimation of the accuracy of a single measured point may be fully transferred to the accuracy of the nodal displacements δ_N . For example, a noisy point cloud could lead to a wrong calculation of the local incidence angle and thus affecting the quantification of the cosine-dependent signal degradation (see eqn. 3.12).

3.3.4. Comparison of the interpolation approaches

A comparison of the performance of the presented interpolation methods is provided herein figs. 3.13 and 3.14 for an exemplary case of the simulation described in section 4.2. Moreover, the processing time needed to perform the calculations for the three presented methods is summarised in tab. 3.1.

As fig. 3.14 shows, the accuracy of the point cloud to be interpolated are almost constant across the whole surface of the scanned structure, as the vertical standard deviation of its points range between 1 and 1.012 mm. Since the scanner is located below the centre of the beam, the points closer to the beam ends have been acquired with a larger incidence angle indeed. Moreover, in fig. 3.14 the effect of the removal of skinny triangles is visible at the border of the scanned beam.

method	variance propagation	log-Euclidean	nearest neighbour
time [s]	1.28	83.74	0.15

Table 3.1: Interpolation methods: comparison of processing time

Although the most mathematically rigorous, the variance propagation method delivers results that may seem counter-intuitive (see fig. 3.13b). Because of the assumption of uncorrelatedness among the points of the point cloud, the variance propagation approach return values of σ_{δ_N} systematically lower than the measured ones. Indeed, the value of σ_{δ_N} depends primarily on the relative position of the node N with respect to the vertices A , B and C (see fig. 3.8), i.e. the weights in eqn. 3.3.

Differently from the variance propagation approach, both the log-Euclidean interpolation and the nearest neighbour search deliver results that smoothly interpolate the input data. However, none of the two methods is outright superior to the other. For instance, the log-Euclidean interpolation assigns variances to a denser set of nodal displacements, because within the NN approach the number of nodes cannot exceed the number of acquired points.

Furthermore, when comparing the computational effort needed by the tested methods, the NN search is the fastest one, while the log-Euclidean interpolation is more than 500 times slower (see tab. 3.1).

The bottom line of this comparison is that, although all the three approaches are viable, the engineer should choose the one that fits best with the assumptions and purposes of the concrete application case. For example, variance propagation may lead to underestimation of the variance of the nodal displacements if the uncorrelatedness of the input cannot be guaranteed. In the simulations and application presented further in this work, the NN approach has been pragmatically adopted, because of its computational efficiency and aptness to the assumption of uncorrelated measurements.

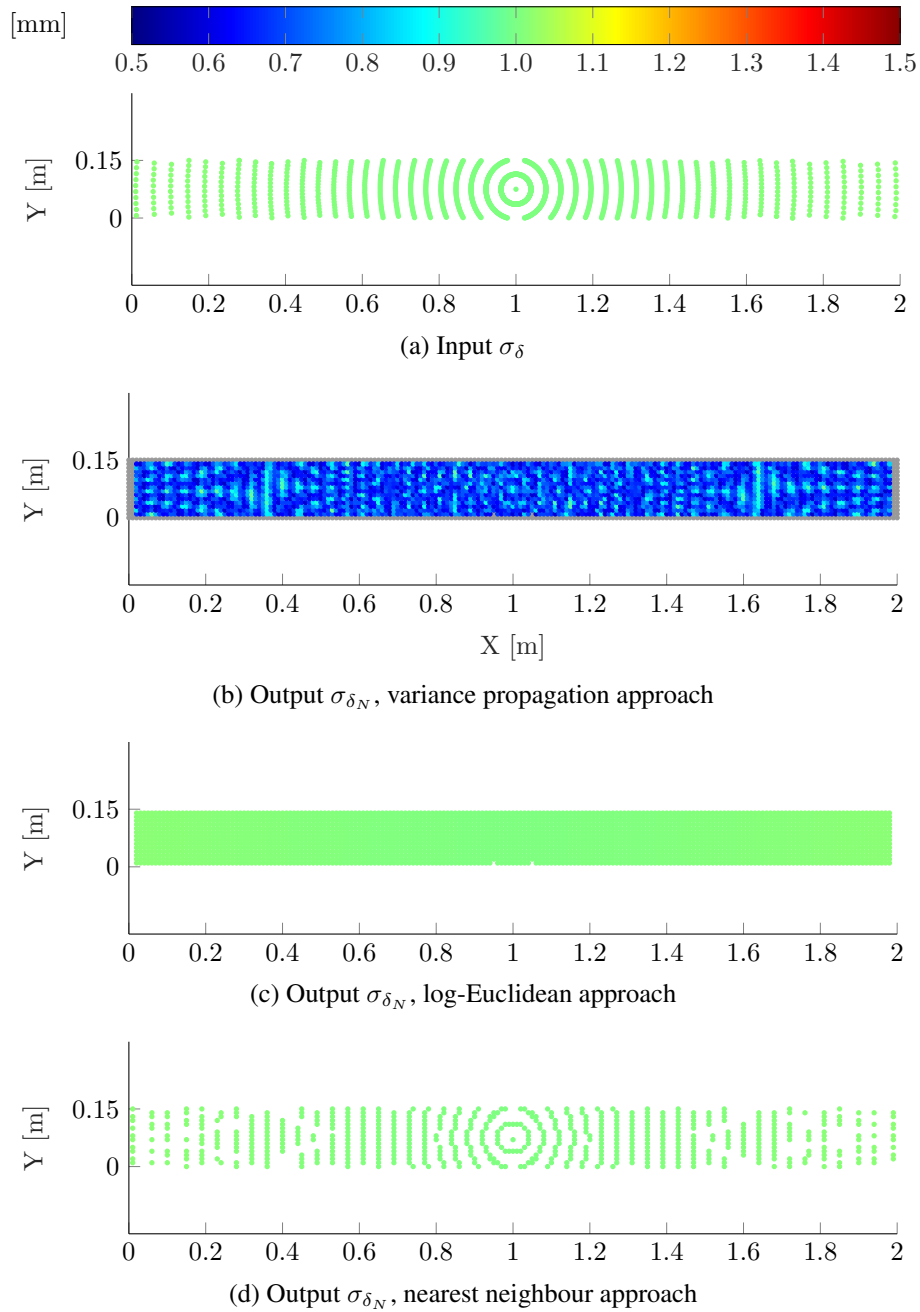


Figure 3.13: Variance propagation (b), Log-Euclidean (c), and Nearest Neighbour (d) interpolation outcomes for common input data (a). The FE nodes are colour-coded according to their value of σ_{δ_N}

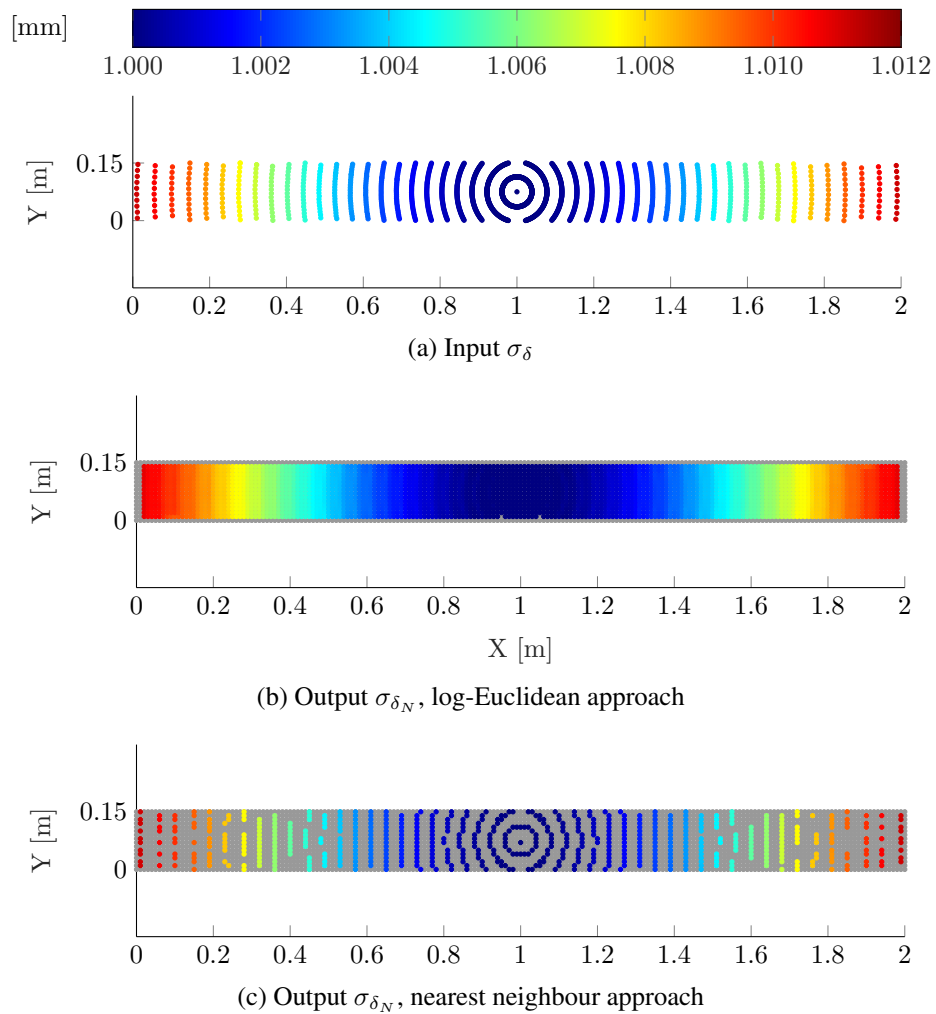


Figure 3.14: Same content of fig. 3.13 (a), (b), and (c) with a different colour bar to better highlight how the log-Euclidean and the NN approaches perform. The FE nodes are colour-coded according to their value of σ_{δ_N} . In grey, the FE nodes locations that have no displacement associated

3.4. Estimation of parameters

3.4.1. Integrated monitoring

The interpolation of measurements and their accuracies described in this chapter is used to calculate the displacements in correspondence of the FE nodes, in order to identify the mechanical properties of the investigated structure. Although the identification problem has been defined as different from the inverse problem of back analysis (see fig. 3.1), inversion techniques are needed for its solution. When facing an inversion problem, many approaches can be adopted, such as regression, Bayesian inference, sequential Monte Carlo, or searching for the best parameters with gradient descent or grid search methods. In this work, as optimisation method, the least squares adjustment scheme has been adopted, in order to follow the idea of integrated monitoring (Chrzanowski et al., 1991), as implemented by Lienhart (2007).

The LSA, which comes in a closed-form expression, is the most established regression method within the geodetic community because of its computational efficiency and the fact that it yields the maximum likelihood estimate in linear models with normally distributed observations. Moreover, several extensions (e.g. outlier detection, study of reliability) can be easily implemented.

More formally, the LSA follows the Gauss-Markov model for weighted observations is (Niemeier, 2012)

$$F(\hat{\boldsymbol{\xi}}) = \mathbf{y} + \mathbf{e}, \quad e_j \in \mathcal{N}(0, \boldsymbol{\Sigma}_j) \quad (3.33)$$

For the i -th iteration, after a linearisation of the functional model (Taylor, 1st order) in proximity of the point $\boldsymbol{\xi}_i$, the LSA is solved iteratively with respect to $d\hat{\boldsymbol{\xi}}_i = \hat{\boldsymbol{\xi}}_i - \boldsymbol{\xi}_i^0$. Herein, the subscript i indicates the i -th iteration, the superscript 0 indicates the linearisation point, the hat $\hat{}$ denotes an estimated value, and the subscript 0 represents an a-priori value.

$$\underbrace{\frac{\partial F(\boldsymbol{\xi})}{\partial \boldsymbol{\xi}^\top}}_{\mathbf{A}_i} \bigg|_{\boldsymbol{\xi}=\boldsymbol{\xi}_i^0} d\hat{\boldsymbol{\xi}}_i = \underbrace{\mathbf{y} - F(\boldsymbol{\xi}_i)}_{d\mathbf{y}_i} + \mathbf{e}_i, \quad e_i \in \mathcal{N}(0, \boldsymbol{\Sigma}_{yy}) \quad (3.34)$$

$$\mathbf{P} = \sigma_0^2 \boldsymbol{\Sigma}_{yy}^{-1} \quad (3.35)$$

$$d\hat{\boldsymbol{\xi}}_i = (\mathbf{A}_i^\top \mathbf{P} \mathbf{A}_i)^{-1} \mathbf{A}_i^\top \mathbf{P} d\mathbf{y}_i \quad (3.36)$$

$$\boldsymbol{\Sigma}_{\hat{\boldsymbol{\xi}}_i \hat{\boldsymbol{\xi}}_i} = s_{0_i}^2 (\mathbf{A}_i^\top \mathbf{P} \mathbf{A}_i)^{-1} \quad (3.37)$$

$$s_{0_i} = \sqrt{\frac{\mathbf{e}_i^\top \mathbf{P} \mathbf{e}_i}{r}} \quad (3.38)$$

$$\hat{\xi}_i = \xi_{i+1}^0 + d\hat{\xi}_i \quad (3.39)$$

where

- \mathbf{A} is the design matrix, i.e. the Jacobian of the observations with respect to the sought parameters;
- ξ^0 is the vector of the parameters at the linearisation point;
- $\hat{\xi}$ is the vector of the estimated parameters;
- $d\hat{\xi}$ is the vector of the estimated reduced parameters;
- \mathbf{y} is the vector of observations;
- $d\mathbf{y}$ is the vector of reduced observations;
- \mathbf{e} is the vector of the residuals, i.e. the random deviations;
- \mathbf{P} is the weight matrix;
- σ_0 is the a-priori variance per unit weight;
- Σ_{yy} is the variance-covariance matrix of the observations;
- $\Sigma_{\hat{\xi}\hat{\xi}}$ is the variance-covariance matrix of the estimated parameters;
- s_0 is the a-posteriori variance per unit weight;
- r is the redundancy of the system, calculated as the difference between the number of rows and columns of \mathbf{A} , i.e. the difference between the number of observations and the number of parameters.

As for the convergence threshold on $\hat{\xi}$ to stop the iteration, Niemeier (2012) suggests to set it below the desired precision of the parameters (e.g. few mm for geodetic networks). Without a predefined required level of precision, a reasonable alternative criterion to stop the iterations is the ratio between the change of the parameters $d\hat{\xi}_i$ and its standard deviation; the former should be at least one order of magnitude smaller than the latter. Within this work, a difference of three orders of magnitude has been employed as criterion, as formalised in eqn. 3.40:

$$\min(|d\hat{\xi}_i \oslash \sqrt{\text{diag}(\Sigma_{\hat{\xi}\hat{\xi}})}|) < 1\% \quad (3.40)$$

where the symbol \oslash represents the element-wise division. In this case, the latest update of the parameters modifies the distribution of the residuals only by a negligible amount.

Summarising, the identification algorithm is composed of two main steps: (i) the linearisation of the FE model with respect to the sought parameters, and (ii) the actual search of best fit parameters in terms of the sum of the squared residuals with a least squares adjustment. Corresponding to the proposed method of integrated monitoring as implemented by Lienhart (2007), the actual observation equations included in the LSA and their associated covariance matrices are the following:

$$\mathbf{d}_{\text{meas}} + \mathbf{e}_{\text{meas}} = \mathbf{d}_{\text{FEM}}(\hat{\mathbf{u}}), \Sigma_{dd,\text{meas}} \quad (3.41)$$

$$\mathbf{u}_{\text{sys}} + \mathbf{e}_{\text{sys}} = \hat{\mathbf{u}} - \mathbf{K}(\hat{\mathbf{p}})^{-1}\hat{\mathbf{f}}, \Sigma_{\text{sys}} \quad (3.42)$$

$$\mathbf{p}_0 + \mathbf{e}_p = \hat{\mathbf{p}}, \Sigma_{pp} \quad (3.43)$$

$$\mathbf{f}_0 + \mathbf{e}_f = \hat{\mathbf{f}}, \Sigma_{ff} \quad (3.44)$$

where

- \mathbf{d}_{meas} are the geodetic observations; in this work, they are the displacements of the surface δ_N , interpolated from the scan data as explained in section 3.3;
- \mathbf{d}_{FEM} are values corresponding to \mathbf{d}_{meas} , calculated from the nodal displacements; in this thesis, they are the displacements of a subset of the FE nodes, orthogonal to the reference surface;
- \mathbf{u}_{sys} are pseudo-observations of the nodal displacements of the FE model, which are set to be zero, for the reason further explained in the text;
- \mathbf{p}_0 are the a-priori values of the material parameters;
- \mathbf{f}_0 are the a-priori values of the forces;
- $\hat{\mathbf{u}}$ are the estimated nodal displacements;
- $\hat{\mathbf{p}}$ are the estimated material parameters;
- $\hat{\mathbf{f}}$ are the estimated nodal forces;
- \mathbf{K} is the stiffness matrix of the FE model;
- $\Sigma_{dd,\text{meas}}$, Σ_{pp} , Σ_{ff} , and Σ_{sys} are the VCMs of the corresponding variables.

The eqn. 3.41 (*measurement part*) links the actual observations to the nodal displacements of the FE model and depends on the type of sensors employed, while the eqn. 3.42 (*system part*) describe the behaviour of the FE model and therefore account for the knowledge about the structure and its properties. The eqn. 3.43 and 3.44 are stochastic constraints that state the prior knowledge about the forces and the material parameters, respectively. In fact, Σ_{pp} and Σ_{ff} are used to quantify the uncertainty of the initial values of the parameters and forces, respectively.

As a result, the vectors $d\hat{\boldsymbol{\xi}}$ and $d\mathbf{y}$, the design matrix \mathbf{A} and the covariance matrix of the observations Σ_{yy} for a given iteration are as follows (iteration count i omitted for readability):

$$d\hat{\boldsymbol{\xi}} = \begin{bmatrix} d\hat{\mathbf{u}} \\ d\hat{\mathbf{p}} \\ d\hat{\mathbf{f}} \end{bmatrix} = \begin{bmatrix} \hat{\mathbf{u}} - \mathbf{u} \\ \hat{\mathbf{p}} - \mathbf{p} \\ \hat{\mathbf{f}} - \mathbf{f} \end{bmatrix} \quad (3.45)$$

$$\mathbf{A} = \begin{bmatrix} \frac{\partial \mathbf{d}_{\text{meas}}}{\partial \mathbf{u}} & & \\ \mathbf{I} & -\frac{\partial \mathbf{u}(\mathbf{p}, \mathbf{f})}{\partial \mathbf{p}} & -\frac{\partial \mathbf{u}(\mathbf{p}, \mathbf{f})}{\partial \mathbf{f}} \\ & \mathbf{I} & \\ & & \mathbf{I} \end{bmatrix} = \begin{bmatrix} \mathbf{A}_u & & \\ \mathbf{I} & \mathbf{A}_p & \mathbf{A}_f \\ & \mathbf{I} & \\ & & \mathbf{I} \end{bmatrix} \quad (3.46)$$

$$d\mathbf{y} = \begin{bmatrix} \mathbf{d}_{\text{meas}} - \mathbf{d}_{\text{FEM}}(\mathbf{u}) \\ \mathbf{0} \\ \mathbf{p}_0 - \mathbf{p} \\ \mathbf{f}_0 - \mathbf{f} \end{bmatrix} \quad (3.47)$$

$$\Sigma_{yy} = \begin{bmatrix} \Sigma_{dd, \text{meas}} & & & \\ & \Sigma_{\text{sys}} & & \\ & & \Sigma_{pp} & \\ & & & \Sigma_{ff} \end{bmatrix} \quad (3.48)$$

where \mathbf{u} denotes the set of nodal displacements, \mathbf{p} the material parameters, and \mathbf{f} the nodal forces².

The block \mathbf{A}_u of the matrix \mathbf{A} in eqn. 3.46 contains the derivatives of the geometric observations with respect to the nodal displacements e.g. the strain measured at certain locations as in (Lienhart, 2007), or the displacements in certain directions as herein. In fact, in this work, the interpolation and the calculation of the VCM for a subset of the surface nodal displacements is solved beforehand, as described in section 3.3. Therefore, the block \mathbf{A}_u of the matrix \mathbf{A} is an identity matrix.

Conversely, for many observation types, it is possible to include the interpolation step directly in the LSA. If such a strategy had been adopted in this work, the observations would have consisted directly in the acquired point clouds, and also the input Σ_{yy} would have explicitly included the variances and covariances of the TLS observations instead of the output of the VCM interpolation. Nevertheless, the linearisation of some interpolation schemes would have turned particularly complex. This holds for example, when the interpolation is performed by employing a nearest neighbour search, which is non-differentiable.

The elements within the diagonal variance matrix Σ_{sys} should be chosen some orders of magnitude smaller than the elements along the diagonal of the rest of Σ_{yy} . In fact, the eqn. 3.42 is included for the sole purpose of connecting the measurements with the material parameters and the forces. Theoretically, the relation

$$\mathbf{0} = \mathbf{u} - \mathbf{K}(\mathbf{p})^{-1}\mathbf{f}$$

should be included as a condition to be fulfilled into the LSA. Including it instead as a set of pseudo-observations is conceptually more straightforward and adds flexib-

²In (Lienhart, 2007), the matrices \mathbf{A}_p and \mathbf{A}_f are denoted as $-\mathbf{T}_{up}$ and $-\mathbf{T}_{uf}$, respectively

ility in case of model uncertainty. Indeed, choosing low variances for these pseudo-observations lets them act practically as if they were conditions and tie the solution to the linearised model. However, at the same time, the magnitude of the diagonal elements within Σ_{sys} has to be sufficiently big to prevent the ill-conditioning of the normal matrix $\mathbf{A}^T \mathbf{P} \mathbf{A}$, which has to be inverted in eqn. 3.37. In this work, the entries of Σ_{sys} have been set to be 4 orders of magnitude smaller than the smallest element on the diagonal of Σ_{yy} , and no ill-conditioning has been observed.

In the developed Matlab code, the calculations have been generally performed using units of the international system (SI), for the sake of clarity and simplicity. With this regard, it was noticed that the design matrix \mathbf{A} of the LSA can contain rather large values, depending on the stiffness of the structure. For example, the entries of \mathbf{A} can reach values of the order of 10^{12} Pa/m in case of steel structures. The vastly different orders of magnitude of the non-zero elements in \mathbf{A} may lead to numerical issues e.g. a quasi-singular normal matrix. Even if such values do not jeopardise the algorithm for the tested application examples, the numerics within the LSA have been modified and improved by changing the unit of measurement of \mathbf{p} and Σ_{pp} so that the numerical values of the variances within Σ_{pp} have the same order of magnitude of the ones within Σ_{yy} . In this way, entries of Σ_{sys} have approximately the same relative weight with respect to both Σ_{pp} and Σ_{yy} . Moreover, numerical values of the partial derivatives of the parameters with respect to each observation are closer to the unity, thus reducing the numerical errors when estimating very "stiff" parameters, which are scarcely sensitive to the observations, e.g. the Young modulus of a very rigid material.

Throughout this thesis, only the displacements and material parameters are estimated within the LSA, i.e. $\boldsymbol{\xi} = \left[\frac{d\hat{\mathbf{u}}}{d\hat{\mathbf{p}}} \right]$. In fact, the focus has been laid on the problem of identification rather than on the back analysis problem (see fig. 3.1), because the former is of greater interest within the field of SHM. Even if there are concrete applications of the back analysis problem for structures whose behaviour remains in the linear elastic region (e.g. the estimation of static wind loads), the main application field of back analysis is probably forensic engineering, which often deals with plasticisation and failure modes. Moreover, only Young's moduli E have been estimated, because it is the main parameter determining the mechanical behaviour of structural elastic members. Apart from the above-mentioned reasons, these limitations of the analysis have also been motivated by the time constraints. It would be extremely interesting to extend the evaluation of the method beyond these boundaries.

A further important assumption made is that the geometry of the undeformed structure (i.e the size of the FE elements and their connectivity) is considered constant across different measurement epochs. Indeed, especially when dealing with the monitoring of damaged structures, the variability (in space or in time) of the stiffness of a structure can be physically due to a local reduction of the cross sectional surface due to phenomena such as delamination or corrosion, to discontinuities in the mechanical continuum due to cracking or fatigue, or to an actual reduction of the

material stiffness due to processes such as plasticising. However, at a macroscopic scale, any of the mentioned phenomena has been interpreted as the latter case, i.e. a change of E .

3.4.2. Pre-elimination

Since the most time-consuming part of the analysis is the FE evaluation and not the calculation of the LSA, in his analysis Lienhart (2007) included all the nodal displacements in the linearisation of the FE model within the LSA, i.e. the partial derivatives of eqn. 3.42 within the design matrix \mathbf{A} have been calculated for all the nodes of the FE model. Although the same is valid for the work presented herein, a reduction of the dimension of the design matrix \mathbf{A} can be beneficial in respect to (i) the RAM usage when storing the matrices involved in the LSA, especially when inverting the normal matrix, and (ii) the reading of the nodal displacements from text files. In order to reduce the computational burden of the two mentioned stages, the nodal displacements involved in the LSA can be selectively chosen thanks to a pre-elimination (Niemeier, 2012) of the parameters which are not of interest or are not involved in the interpolation process.

More concretely, the vector of nodal displacements \mathbf{u} can be split in two complementary subsets \mathbf{u}_{obs} and $\mathbf{u}_{\text{-obs}}$. The former contains the nodal displacements that have been observed, and the latter includes the nodal displacements that have no associated observed value.

If the elements within \mathbf{u} are permuted as shown, the quantities $d\hat{\xi}$, \mathbf{A} , $d\mathbf{y}$, and Σ_{yy} can be rearranged then as follows:

$$d\hat{\xi} = \begin{bmatrix} d\hat{\mathbf{u}}_{\text{obs}} \\ d\hat{\mathbf{p}} \\ \hline d\hat{\mathbf{u}}_{\text{-obs}} \end{bmatrix} = \begin{bmatrix} \hat{\mathbf{u}}_{\text{obs}} - \mathbf{u}_{\text{obs}} \\ \hat{\mathbf{p}} - \mathbf{p} \\ \hline \hat{\mathbf{u}}_{\text{-obs}} - \mathbf{u}_{\text{-obs}} \end{bmatrix} = \begin{bmatrix} d\hat{\xi}_1 \\ \hline d\hat{\xi}_2 \end{bmatrix} \quad (3.49)$$

$$\mathbf{A} = \begin{bmatrix} \mathbf{A}_u & \mathbf{0} & \mathbf{A}_{u\text{-obs}} \\ \mathbf{I} & \mathbf{A}_{p\text{obs}} & \mathbf{0} \\ \mathbf{0} & \mathbf{A}_{p\text{-obs}} & \mathbf{I} \\ \mathbf{0} & \mathbf{I} & \mathbf{0} \end{bmatrix} = \begin{bmatrix} \mathbf{A}_1 \\ \hline \mathbf{A}_2 \end{bmatrix} \quad (3.50)$$

$$d\mathbf{y} = \begin{bmatrix} \mathbf{d}_{\text{meas}} - \mathbf{d}_{\text{FEM}}(\mathbf{u}) \\ \mathbf{0} \\ \mathbf{0} \\ \mathbf{p}_0 - \mathbf{p} \end{bmatrix} \quad (3.51)$$

$$\mathbf{P} = \sigma_0^2 \boldsymbol{\Sigma}_{yy}^{-1} = \sigma_0^2 \begin{bmatrix} \boldsymbol{\Sigma}_{dd, \text{meas}} & & & \\ & \boldsymbol{\Sigma}_{\text{sys, obs}} & & \\ & & \boldsymbol{\Sigma}_{\text{sys, } \neg \text{obs}} & \\ & & & \boldsymbol{\Sigma}_{pp} \end{bmatrix}^{-1} \quad (3.52)$$

For simplicity of representation, differently than eqn. 3.45, the vector of the observations does not include the nodal forces \mathbf{f} . If they are included in the analysis, they behave exactly like the material parameters \mathbf{p} .

It is possible to notice that, within the block matrix \mathbf{A} (see eqn. 3.50), $\mathbf{A}_{u \neg \text{obs}} = \mathbf{0}$, according to the provided definition of $\mathbf{u}_{\neg \text{obs}}$. Moreover, the second element in the block vector $d\mathbf{y}$ is zero, as it represents the discrepancies between the measured deformations \mathbf{d}_{meas} and their FE-derived equivalents ones \mathbf{d}_{FEM} .

As a result, it can be shown that the pre-elimination of the non observed nodal displacements $d\mathbf{u}_{\neg \text{obs}}$ from the vector $d\hat{\boldsymbol{\xi}}$ does not affect the estimation of the remaining parameters.

Niemeier (2012) shows how the parameters $d\hat{\boldsymbol{\xi}}_1$ can be estimated separately from the parameters $d\hat{\boldsymbol{\xi}}_2$ according to the following formula

$$d\hat{\boldsymbol{\xi}}_1 = \underbrace{(\mathbf{N}_{11} - \mathbf{N}_{12}\mathbf{N}_{22}^{-1}\mathbf{N}_{21})^{-1}}_{\mathbf{Q}_{11}} \mathbf{A}_1^\top \mathbf{P} d\mathbf{y} \quad (3.53)$$

where \mathbf{Q}_{11} is the cofactor matrix, and the normal matrix \mathbf{N} is subdivided as follows

$$\mathbf{N} = \begin{bmatrix} \mathbf{N}_{11} & \mathbf{N}_{12} \\ \mathbf{N}_{21} & \mathbf{N}_{22} \end{bmatrix} = \begin{bmatrix} \mathbf{A}_1^\top \mathbf{P} \mathbf{A}_1 & \mathbf{A}_1^\top \mathbf{P} \mathbf{A}_2 \\ \mathbf{A}_2^\top \mathbf{P} \mathbf{A}_1 & \mathbf{A}_2^\top \mathbf{P} \mathbf{A}_2 \end{bmatrix} \quad (3.54)$$

Similarly, the a-posteriori VCM of the parameters is

$$\boldsymbol{\Sigma}_{\hat{\boldsymbol{\xi}}_1 \hat{\boldsymbol{\xi}}_1} = s_0 \mathbf{Q}_{11} \quad (3.55)$$

After the substitution of the matrix blocks shown in eqn. 3.46 in eqn. 3.53,

$$d\hat{\boldsymbol{\xi}}_1 = \begin{bmatrix} \mathbf{A}_u^\top \boldsymbol{\Sigma}_{dd, \text{meas}}^{-1} \mathbf{A}_u + \boldsymbol{\Sigma}_{\text{sys, obs}}^{-1} & \boldsymbol{\Sigma}_{\text{sys, obs}}^{-1} \mathbf{A}_{p, \text{obs}} \\ \mathbf{A}_{p, \text{obs}}^\top \boldsymbol{\Sigma}_{\text{sys, obs}}^{-1} & \mathbf{A}_{p, \text{obs}}^\top \boldsymbol{\Sigma}_{\text{sys, obs}}^{-1} \mathbf{A}_{p, \text{obs}} + \boldsymbol{\Sigma}_p^{-1} \end{bmatrix}^{-1} \begin{bmatrix} \mathbf{A}_u^\top \boldsymbol{\Sigma}_{dd, \text{meas}}^{-1} (\mathbf{d}_{\text{meas}} - \mathbf{d}_{\text{FEM}}(\mathbf{u})) \\ \boldsymbol{\Sigma}_p^{-1} (\mathbf{p}_0 - \mathbf{p}) \end{bmatrix} \quad (3.56)$$

which is the same expression that can be obtained by not including \mathbf{u}_{obs} in the LSA as follows

$$d\hat{\xi} = \begin{bmatrix} d\hat{\mathbf{u}}_{\text{obs}} \\ d\hat{\mathbf{p}} \end{bmatrix} = \begin{bmatrix} \hat{\mathbf{u}}_{\text{obs}} - \mathbf{u}_{\text{obs}} \\ \hat{\mathbf{p}} - \mathbf{p} \end{bmatrix} \quad (3.57)$$

$$\mathbf{A} = \begin{bmatrix} \mathbf{A}_u & \mathbf{0} \\ \mathbf{I} & \mathbf{A}_{p\text{obs}} \\ \mathbf{0} & \mathbf{I} \end{bmatrix} \quad (3.58)$$

$$d\mathbf{y} = \begin{bmatrix} d_{\text{meas}} - d_{\text{FEM}}(\mathbf{u}) \\ \mathbf{0} \\ \mathbf{p}_0 - \mathbf{p} \end{bmatrix} \quad (3.59)$$

$$\mathbf{P} = \sigma_0^2 \Sigma_{yy}^{-1} = \sigma_0^2 \begin{bmatrix} \Sigma_{dd,\text{meas}} & & \\ & \Sigma_{\text{sys,obs}} & \\ & & \Sigma_{pp} \end{bmatrix}^{-1} \quad (3.60)$$

Of course, if one is also interested in the nodal displacements of the whole structure, it is possible to calculate them by running the FE evaluation one more time with the estimated $\hat{\mathbf{p}}$ and $\hat{\mathbf{f}}$ as parameters. This could be the case when the monitoring requirements include the inference of either stresses, strains or displacements of parts of the structure that have not been directly monitored. With the computational efficiency in mind, the LSA should include only the nodal displacements that have been observed (\mathbf{u}_{obs}).

3.4.3. Partitioning of the structure

According to the presented identification scheme, \mathbf{p} can be either a scalar when a single parameter is estimated, or a vector that encompasses several parameters. In fact, \mathbf{p} does not necessarily include one or several entries per FE element, since it can be typically assumed that multiple elements share the same value of the parameter. The entries of \mathbf{p} can denote one or more distinct mechanical parameters (e.g. the Young modulus and the Poisson ratio) for one or more different partitions of the structure. The size and shape of the partitions have to be chosen with engineering judgement. For example, the borders among partitions should possibly trace expected actual discontinuities in the structure's material properties, such as different layers within a composite material, or successive concrete pourings within a cast concrete structural member. Lacking specific assumptions, in this work the partitions have been created by automatically subdividing the analysed structures according to a regularly spaced 3D grid. A simple example of partitioning is depicted in fig. 3.15.

3.4.4. Closed-loop validation

In this section, an initial performance analysis of the LSA is provided, as a more in-depth discussion is given in sections 4.2, and 4.3, where simulations that also

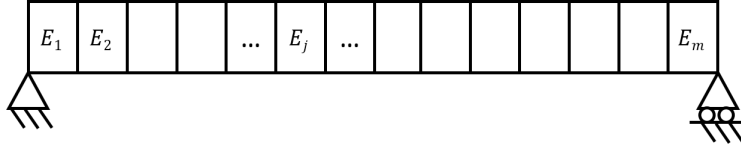


Figure 3.15: Exemplary sketch of the subdivision of a structure. In this case, a simply supported beam subdivided along only one dimension

include the scanning are analysed, and in section 4.4, where a concrete use case is detailed.

Closed loop simulations have been conducted, in order to investigate the dependency of the results with respect to:

- the noise level of the measurements, which have been assumed constant for all the observations;
- the number of the partitions;
- the a-priori values of the parameters \mathbf{p}_0 , which have been assumed uniform for all the partitions;
- the a-priori values of the accuracy of the parameters, which have been assumed uniform for all the partitions.

The influence of the first three inputs listed above has been tested by varying them for a selection of scenarios. The results of these closed-loop validation tests are shown in figs. 3.16 to 3.19. Differently, the influence of Σ_{pp} on the stochastic results of the LSA has been investigated with a Monte Carlo simulation, which is described separately in the following section 3.4.5.

The test setup described herein is similar to the one described in section 4.2, but instead of generating the scan data and interpolating the measured displacements, these displacements have been simulated directly. Consistently with the assumptions stated in section 3.3, the measurements are considered uncorrelated, i.e. $\Sigma_{dd} = \sigma_d^2 \mathbf{I}$. As for the properties of the structure, the beam is 2 m long, and simply-supported. The cross section is 25 mm high and 150 mm wide, and the loads acting on the beam are the self-weight ($\rho = 7850 \text{ kg/m}^3$) and a vertical concentrated load of 4 kN at midspan. The concentrated load has been distributed among all the nodes belonging to the midspan cross section, in order to reduce the stress concentration in the model. The beam has been partitioned along its main axis in sections of equal length (see fig. 3.15), and the Young's modulus E_{true} is equal to 210 GPa for all partitions.

For the scenarios analysed in this section, the a-priori accuracy of the parameters is equal for all the simulations, i.e. $\Sigma_{pp} = \sigma_{E_0}^2 \mathbf{I}$, with $\sigma_{E_0} = 10 \text{ GPa}$. For each combination of σ_d and E_0 , the scenario has been analysed for the nine numbers of partitions (1, 2, 3, 4, 6, 8, 12, 24, and 36). The figs. 3.16 to 3.19 show for every partition the value of \hat{E} with a round marker, and the associated accuracy with a

vertical error bar that spans from $\hat{E} - \sigma_{\hat{E}}$ to $\hat{E} + \sigma_{\hat{E}}$.

Sensitivity to the noise level of the measurements

The first remark on the sensitivity to the noise level of the measurements is that, as expected, an increase of σ_d entails a growth of the standard deviation of the estimations as well. This can be seen by comparing fig. 3.16 with fig. 3.17. This is especially noticeable for a low number of partitions, because when there are many of them (12 or more) all the σ_E are very close to σ_{E_0} anyway, thus not improving the knowledge about them.

Concerning the value obtained for $\sigma_{\hat{E}}$, the positive outcome is that, for all the simulated cases, E_{true} lies within the 1σ error bars. The measurements with $\sigma_d = 1$ mm, which are technically feasible, helps to improve the knowledge of E for a single partition significantly beyond the assumed initial uncertainty of $\sigma_{E_0} = 10$ GPa, and still provides some contribution for the case of 2 partitions and for the central one in case of 3 partitions.

On the other hand, the proposed method also shows some limitations. In fact, $\sigma_d = 1$ mm is not accurate enough for estimating E with a spatial resolution smaller than 0.7 m. However, this finding needs to be put into perspective: a deformation of 2 m long steel beam with this shape under this load does not cause mm-level variations of the deformations over short distances. Thus, TLS is not appropriate as measuring system, and this is to be expected.

Sensitivity to the a-priori information on the parameters

The results of the LSA are sensitive to the a-priori information on the parameters \mathbf{p}_0 , even if their a-priori covariances Σ_{pp} is very large.

The effects of a deviation of E_0 from E_{true} can be seen by comparing fig. 3.16 and fig. 3.18. These two figures present the results of two simulations that differ only in the value of the initial guess of the material parameters. The former figure shows the values of \hat{E} and $\sigma_{\hat{E}}$ for $E_0 = E_{\text{true}}$, while the latter for $E_0 = E_{\text{true}} + 10$ MPa. As expected, the comparison indicates that a value of E_0 that strongly deviates from the true one could lead to wrong estimates for the partitions of the structure that show a low sensitivity to the measurements, for instance close to the pinned supports of a simply supported beam. The larger the deviation $E_0 - E_{\text{true}}$, larger the error in the least sensitive partitions.

The choice of E_0 is crucial because, besides the stochastic constraints (see eqn. 3.43), also the initial guess of the parameters within the LSA plays a role. Indeed, in the first iteration of the LSA, an initial guess of each parameter has to be chosen (see eqn. 3.36), which reasonably coincides with their a-priori value \mathbf{p}_0 .

However, when solving for a large number of partitions with rather homogeneous material properties, this issue can be overcome by first running an identification for just one partition for simple objects like a beam or a plate, and then subsequently

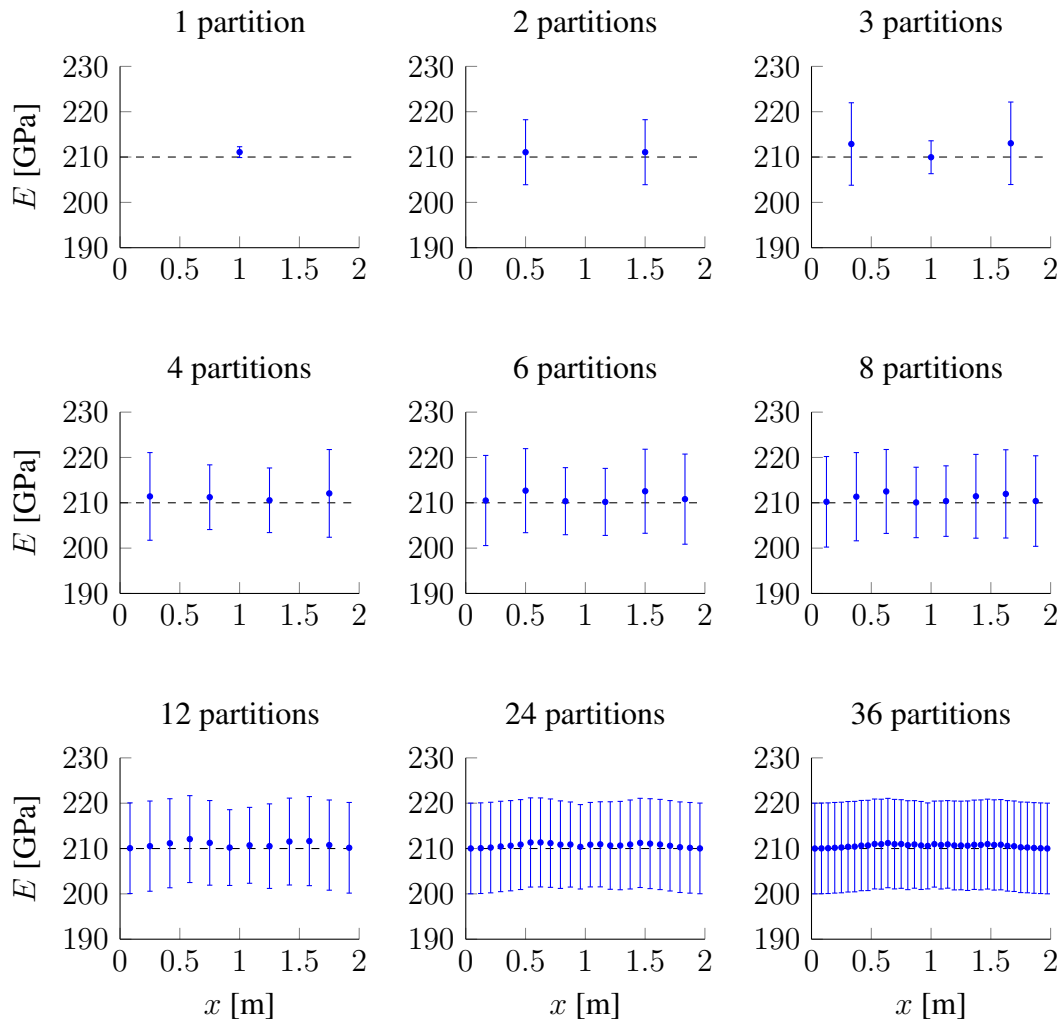


Figure 3.16: Result of a closed loop simulation with $\sigma_d = 1$ mm, and $E_0 = 210 \pm 10$ GPa. The horizontal axes show the position along the 2 m long beam, while the vertical axes represent the estimated Young modulus of each partition, in GPa. The vertical error bars depict the 1σ confidence interval for each partition. The dashed black line represents the value of the ground truth $E_{\text{true}} = 210$ GPa

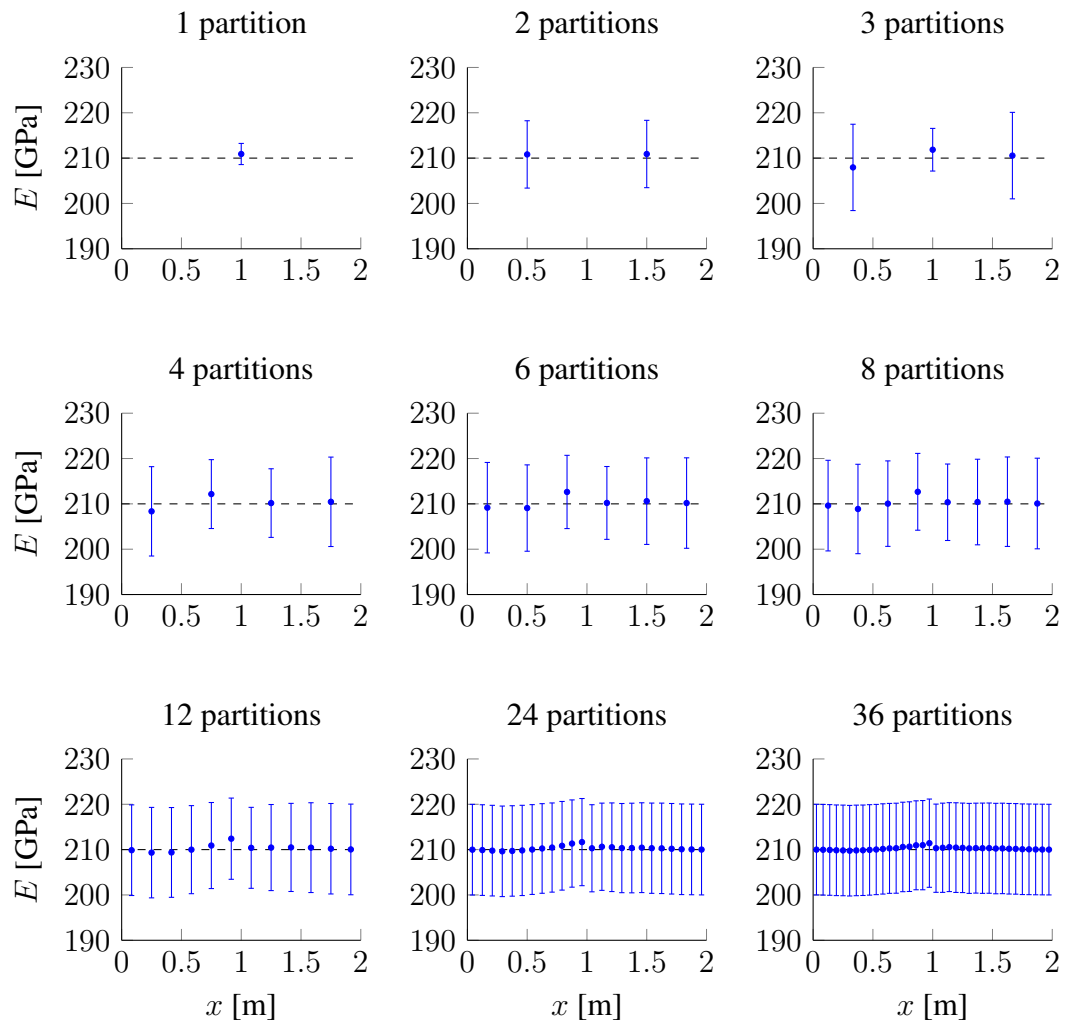


Figure 3.17: Same situation as in fig. 3.16 but with increased measurement noise of $\sigma_d = 2$ mm

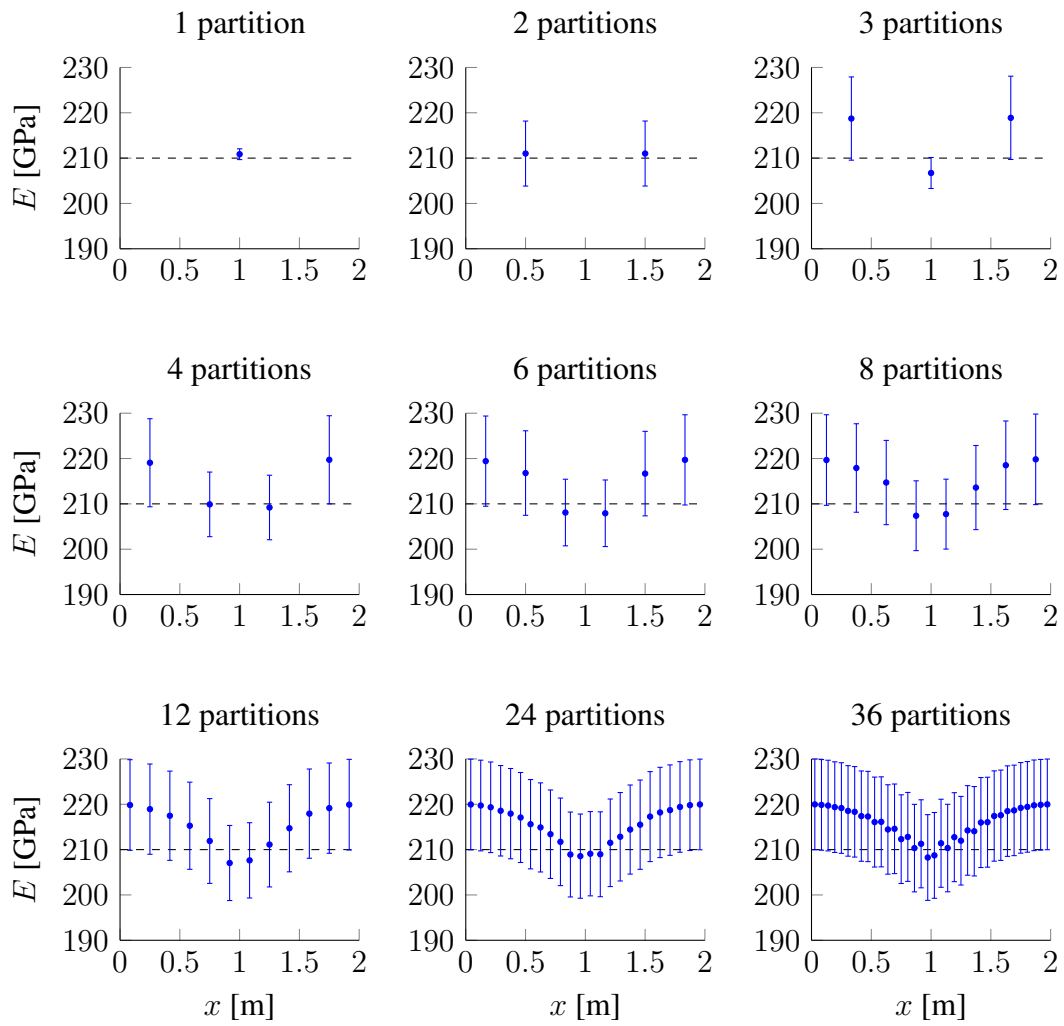


Figure 3.18: Same situation as in fig. 3.16 but with a different initial value $E_0 = 220 \pm 10$ GPa

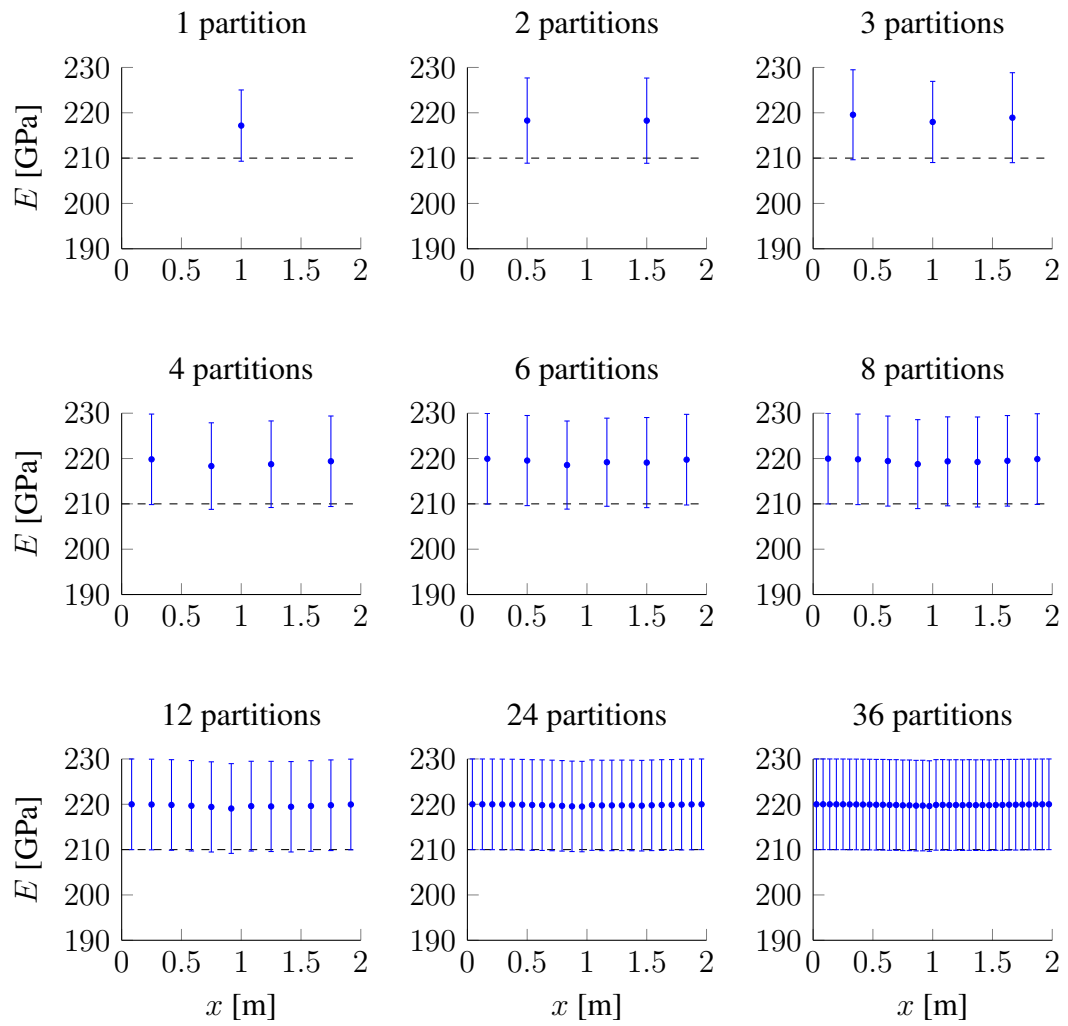


Figure 3.19: Same situation as in fig. 3.18 but with increased measurement noise of $\sigma_d = 10$ mm

adopt the resulting value of the parameter as initial guess.

Sensitivity to the number of partitions

The effects of a different number of partitions is visible in each of the figs. 3.16 to 3.19. The most evident outcome is that an increasing number of partitions leads to an increase in $\sigma_{\hat{E}}$. In particular, the difference in $\sigma_{\hat{E}}$ between the case for 1 partition or multiple ones is striking. More precisely, for a value of $\sigma_d = 1$ mm, the ratio $\sigma_{\hat{E}}/E_{\text{true}}$ amounts to 0.5% for one partition, 3.4% for two partitions, and 1.7% for the central partition of three. For a value of $\sigma_d = 2$ mm instead, the ratio $\sigma_{\hat{E}}/E_{\text{true}}$ is 1.1% for one partition, 3.4% for two partitions, and 2.3% for the central partition of three.

Moreover, one can clearly see that the dependence of \hat{E} on the initial value E_0 varies depending on the position of the partition along the beam. For example, this is visible in fig. 3.18, where the initial conditions E_0 are set to 220 GPa, for all the partitions, while $E_{\text{true}} = 210$ GPa. The beam is more sensitive to changes of E at midspan than close to the supports, because the bending moment has a parabolic trend along the simply supported beam, with a maximum at midspan and null value at the beam ends. Thus, as expected, \hat{E} of the least sensitive partitions remain close to the value of E_0 , while the \hat{E} of the most sensitive partitions are much closer to value of E_{true} . This effect gets more evident for a larger number of partitions. In the simulations with at least 3 partitions shown in fig. 3.18, even an "overshooting" effect is visible. The most sensitive partitions show an underestimated \hat{E} , compensating the overestimation of the least sensitive one due to $E_0 > E_{\text{true}}$.

For very large numbers of partitions (see fig. 3.18, 36 partitions), \hat{E} shows a wave-like pattern along the x direction. This is likely due to the anticorrelation between the parameters of neighbouring partitions (see fig. 4.8).

Another observation that can be drawn from figs. 3.16, 3.18, and 3.19 is that the subdivision of the structure in a large number of partitions leads to the a-posteriori covariances of the parameters $\Sigma_{\hat{p}\hat{p}}$ to be equal to the a-priori ones Σ_{pp} , without improving them. A clear example is visible for the case of 36 partitions in fig. 3.19.

In fact, while estimating the material parameters for a large number of partitions, if the a-priori knowledge about the material parameters is very vague (i.e. the entries within Σ_{pp} are very large), the weight of the geometrical observations \mathbf{d} is larger than the weight of the pseudo-observations \mathbf{p} . This is consistent with the idea of the whole analysis - the LSA should be driven by the measurements if they are sufficiently accurate to improve the initial estimates. In the analysed case, the estimated values of material parameters of the different partitions are strongly correlated (see fig. 4.8) and hardly separable. The reason is that different distributions of the parameters E across the structure lead to very similar deformed configurations, leading to a scattered distribution of \hat{E} driven by the noise of the geometrical observations. This issue could be addressed in future improvements of the implementation of the LSA by adding stochastic constraints also on the difference of \mathbf{p} between nearby

partitions.

The scatter could be theoretically so large that during the iterative LSA one or more \hat{E}_i are estimated as negative, and no FE evaluation for the numerical calculation of the local gradient would be possible anymore. Negative Young's moduli have indeed no physical meaning. In addition, from a rigorous point of view, depending on the type of parameters, the support of the a-priori probability density distribution of the material parameters may not extend to an infinite interval for physical reasons. For example, meta-materials aside, elastic moduli cannot be negative and Poisson ratios are limited within the range $[0, 0.5]$. In fact, when the a-priori uncertainty on a parameter is much larger than the parameter itself, the assumption of its normality may not be plausible anymore. Besides the use of a distribution with a probability density function that is supported on a semi-infinite interval, a first possible measure to overcome this issue is the definition of a location dependent σ_p across the structure's partitions, decreasing its value in proximity of the least sensitive areas. Alternatively, the size of the partitions can be chosen adaptively i.e. with a higher resolution where the sensitivity is higher.

Lastly, in figs. 3.16, 3.18 and 3.19 it is possible to notice that, when subdividing the beam into two partitions, the standard deviation of E is (i) much larger than the case with only one partition, (ii) approximately independent of the measurement noise level σ_d , and (iii) larger than the accuracy of the central partition when subdividing the beam in 3 partitions. The last finding may appear counterintuitive, as σ_E could be expected to grow monotonically when increasing the number of partitions. The reason behind is that, given the symmetry of the monitored beam used as a study case, estimating E for two partitions instead for one does not result in an increased degree of freedom of the solution, as the estimated parameters are strongly correlated.

3.4.5. Monte Carlo validation

The correctness of the stochastic output of the proposed LSA has been validated with a Monte Carlo (MC) closed-loop simulation. The idea is to sample the a-priori parameters \mathbf{p}_0 according to a freely chosen, yet plausible, dispersion Σ_{pp} , and then to compare the empirical dispersion of the estimated parameters with their formal one.

The used scenario is very similar to the one employed for the simulations described in section 3.4.4, and the only difference is that the validation has been conducted for two values of σ_{E_0} (10 and 20 GPa). The beam has been partitioned along its main axis in 4 sections of equal length (see fig. 3.15, with $m = 4$); thus, \mathbf{p} contains four Young's moduli, one for each partition, i.e. $\mathbf{p} = [E_1, E_2, E_3, E_4]$. The size of the sample amounts to 300 repetitions. The reason of this number, which is rather low, were time constraints.

The parameters are sampled according to the following distribution:

$$\mathbf{p}_0 \in \mathcal{N}(\mathbf{p}_{\text{true}}, \Sigma_{pp}) \quad (3.61)$$

where \mathbf{p}_{true} are the actual values of the parameters used for the generation of the synthetic scenarios.

The results of the Monte Carlo simulations are presented in tab. 3.2. They confirm that the stochastic output of the LSA is correct, because the deviations of \hat{E} from the value of E_{true} are well within the estimated $\sigma_{\hat{E}}$. Moreover, the \hat{E} are correlated with the sampled values of E_0 , as expected. The empirical standard deviations of the sample s_{E_0} do not exactly coincide with $\sigma_{E_0} = 210$ MPa because of the finite number of samples.

The average a-posteriori standard deviation $\bar{s}_{\hat{E}}$ and the empirical standard deviation of the 300 estimated \hat{E} match quite consistently, as their difference never exceeds 7%, the value attained for the partition 1 in the scenario with $\sigma_{E_0} = 20$ GPa. In this worst case, the Fisher test statistic F is

$$F = \frac{\bar{s}_{\hat{E}}^2}{\bar{\sigma}_{\hat{E}}^2} = \frac{17.8^2}{16.6^2} = 1.1449$$

which corresponds to a p-value of 0.007, given that the numerator and the denominator degrees of freedom are 299 and 300, respectively.

Moreover, one can observe that $\bar{\sigma}_{\hat{E}}$ and $s_{\hat{E}}$ are larger for the partitions close to the supports (1 and 4) and smaller for the central ones (2 and 3). The reason is the different sensitivity of different portions of the structure to the geometric measurements, as already shown by the results presented in section 3.4.5.

	partition ID			
	1	2	3	4
$\bar{E}_0 \pm s_{E_0}$	209.3 \pm 10.1	210.3 \pm 9.5	210.4 \pm 10.5	210.2 \pm 10.0
$\bar{\hat{E}} \pm s_{\hat{E}}$	209.3 \pm 9.6	210.5 \pm 5.9	210.5 \pm 5.9	210.1 \pm 9.6
$\bar{\sigma}_{\hat{E}}$	9.2	5.8	6.0	9.4
$\bar{\sigma}_{\hat{E}}/s_{\hat{E}}$	96%	98%	102%	98%

(a) Scenario with $E_{\text{true}} = 210$ GPa, $\sigma_{E_0} = 10$ GPa

	partition ID			
	1	2	3	4
$\bar{E}_0 \pm s_{E_0}$	208.6 \pm 20.2	210.6 \pm 19.0	210.8 \pm 21.0	210.5 \pm 19.9
$\bar{\hat{E}} \pm s_{\hat{E}}$	208.7 \pm 17.8	211.0 \pm 8.9	210.9 \pm 8.8	210.1 \pm 17.8
$\bar{\sigma}_{\hat{E}}$	16.6	8.9	9.1	17.3
$\bar{\sigma}_{\hat{E}}/s_{\hat{E}}$	93%	100%	103%	97%

(b) Scenario with $E_{\text{true}} = 210$ GPa, $\sigma_{E_0} = 20$ GPa

Table 3.2: Results of the Monte Carlo validation. Herein, a bar on the top of a symbol denotes the average over the 300 samples, the symbol s denotes an empirical standard deviation, the symbol σ denotes a formal standard deviation. E_0 is the sampled a-priori parameter, while \hat{E} is the estimated value of the parameter within the LSA. The first row shows how the 300 samples approximate the scenario specifications, the second row describes the distribution of \hat{E} , and the third row the estimated standard variation of \hat{E} , averaged for the 300 repetitions.

3.5. Considerations on calculations

This section includes a collection the most relevant encountered numerical issues and insights about the calculation involved in the whole presented method. The section 3.5.1 provides the context to understand the sections 3.5.2 and 3.5.3.

3.5.1. Description of the Jacobian \mathbf{A}_p

The entries of the Jacobian matrix $\mathbf{A}_p = \frac{\partial \mathbf{u}}{\partial \mathbf{p}}$ (see eqn. 3.46) describe the sensitivity of the displacements to a change in E of each partition. The number of columns of the matrix m coincides with the number of partitions, while the number of rows n coincides with the number of observed nodal displacements.

The derivative is numerically determined by calculating the symmetric difference quotient

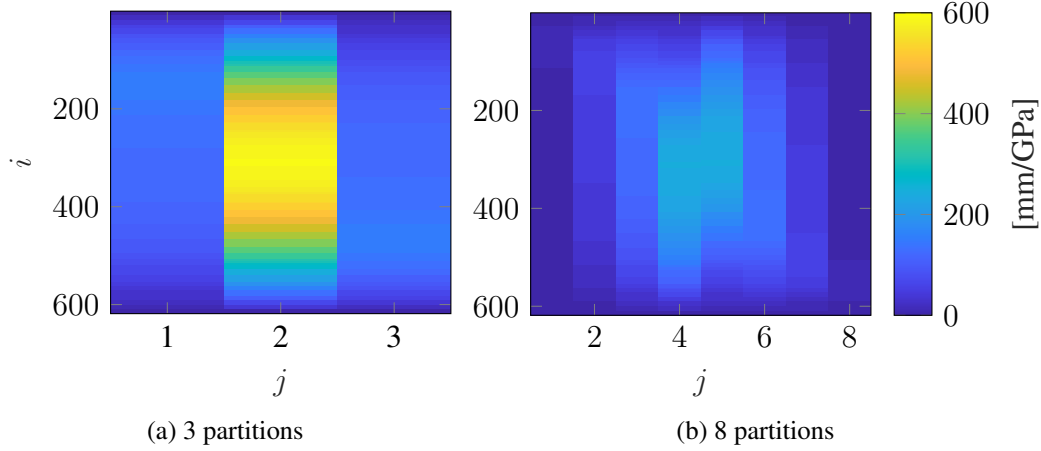


Figure 3.20: Visual representation of the entries of \mathbf{A}_p for different numbers of partitions. The two matrices are scaled horizontally differently, as they feature different numbers of columns

$$\frac{\partial u_i(\mathbf{p})}{\partial p_j} = \frac{u_i(\mathbf{p} - \Delta p \mathbf{e}_j) - u_i(\mathbf{p} + \Delta p \mathbf{e}_j)}{2\Delta p} \quad (3.62)$$

$\mathbf{p} \in \mathbb{R}^m; \quad i = 1, \dots, n; \quad j = 1, \dots, m$

or by calculating the one-sided difference quotient

$$\frac{\partial u_i(\mathbf{p})}{\partial p_j} = \frac{u_i(\mathbf{p}) - u_i(\mathbf{p} + \Delta p \mathbf{e}_j)}{\Delta p} \quad (3.63)$$

$\mathbf{p} \in \mathbb{R}^m; \quad i = 1, \dots, n; \quad j = 1, \dots, m$

where \mathbf{e}_j represents the j -th unit vector of an Euclidean canonical orthonormal basis $\{\mathbf{e}_1, \mathbf{e}_2, \dots, \mathbf{e}_n\}$, and Δp is the step size. In this work, Δp has been kept constant for all the elements of the vector \mathbf{p} . More information about the size of Δp is provided in section 3.5.3. Computationally, a single evaluation of the FE model is equivalent to determine $\mathbf{u} = \mathbf{u}(p_j)$, because for each parameter p_j , all the nodal displacements \mathbf{u} are calculated. Therefore, the calculation of a Jacobian matrix \mathbf{A}_p with m columns (i.e. a structure partitioned m times) needs $2m$ evaluations of the FE model if symmetric difference quotients are calculated. Differently, if one-sided numerical derivatives are employed, all the entries of \mathbf{A}_p share the evaluation point \mathbf{p} and, as a result, only $m + 1$ evaluations are needed. To reduce the computational effort, in this work only right derivatives have been calculated.

Two visual representations of \mathbf{A}_p are provided in fig. 3.20. The figures refer to a simply supported beam, the vertical displacements of which have been measured in 616 equally spaced locations along the beam's major dimension x . The estimated parameters are the Young modulus of each partition, and the two sub-figures (a) and (b) refer to a subdivision of the beam in 3 and 8 partitions, respectively. The

disposition of the partitions corresponds to the one shown in fig. 3.15, and the nodal displacements \mathbf{u} are arranged in the same order, i.e. according to their x coordinate. Consequently, each column of the two Jacobians represents the change in deformed shape of the beam subject to a local change in stiffness within the j -th partition. As expected, the highest values are primarily located in the centre of the matrix, where the partitions that mostly influence the deflection of the beam are located. Secondly, the values along the main diagonal are larger than the neighbouring ones because the effect of a change of stiffness of a partition has primarily effect on the nodes located in its proximity. Moreover, the matrix is symmetric because of the symmetry of the structure. Another visible property of the depicted Jacobians is that the sum of all the elements belonging to the i -th row is the same for both the matrices, even if they have a different number of partitions. In more formal terms, given a FE model and a set of observations, for two Jacobian matrices \mathbf{A}_p and \mathbf{A}_q with respectively m_p and m_q partitions:

$$\forall i \in \{1, \dots, n\} \quad \sum_{j=1}^{m_p} a_{p \ i,j} = \sum_{j=1}^{m_q} a_{q \ i,j} \quad (3.64)$$

3.5.2. Numerical precision of the Abaqus output files

A first numerical issue that can arise while exporting the nodal displacements from a FE solver, is their limited precision. Among the various ASCII output files provided by Abaqus, two of them are particularly convenient to output the nodal displacements: the Abaqus data (.dat) files returns the nodal displacements in a floating-point 5-digit representation with exponent, while the result (.fin) files provide the nodal displacements in double precision, i.e. with 15 to 17 significant digits. A floating-point 5-digit representation is suitable to describe the field of deformation with an acceptable level of precision, but when calculating the differences between fields of deformation (for example when computing the numerical derivatives \mathbf{A}_p) a variation of the displacement field smaller than 0.01% cannot be distinguished anymore. In fact, given the small sensitivity of the areas close to the supports, the values within the matrix \mathbf{A}_p may be impaired by quantisation errors. To overcome this issue, the Abaqus result .fin files have been used, the precision of which is sufficient for an accurate computation of \mathbf{A}_p .

In order to exemplify the importance of an adequate numerical precision, a practical case is shown in fig. 3.21. Herein, two data series show the vertical displacement of a node due to a change in stiffness of a single partition of a beam. The only difference between the two plotted data series in fig. 3.21 is the precision of the representation, which correspond to the aforementioned .dat and .fin Abaqus output files. The partition of the beam with variable stiffness is the leftmost one of 24, while the analysed node is located at midspan. The specifications of this simulation are the same for the closed-loop tests detailed in section 3.4.4, with the difference that no random deviations of the measured displacements have been modelled.

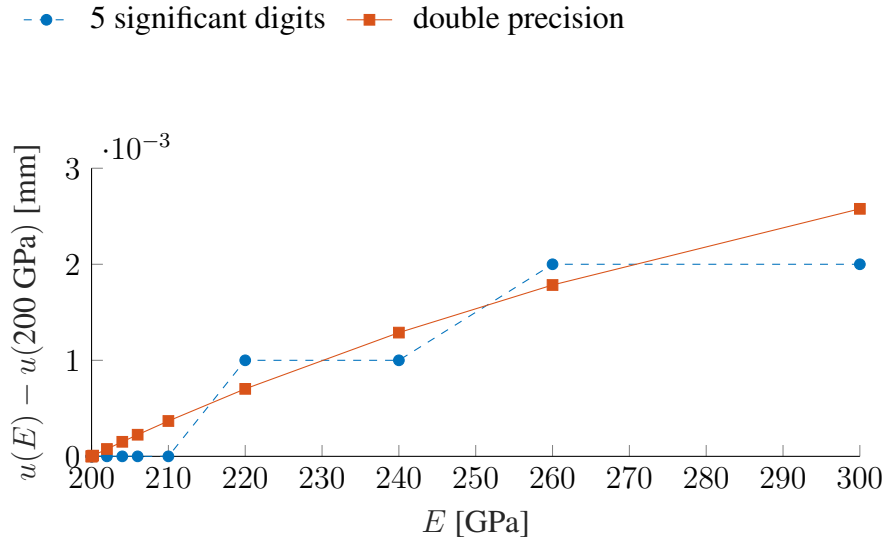


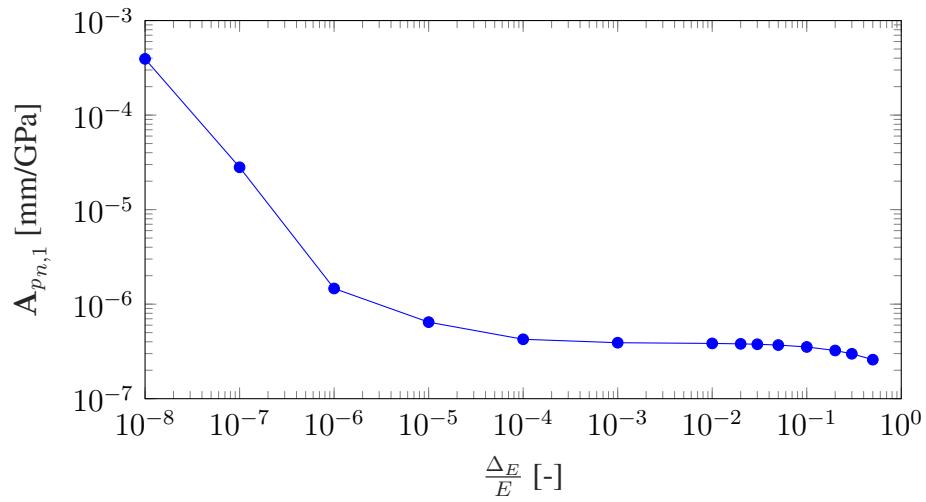
Figure 3.21: The function $\mathbf{u} = \mathbf{u}(E)$ for a single node of a 2 m long, simply supported beam. Examples of the effect of a limited machine precision on the evaluation of the nodal displacements and their numerical derivatives with respect to the material parameters

It is clearly visible that if the .dat output is used, the precision of nodal displacements is limited to 0.001 mm. Although such precision is sufficient for the calculation of reduced observations dy in the LSA (see eqn. 3.47), the quantisation effects would lead to a wrong computation of the design matrix \mathbf{A} . In fact, the difference quotients used to evaluate \mathbf{A}_p (see 3.63) would be affected by strong numerical errors, such as subtractive cancellation.

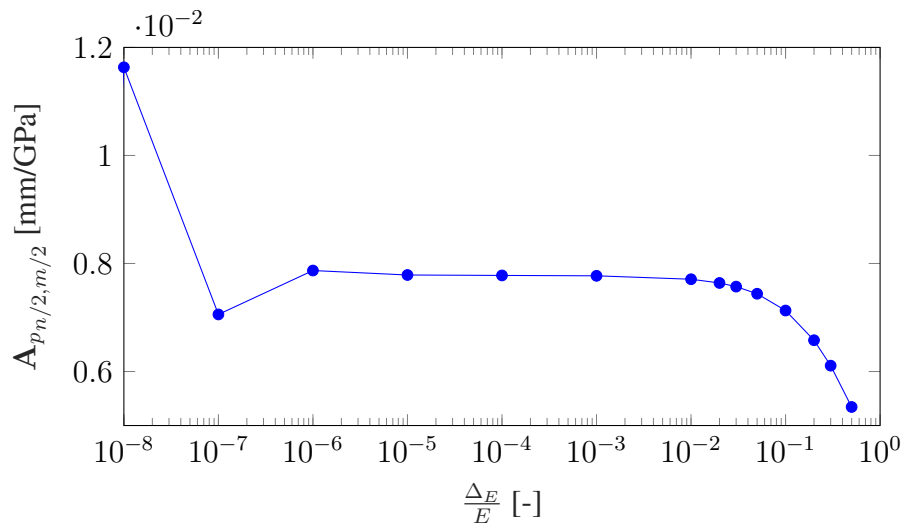
3.5.3. Step size for the numerical derivatives of a non-linear function

Since the function $\mathbf{u} = \mathbf{u}(E)$ for the simply supported beam described in section 4.2 is not linear ($\mathbf{u} \propto \frac{1}{E}$), the values of its numerically computed derivatives within \mathbf{A}_p vary depending on the step size Δp (see eqn. 3.63). Analytically, the smaller the step Δp , the more accurate is the estimation of the local derivative. However, if the step is too small, the numerator of the difference quotient may be comparable with the numerical precision of its machine representation (epsilon), i.e. the distance to the next floating point number, for an unchanged exponent (see fig. 3.21). The order of magnitude of the minimum step size that does not provoke such numerical errors has been determined empirically, by calculating the value of some selected elements of the Jacobian \mathbf{A}_p for various step sizes. Indeed, the entries of \mathbf{A}_p mostly affected by quantisation and flooring errors are the smallest ones, i.e. $\mathbf{A}_{p_{n,1}}$ and $\mathbf{A}_{p_{1,m}}$, which correspond to the bottom-left and top-right cells in each of the matrices depicted in fig. 3.20.

Fig. 3.22a depicts the value of $\mathbf{A}_{p_{n,1}}$ for different values of the relative step size



(a) The smallest entry within \mathbf{A}_p , logarithmic y axis



(b) The largest entry within \mathbf{A}_p , linear y axis

Figure 3.22: Search of a suitable step size for numerical differentiation. The effect of a varying relative step size $\frac{\Delta p}{p} = \frac{\Delta E}{E}$ on the numerical differentiation of two entries within \mathbf{A}_p . Case of a simply supported beam subdivided in 36 partitions

$\frac{\Delta p}{p} = \frac{\Delta E}{E}$. For comparison, also the corresponding values of the largest entry of \mathbf{A}_p is plotted in fig. 3.22b. It is possible to see show that for values of ΔE below $10^{-6} E$, the calculation of the numerical derivative becomes unstable. Conversely, for values of Δp growing above $10^{-2} E$, the one-sided difference quotient estimates the slope of a secant that progressively diverges from the local tangent. Therefore, the step size has been restricted within the range from $10^{-2} E$ to $10^{-4} E$, in order to get an accurate estimate of local derivative without triggering numerical errors.

3.5.4. Precision of the LSA implementation

The minimum magnitude of the noise on the observations that can be handled correctly by the LSA has been investigated. To do so, another closed-loop simulation has been performed and the ratio between the a-priori variance factor σ_0^2 and the a-posteriori one s_0^2 has been analysed.

The model used for this analysis is conceptually similar to the one described in section 3.4.4, although the size and the mechanical properties of the simulated beam are different. The simply-supported beam is 6 m long, with a rectangular cross section 30 cm wide and 40 cm high. The beam is loaded with 121 kN at mid-span, and the modelled material is linear isotropic ($E = 11$ GPa, $\nu = 0$). The beam is discretised with a single partition of C3D8 finite elements, each with a size of $5 \times 5 \times 5$ cm³. The observations consist of 197 displacements equally spaced along the centre of the beam's width, in correspondence of the location of the nodes. For each side, the two outermost nodes have been excluded from the analysis because of their limited displacements, because the extremities of the beam are vertically constrained.

The idea behind this analysis is that by progressively decreasing the noise on the observations, a set of residuals of the same order of magnitude of the numerical errors inherent in the proposed algorithm shall be eventually reached. If the VCM of the observations is correctly scaled, the expected value of the ratio $\frac{\sigma_0^2}{s_0^2}$ equals 1; otherwise, the ratio s_0^2/σ_0^2 diverges from the unity. For example, given $r = 196$ degrees of freedom, the χ^2 test is rejected with a significance level $\alpha = 0.05$ when the following inequality is true:

$$\frac{s_0^2}{\sigma_0^2} > \frac{\chi_r^2(1 - \alpha)}{r} = \frac{229.7}{196} = 1.17 \quad (3.65)$$

As shown in fig. 3.23, the algorithm and its LSA work properly for noise with an order of magnitude larger than 0.01 mm. For smaller noise levels, the χ^2 test is not satisfied anymore.

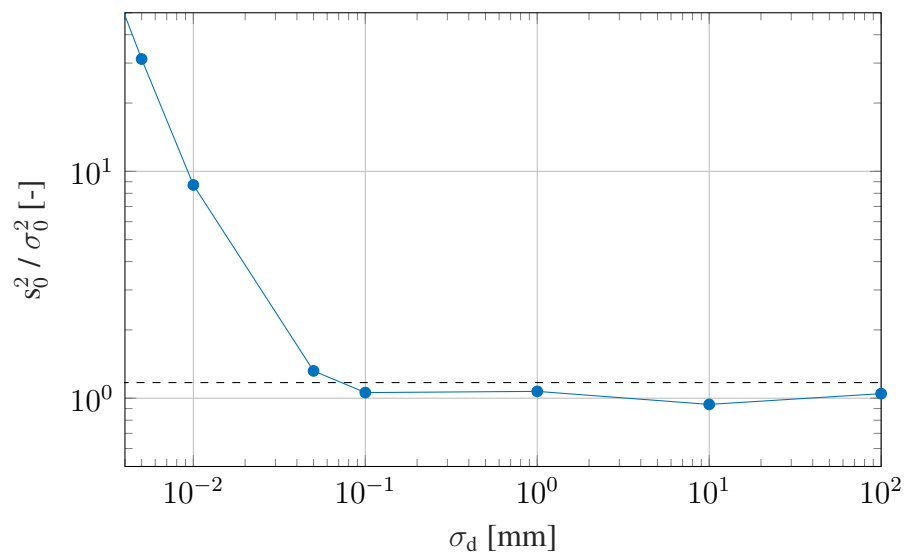


Figure 3.23: Ratio between the prior and the posterior variance factors, for different measurement noise magnitudes σ_d . The horizontal dashed line represents the value of the χ^2 test statistics $\frac{\chi_{197}^2(0.95)}{197}$

4. Application cases

In order to evaluate the strengths and limits of the proposed method, three application cases are presented herein: a steel beam, an alloy plate, and a cross-laminated timber (CLT) slab. The first two examples are based on synthetic data, whereas the third one is based on real data. Differently from the validation simulations detailed in sections 4.2 and 4.3, the synthetic application examples include the generation of realistic noisy point clouds. Moreover, the CLT slab is not the only real structure that has been monitored while developing this thesis. In fact, during an early stage of development of the presented identification method, the deformation of a snow structure has been analysed and the determination of its density and viscosity has been attempted (Serantoni et al., 2017). However, this experiment has not been included in the thesis as the employed method does not correspond to the formulation presented herein, and therefore does not represent a valid testing. Nevertheless, the gathered experience has been extremely useful for the definition of the methods' requirements and for circumventing major pitfalls that can be encountered in practice.

An important question to consider when interpreting the outcomes of the proposed method is: within which limits can an estimate of the material parameters be considered equal to the expected ones? Or in other words: what is the relationship between a certain structural damage and its effect on the estimation of the structure's stiffness? How big is a useful detection? The answer depends strongly on the kind of investigated structure, i.e. its geometry and its material. For example, let us take as model the steel beam that is been analysed in section 4.2. If a 1 mm thick uniform corrosion on a single face of a cross section takes place¹, the height of the cross section h decreases by 4%, determining a decrease of the flexural stiffness EJ of 11.5%. Indeed, the moment of inertia of a rectangular cross section is $J = \frac{bh^3}{12}$.

The application example presented herein has been designed with the following specifications in mind:

- the maximum displacements of the structure lie within the range of the accuracy typically achieved with a terrestrial laser scanner over distances of a few meters (approx. 1-5 mm), in order to analyse both the cases in which the signal-to-noise ratio for a single point of the point cloud is smaller or larger

¹Corrosion allowance defined by the norm ISO 9223 for weathering steel, corrosion class C3 for urban areas - mild class

than 1;

- the stress is kept below the yield point in the whole structure, so as to comply with the assumption of linear elastic material, as local non-elastic effects (e.g. cracks, plastic hinges) cannot be modelled by the employed FE model;
- a simple geometry and easily-definable boundary conditions, to provide for easy reproducibility in laboratory environment, in case of future real experiments.

Because of these specifications, the most suitable materials to be analysed are the one that can undergo large strains, i.e. they feature a large yield strain $\varepsilon_y = f_y/E$. For example, concrete is not a suitable material to be monitored because it can undergo only relatively moderate strain before cracking. Tab. 4.1 provides the main mechanical properties of some common construction materials mentioned throughout this thesis.

Table 4.1: A list of construction materials and their mechanical properties.

Material	E [GPa]	ν [-]	ρ [kg/m ³]	f_y [MPa]	ε_y [$\mu\varepsilon$]
Steel S235	210.0	0.30	7850	235	1119
Alum. alloy 5083	72.0	0.33	2650	228	3167
Concrete C25/30	31.5	0.20	2500	2.6 (tens.)	83
CLT C24	11.0	~0.4	436	24	2182

4.1. Numerical simulation tool

For the application cases described in sections 4.2 and 4.3, a numerical simulation tool has been employed, in order to validate the entire workflow of the structural identification, from the TLS data acquisition to the parameter estimation. This simulation tool integrates a generator of synthetic TLS point clouds upstream of the identification algorithm, as described in the previous chapter. This tool can be used for the following scopes:

- prediction of the expected accuracy of the results before the actual measurements, in analogy to the pre-analysis of geodetic networks;
- configuration assessment, i.e. scenario simulation and optimisation of the main scanning settings (i.e. location, resolution, and precision);
- validation of the accuracy of the algorithm (closed-loop simulation), i.e. the resulting material parameters and their standard deviations are compared to the ground truth values used within the simulation stage.

A conceptually similar tool has been developed for the optimal location of the scanner by Soudarissanane (2016), who developed a greedy algorithm that returns a minimal number of stand points of the sensor, given a 2D scene and some constraints on the admissible ranges of incidence angle and distance. Herein, the simulations

have been conducted, instead of real measurements, in order to (i) better control the boundary conditions and the noise levels of the observations, (ii) have nearly arbitrary flexibility regarding the object shape and material properties, and (iii) set the ground truth with a quasi-arbitrary level of precision for assessing the accuracy of the results.

The synthetic scan generation needs the following data as input:

- a FE model of a structure and its location;
- a loading scenario of the structure;
- the scanner location and orientation;
- the scanning settings of the scanner, i.e. its resolution and accuracy.

From the operative point of view, the ground truth displacements between the reference and the deformed states are simulated directly while creating an Abaqus .inp input file. Subsequently, two .obj geometry files that describe the shape of both the reference and the deformed states of the structure are exported and used as input for the synthetic scans. The boundary conditions (BC), although they can be chosen freely, have been designed to be realistic and as simple as possible in order to be able to validate the FE results with explicit analytical expressions, when possible. The only important aspect is that the BC of the scanned model coincide with the ones used within the solving FE model.

The levels of normally distributed noise that are applied to the simulated measurements can be defined freely. However, due to the finite internal precision of the specific adopted implementation of the algorithm and the piecewise linear deformed shape of the deformed FE mesh, the generation of synthetic scans introduces additional numerical errors that attain the size of 0.02 mm. On one hand, this is practically irrelevant because all market available scanners have significantly higher noise levels (see tab. 2.1); on the other hand, this is theoretically relevant, because the simulations cannot be used to investigate the achievable accuracies with lower noise levels e.g. if new measurement technologies become available. The simulation scenarios have been pragmatically restricted to noise levels σ_ρ above 0.1 mm (see fig. 3.23). In this way, the impact of the numerical errors does not exceed 20%.

The scanning random deviations have been modelled by simulating the measurement process of a TLS, and adding random deviations on all the three recorded observables, i.e. the range ρ , the horizontal angle φ , and the vertical angle θ . The noise realisation is random for every simulated scenario, in order to approximate reality and reduce the generation of biases due to a specific random realisation. An explanatory bi-dimensional sketch is presented in fig. 4.1. In the actual 3D case, both the vertical and the horizontal angles are considered. The scans are synthetically generated by intersecting the rays emitted from the centre of the instrument with the FE mesh, the nodes of which are exported from Abaqus CAE as .obj format files and then triangulated. The calculation of the coordinates of the point where each ray intersects the triangulation of the FE nodes has been performed following the ap-

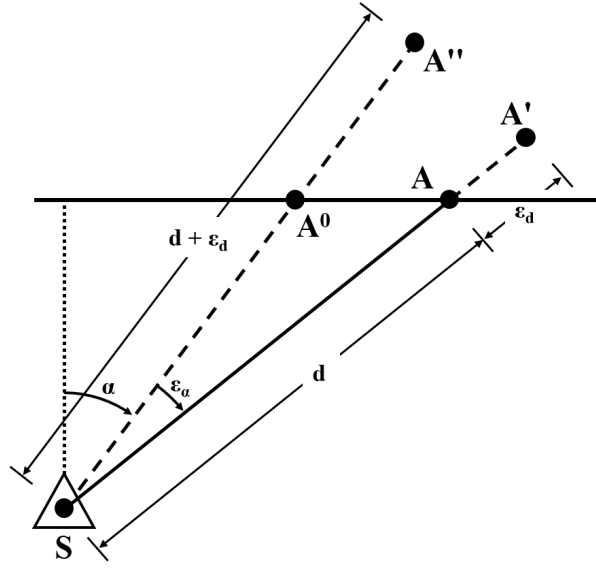


Figure 4.1: Generation of synthetic scans, including the effects of random deviations on angles and distances (2D situation for better readability). The scanner with instrumental centre S sends a signal in the direction $\alpha + \varepsilon_\alpha$ and records the direction α . The actual beam intersects the surface in the point A , and the measured distance is $d + \varepsilon_d$. As a result, the stored polar coordinates $(d + \varepsilon_d, \alpha)$ represent the point A'' , whereas an error-free scanning system ($\varepsilon_\alpha = \varepsilon_d = 0$) would have measured the point A^0

proach developed by Möller and Trumbore (1997) and implemented by Tuszynski (2019).

Additionally, in the validation tests, $\Sigma_{\hat{E}\hat{E}}$ has been calculated by multiplying the cofactor matrix for the a-priori variance factor σ_0 , instead of the a-posteriori one s_0 . In this way, $\Sigma_{\hat{E}\hat{E}}$ is not influenced by the incidental distribution of the residuals. However, since the noise is generated accordingly to $\Sigma_{dd,meas}$, the ratio between the posterior and the prior variance factors lies in the interval $[0.99 - 1.01]$, i.e. very close to the unity.

4.2. Simulated simply supported beam

The first of the two application cases with synthetic data consist in the analysis of a simply supported beam. The results shown in this chapter extend and detail the ones described in (Serantoni and Wieser, 2019). More precisely, the model consists of a 2 m long, flat beam of S235 steel, with a cross section 150 mm wide and 25 mm high. S235 steel is a very common type of structural steel; its properties are listed in tab. 4.1. The bar is subject to a three-point flexural test without torsion, and the vertical load at mid-span (4 kN, marked as \mathbf{F} in fig. 4.2) has been distributed over the whole cross section, in order to minimise local deformation effects and to approximate the ideal case of a simply-supported slender beam. The self-weight of

the bar is taken into account. In this way, the structural scheme is a very simple one, and the FE results could be validated by hand calculations.

In fact, the general shape of the Euler-Bernoulli bent beam is the following:

$$u(x) = - \int_0^x \left(\int_0^x \frac{M(x)}{E(x)J(x)} dx + C_1 \right) dx + C_2 \quad (4.1)$$

where M is the bending moment, J is the cross-sectional modulus of inertia, E is the Young modulus of the cross-section, x is the curvilinear coordinate along the beam, and C_1 and C_2 are integration constants that depend on the boundary conditions, i.e. the kind of restraints at the beam ends and the applied load. In the case of a simply supported beam $u(0) = u(l) = 0$ and, for a beam of length l , with uniform cross-section, and with a concentrated load ad midspan F and a distributed load q holds:

$$u(l/2) = \frac{Fl^3}{48EJ} + \frac{5ql^4}{384EJ} \quad (4.2)$$

The simulated scans have a resolution in both azimuth and elevation angle of 1 gon and cover the extrados of the beam, i.e. the bottom surface, where the longitudinal fibres experience traction. Although actual scanners can scan at resolutions much finer than 1 gon (see tab. 2.1), this value has been chosen because it is sufficient to denote the measurement as areal, yet keeping the computational effort of the scan generation low. Additionally, the choice of neglecting the correlations among the point of the point cloud (see 2.1.2) is particularly valid for scans with moderate resolution, because the laser footprints do not overlap. The scan data of the sides of the beam are not processed because there would be almost exclusively in-plane displacement of surface points, and the laser scan is not sensitive with respect to them. As for the standard deviations of the measurements, both the angular accuracies (see eqn. 3.10) have been set equal to 0.5 mgon. Instead, six levels of range accuracy σ_ρ have been simulated (0.1, 0.5, 1, 2, 5, and 10 mm). For this analysis, the coordinate system has been defined such that the centre of the beam extrados lies in the point (0, 0, 2.5), the y -axis is parallel to the long edge of the beam, and the xy -plane is parallel to the bottom and top surface of the beam (see fig. 4.2).

In order to constrain the horizontal rigid motion of the beam and preserve its symmetric deformation, the boundary conditions ($x=0$, $y=0$) have been applied to the nodes located at midspan only.

In sight of potential future laboratory experiments, a test about the suitability of the chosen finite elements have been conducted as well. Nevertheless, the choice of the FE elements has no impact on the results of closed-loop experiments, as long as the same type of element is used in both the stages of generation of the point cloud and of identification of the parameters. Given a mesh made of elements with the size of $10 \times 10 \times 2.5 \text{ mm}^3$, the vertical deflection at mid-span has been calculated for three

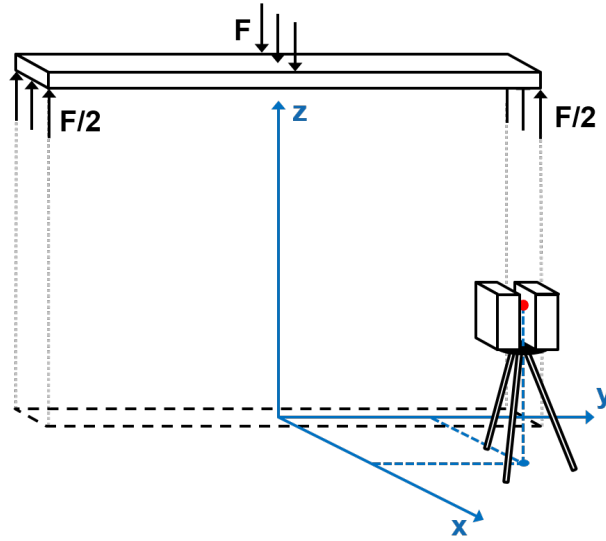


Figure 4.2: Sketch of the experimental setup, including the system of coordinates (in blue) and the sensor location (in red). The sketch is not drawn to scale

element types (C3D8, C3D8I, and C3D8R; see section 2.2) and compared with the analytical solution for a slender beam according to the Euler-Bernoulli theory (see eqn. 4.2). The results are summarised in tab. 4.2. The element that provides the results most in agreement with the analytical deflection at midspan is C3D8R, and it has therefore been chosen for conducting the simulation.

solution	analytical	FEM		
		C3D8	C3D8I	C3D8R
$u(l/2)$ [cm]	-1.77	-1.65	-1.76	-1.77

Table 4.2: Choice of the finite elements: comparison of the deflection at midspan with the analytic solution

Figs. 4.3 and 4.4 show the deformed steel beam, as modelled in Abaqus, while fig. 4.3 shows the 3D deformed shape, colour coded according to its vertical displacements. The grid-like pattern on the beam represents the individual C3D8R finite elements. Both the field of deformations and the field of von Mises stresses are symmetric with respect to the midspan section. The displacement in y direction is approximately null for the whole beam, except for the Poisson effect (see fig. 4.4b). The nodes close to the cross section at midspan do not move neither in x nor in y direction because of the applied boundary conditions.

4.2.1. Results for a single sensor location

With the synthetic sensor placed in the location (0,0,0), the beam has been monitored by using point clouds acquired with six different ranging accuracies. An

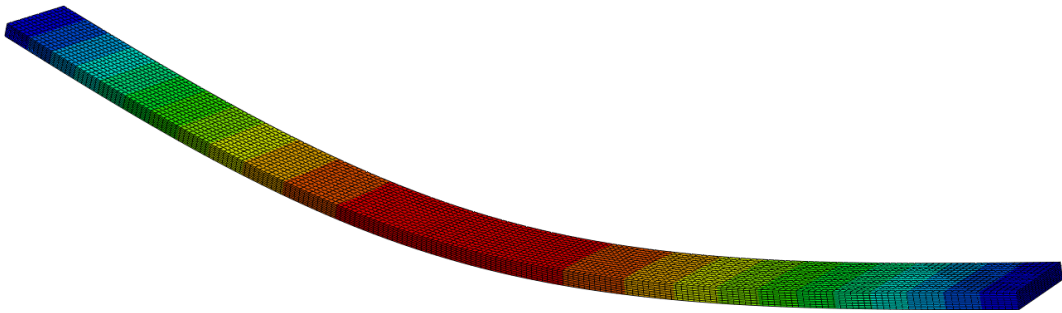


Figure 4.3: 3D deformed shape of the steel beam. The colour coding represents the vertical displacement u_z . The deformation is magnified 10x

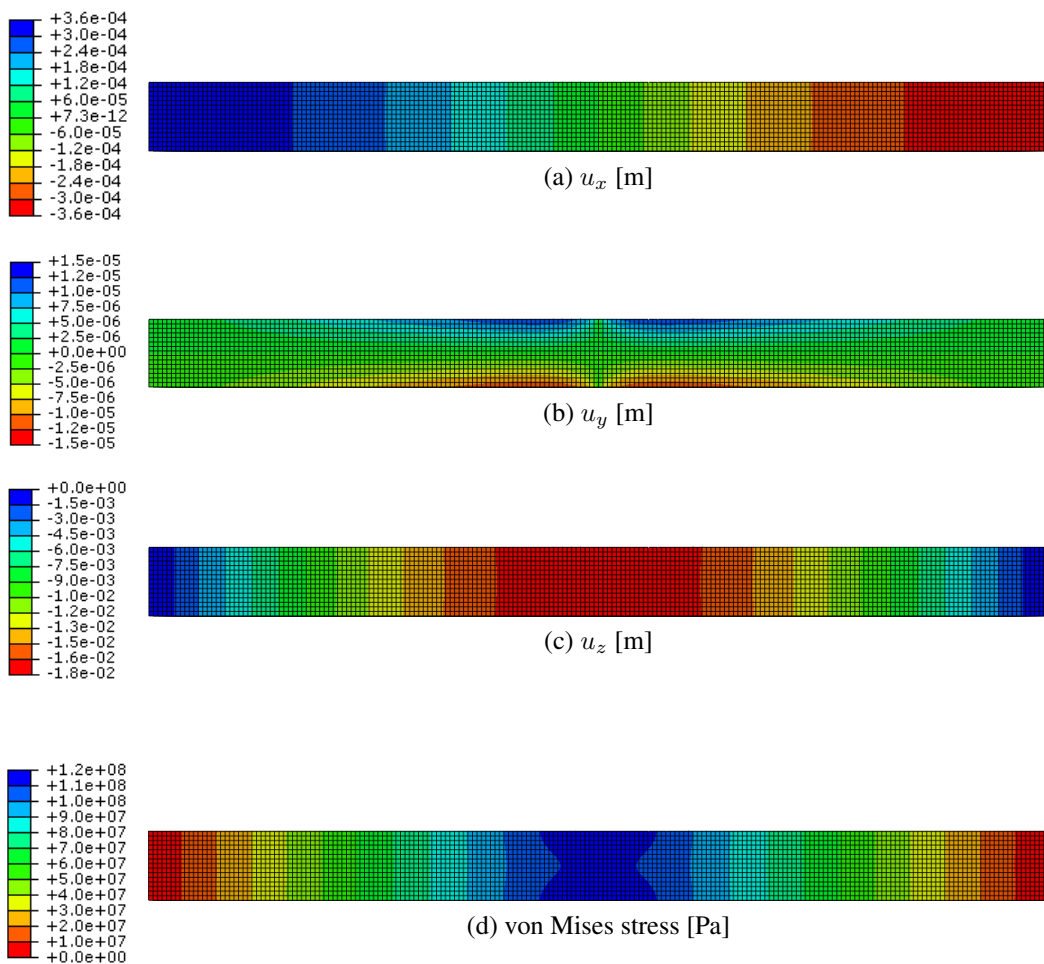


Figure 4.4: Steel beam: spatial distribution of displacements in the three directions and von Mises stresses

example of the results obtained for $\sigma_\rho = 1$ mm is shown in fig. 4.5. The results are presented in the same format as the outcome of the validation shown in fig. 3.16. The main difference is that for the results presented in this chapter the NN interpolation step (see section 3.3.3) is also included in the analysis. Therefore, the noise levels are not specified directly for the vertical displacement, but for the ranging accuracy of the sensor σ_ρ . Additionally, the position of the measurements reflects the scanning pattern instead of directly corresponding to the nodes of the FE model. Because of that, the pattern of \hat{E} along the beam is similar for different numbers of partitions (e.g. for $m = 8$ and $m = 12$).

Fig. 4.5 shows that the value of E_{true} lies within the 1σ error bars for all the estimated parameters, except for the scenario with only 1 partition, for which $\hat{E} - E_{\text{true}} = 1.56 \sigma_{\hat{E}}$. Moreover, similarly to fig. 3.16, an increase of the number of partitions provokes an increase in $\sigma_{\hat{E}}$, the pattern of which is symmetric along the x axis. This last two remarks are corroborated by figs. 4.6 and 4.7, respectively. More precisely, for a realistic value of $\sigma_\rho = 1$ mm, the ratio $\sigma_{\hat{E}}/E_{\text{true}}$ amounts to 0.5% for one partition, to 3.4% for two partitions, and to 1.7% for the central partition of three. These values coincides with the one shown by fig. 3.16, because for this particular scanning setup the uncertainty on the nodal displacements almost coincide by the uncertainty on the range measurements.

Fig. 4.7 shows the estimation of $\sigma_{\hat{E}}$ (i.e. the length of the error bars in fig. 4.5) for different levels of noise σ_ρ . As expected, the highest accuracy is obtained at mid-span for all the scenarios. Moreover, the minimum number of partitions sufficient to have no improvement in the estimation of \hat{E} (i.e. $\sigma_{\hat{E}} \approx \sigma_{E_0}$) for at least one partition decreases for a growing σ_ρ .

The dependence of $\bar{\sigma}_{\hat{E}}$ on σ_ρ is shown in fig. 4.6. For each simulated scenario, $\bar{\sigma}_{\hat{E}}$ is the average of all the $\sigma_{\hat{E}}$ across all the partitions. Predictably, all the relationships are monotonically increasing and do not intersect, except for the scenario with 2 partitions, on the basis of its symmetric structure (see also section 3.4.4). As also shown in fig. 4.5, the case of only one partition delivers much more accurate results than the case of multiple partitions.

The correlations among different parameters have been investigated as well. Fig. 4.8 shows the correlation matrices for six scenarios (the combinations of three number of partitions and two σ_ρ). Each entry of the correlation matrix has been calculated from the VCM of the estimated parameters as follows:

$$\text{corr}(\hat{E}_i, \hat{E}_j) = \frac{\sigma_{\hat{E}_i \hat{E}_j}}{\sqrt{\sigma_{\hat{E}_i}^2 \sigma_{\hat{E}_j}^2}} \quad (4.3)$$

It is possible to observe that all the off-diagonal values are negative. This is a plausible result because, if a partition has an overestimated value of E associated, the other partitions should exhibit an underestimated value in order to compensate and follow the general shape of the deformation, and vice-versa. More precisely, the lower values close to the main diagonal imply that the anti-correlation is larger

for the partitions that are close each other, while the large values in the centre of the matrix hint again that the partitions that influence the global behaviour of the beam the most are the ones close to midspan. Lastly, the absolute values of the correlations decrease for an increasing number of partitions. The intuitive reason is that a parameter change for a small partition influences the rest of the structure less than a large one.

The fig. 4.9 explicitly shows the 2D scatter of the measurements and the elastic curve of the nodes of the beam, for different levels of ranging noise σ_ρ . In this figure, the signal-to-noise ratio of the measurement can be immediately observed. It is also possible to observe that the point density decreases by moving from the centre of the beam towards one of the supports, because of the relative position of the scanner with respect to the bent beam. For the scenarios with $\sigma_\rho \leq 5$ mm, the underestimation of the stiffness of the beam is quite moderate, despite the signal-to-noise ratio is remarkably low.

4.2.2. Results for multiple sensor locations

Besides the analysis on different range accuracies and number of partitions, also the effects of a change of sensor location have been examined. In practice, the estimation of E has been repeated for 36 standpoints in the vicinity of the simulated beam. σ_ρ has been kept constant (2 mm) for all the simulated standpoints. Correspondingly to the simulations detailed in chapter 3, $E_0 = E_{\text{true}} = 210$ GPa.

The output of this analysis are the two heatmaps depicted in figs. 4.10 and 4.11, which represent the spatial distribution of \hat{E} , and $\sigma_{\hat{E}}$, respectively. The values have been estimated in correspondence of the standpoints, while the colour coding has been bi-linearly interpolated among them for visualisation purposes. The standpoints are arranged on a non-regular 6×6 grid, the spacing of which is in both dimensions [0, 0.125, 0.125, 0.25, 0.5, 1] m. Since the beam and the applied forces have two perpendicular axes of symmetry parallel to the xy plane, only the sensor standpoints belonging to the a single quadrant have been considered.

The most evident result is that both the accuracy and the precision of the identification degrade for standpoints far from the beam. No clear bias pattern is recognisable, as the \hat{E} estimated with standpoints far from the beam show large instability but no clear bias.

Moreover, the standpoints aligned with the longitudinal axis of the beam are the ones delivering the most unstable results. Indeed, for these points, a small change of configuration can cause a large change in the amount of scanned points on the bottom surface of the beam. In fact, at a large distance, apart from the problems caused by an unfavourable angle of incidence, only few rows of scanned points might actually illuminate the surface of the structure. This effect would be less problematic if the angular increment of the scan were smaller, so that the amount of scanned points on the surface is less influenced by the scanner configuration.

Although these results contemplate only one realisation of the simulated point

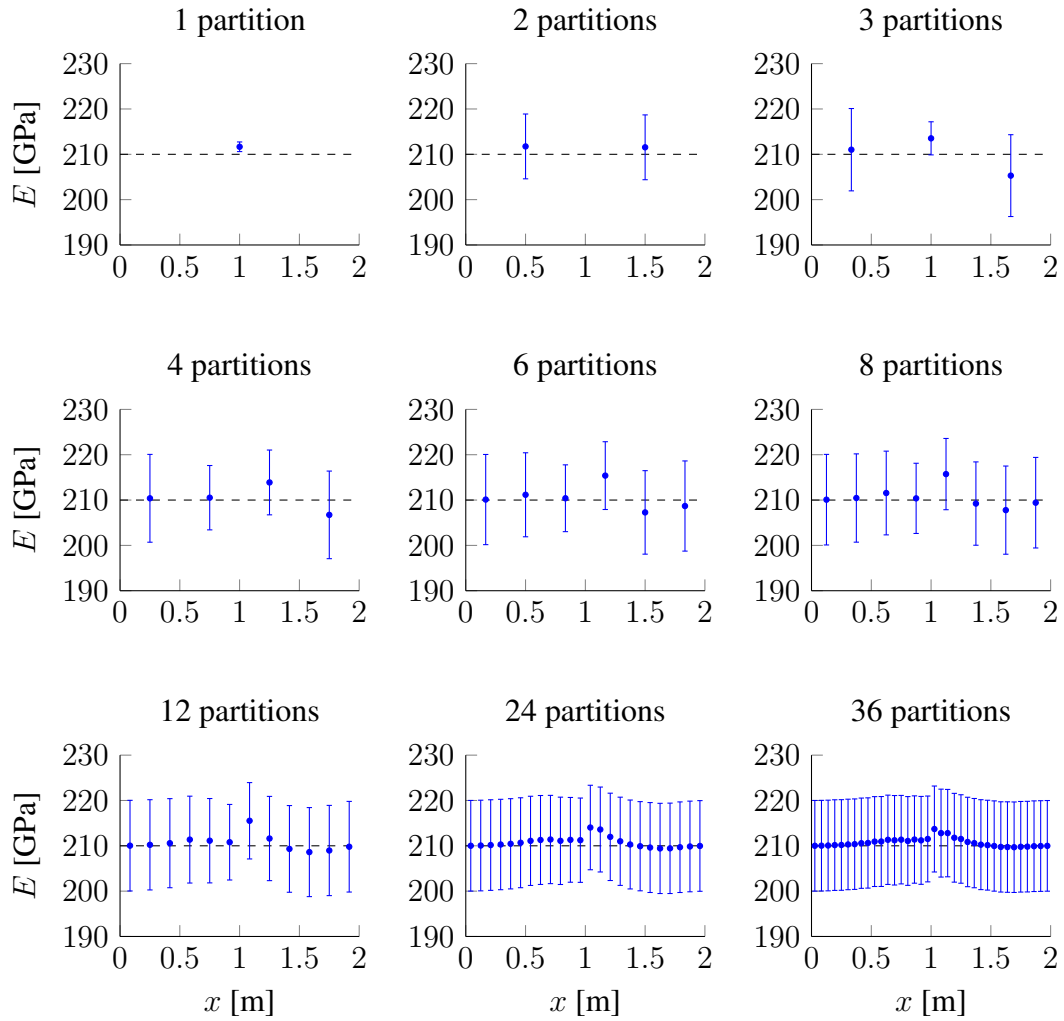


Figure 4.5: Result of a full simulation with $\sigma_\rho = 1$ mm, and $E_0 = 210 \pm 10$ GPa. The horizontal axes show the position along the 2 m long beam, while the vertical axes represent the estimated Young modulus of each partition, in GPa. The vertical error bars depict the 1σ confidence interval for each partition. The dashed black line represents the value of the ground truth $E_{\text{true}} = 210$ GPa.

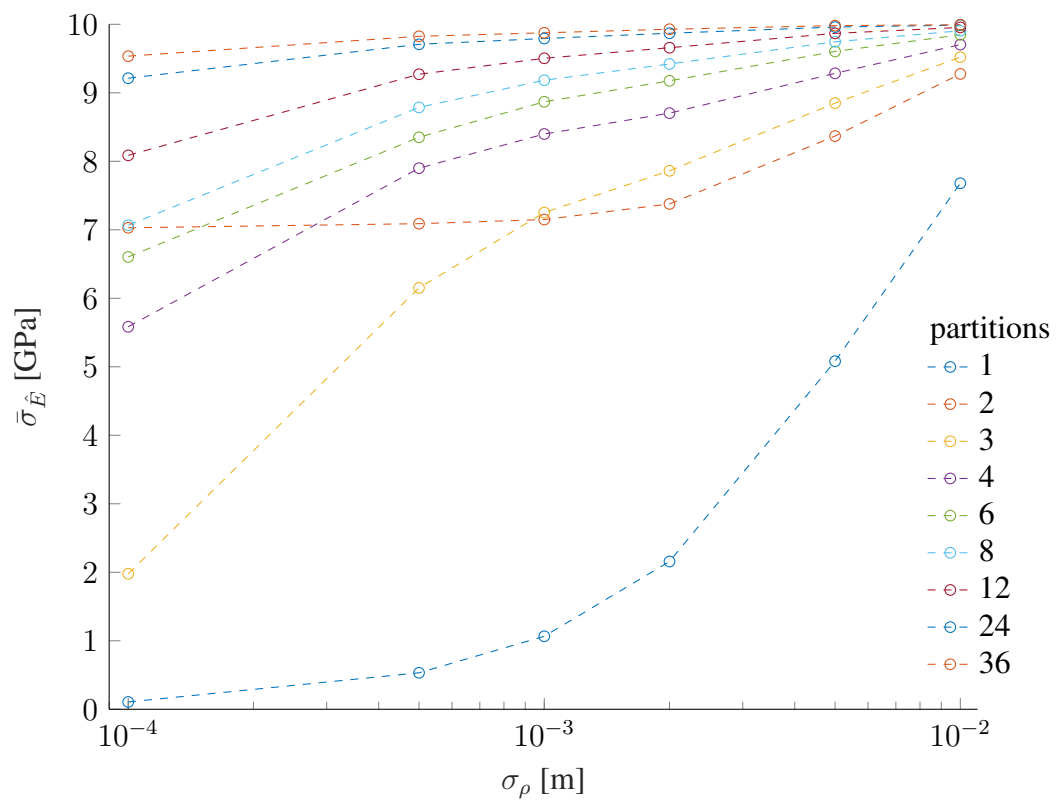


Figure 4.6: $\bar{\sigma}_{E_i}$ for various number of partitions and various noise levels σ_{ρ} , $E_0 = E_{\text{true}} = 210$ GPa

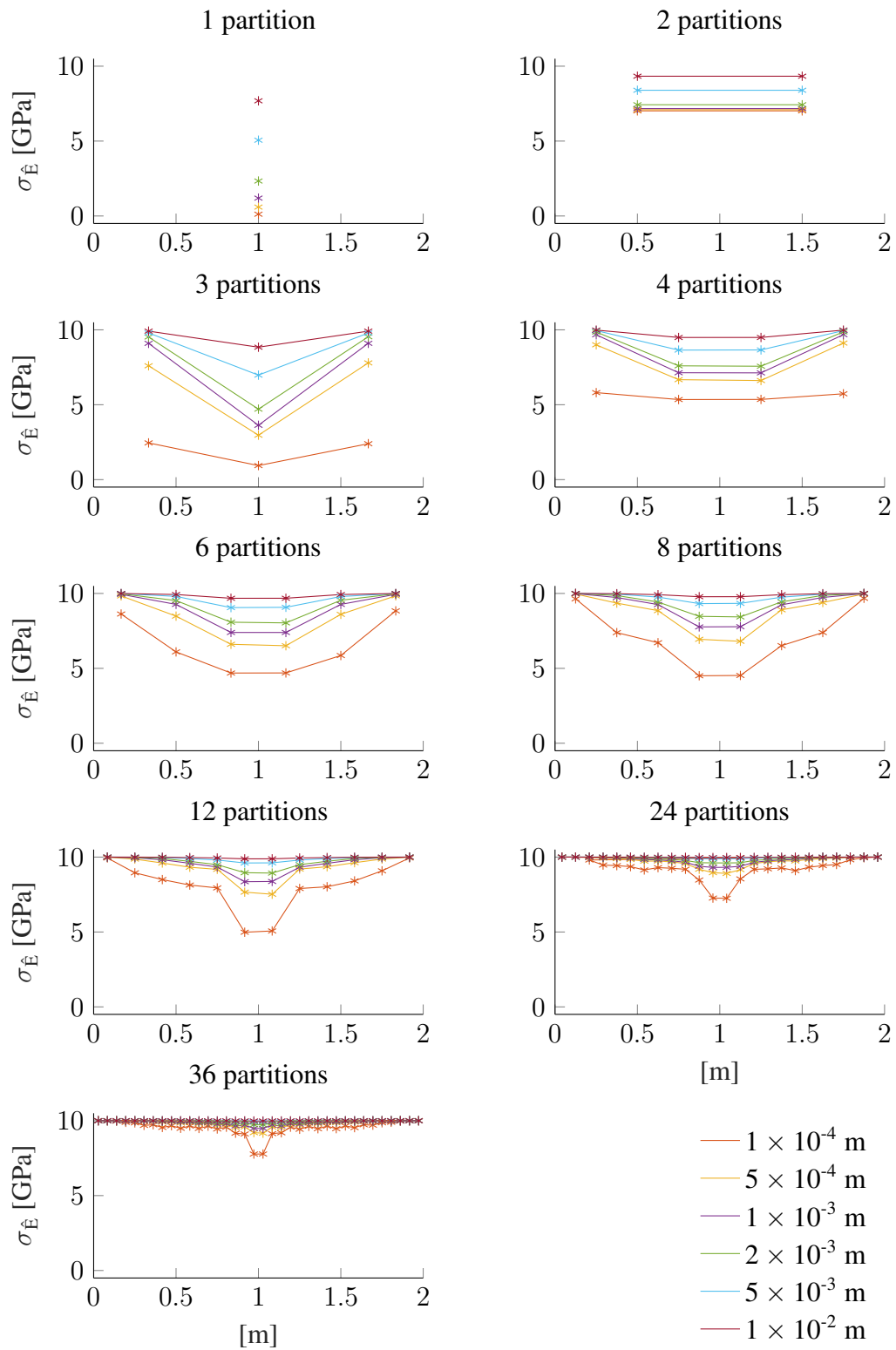


Figure 4.7: σ_{E_i} for various number of partitions and various noise levels σ_{ρ} from 10^{-6} to 10^{-2} m, $E_0 = E_{\text{true}} = 210$ GPa

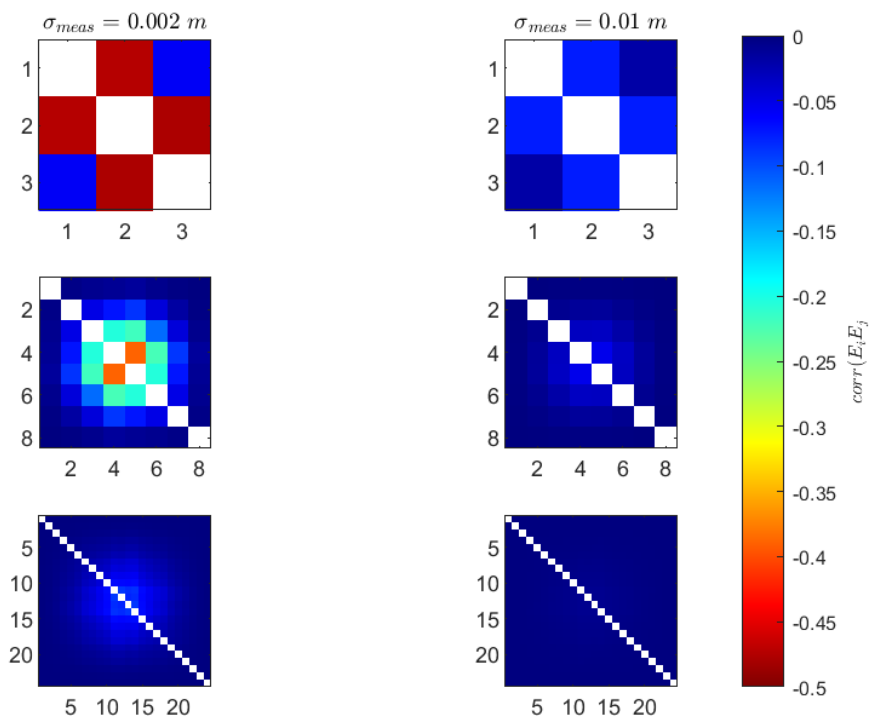


Figure 4.8: Correlation matrices for 3, 8, and 24 partitions and two noise levels σ_ρ . $E_0 = E_{true} = 210$ GPa

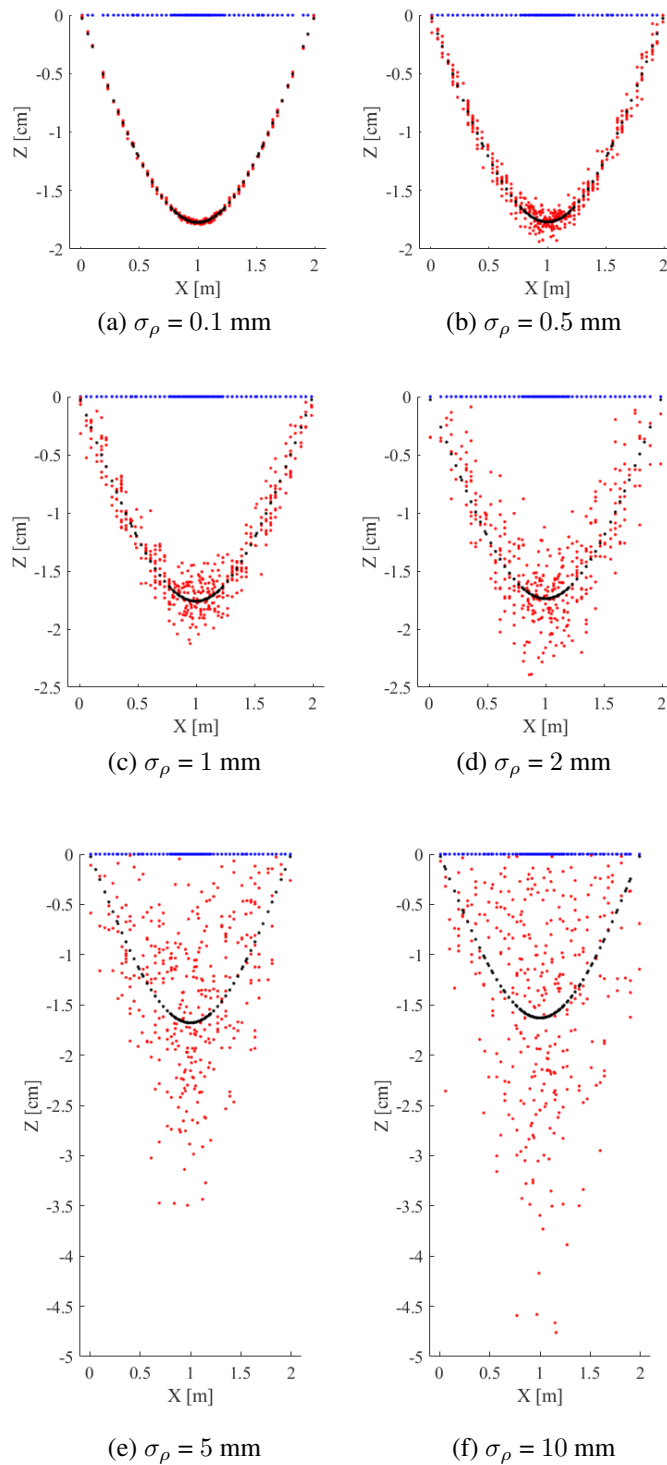


Figure 4.9: 2D view of the measured displacements (in red), the simulated displacements (in black), and the FE nodes in the undeformed configuration (in blue). Results for the scenarios with 1 partition. The scale is adjusted to account for the various values of σ_ρ

cloud, it is possible to draw some indications about the position of the suitable standpoints for a given accuracy in estimating \hat{E} . For this application scenario, the figs. 4.10 and 4.11 suggest that the standpoints within the region ($x > 0.5$ m, $y > 1$ m) deliver an estimation of \hat{E} that deviates from the E_{true} below 7%, while standpoints within the region ($x > 0.125$ m, $y > 0.125$ m) deliver results with a deviation from the E_{true} below 1.5%. The maximal $\sigma_{\hat{E}}$ for the two mentioned regions amount to 7% and 1%, respectively. In addition, given the large sensitivity to the random deviations of the standpoint locations, a Monte Carlo simulation to evaluate the heatmap of $\sigma_{\hat{E}}$ would be also beneficial.

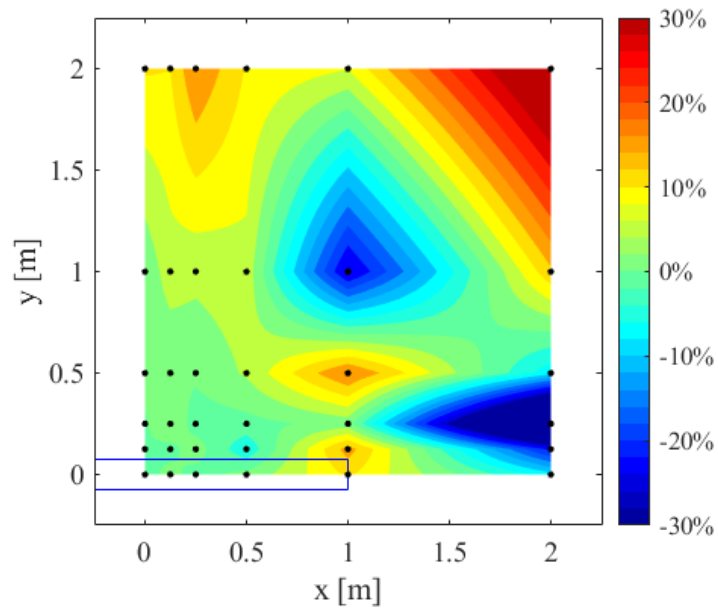


Figure 4.10: Deviation of the estimated value \hat{E} as percent ratio of the ground truth E_{true} . The contour of the scanned beam is outlined in blue and the black dots represent the simulated standpoints, while the colour coding is interpolated between them

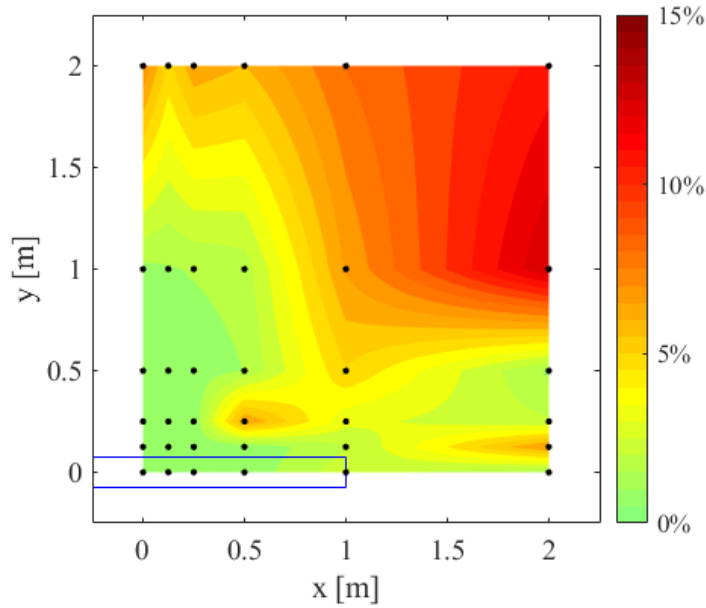


Figure 4.11: Estimated standard deviation of the Young modulus $\sigma_{\hat{E}}$. Values expressed as percent ratios to the ground truth E_{true} . The representation of the contour of the beam and of the standpoints is the same as in fig. 4.10

4.3. Simulated corner-supported plate

The second application case is very similar to the first one, presented in section 4.2. Instead of a simply supported beam, the investigated object is a corner-supported plate, which has a surface of $6 \times 6 \text{ m}^2$ and a thickness of 5 cm. Such specifications have been chosen in order to account also for a planar object, and not only for a linear one. The plate is synthetically scanned from a distance of 2.5 m, below the centre of the extrados. The chosen material is the aluminium alloy 5083, which is actually often manufactured in large plates, and it is commonly used for marine and chemical applications, because its chemical resistance, good strength, and suitability to be welded. Its proprieties are listed in tab. 4.1.

As for the FE modelling, C3D8R elements with a size of $150 \times 150 \times 5 \text{ mm}^3$ have been used, and the plate has been restrained as follows:

- the four corners have been restrained vertically ($u_z = 0$);
- one node of the plate has been restrained horizontally in both directions ($u_x = u_y = 0$);
- a second node of the plate as been restrained horizontally in one direction ($u_x = 0$).

In this way, besides the four vertical supports, only the minimum number of restraints (three) prevents the rigid body motion of the plate within the horizontal plane, and the deformation in the horizontal directions is symmetric. The 3D de-

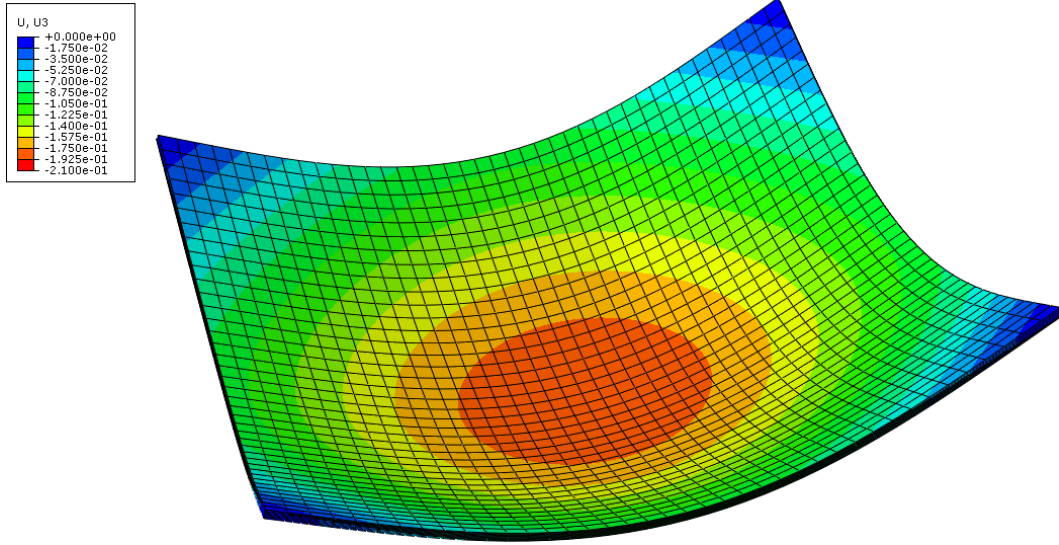


Figure 4.12: 3D deformed shape of the alloy plate. The colour coding represents the vertical displacement u_z . The deformation is magnified 10x

formed shape of the plate is depicted in fig. 4.12, while the displacements of the slab in the three directions and the field of the von Mises stress are shown in fig. 4.13.

4.3.1. Results

Because of the square shape of the plate, it has been subdivided in $1, 2 \times 2, 3 \times 3, 4 \times 4,$ and 5×5 partitions. The results of the identification of the Young's modulus are depicted in figs. 4.14 to 4.25.

Even if the analysis of the alloy plate is very similar to the one of the steel beam, the graphical representation of the results is quite different because of the 2D arrangement of the partitions. For each level of ranging accuracy σ_ρ , two figures are provided: the first one illustrates the distribution across the various partition of \hat{E} , while the second one shows their accuracies $\sigma_{\hat{E}}$. The values of the results are colour-coded.

Several remarks about these results coincide with what already observed in section 4.2.1:

- $\sigma_{\hat{E}}$ increases for growing values of σ_ρ ;
- the symmetry of the structure is reflected in the spatial distribution of both \hat{E} and $\sigma_{\hat{E}}$;
- the least sensitive regions of the plate are the one close to the supports;
- the ground truth E_{true} lies within $\hat{E} \pm 2\sigma_{\hat{E}}$ for all the cases with $\sigma_\rho \geq 0.5$ mm;
- the precision of the identification degrades of several orders of magnitude when increasing the number of the partitions.

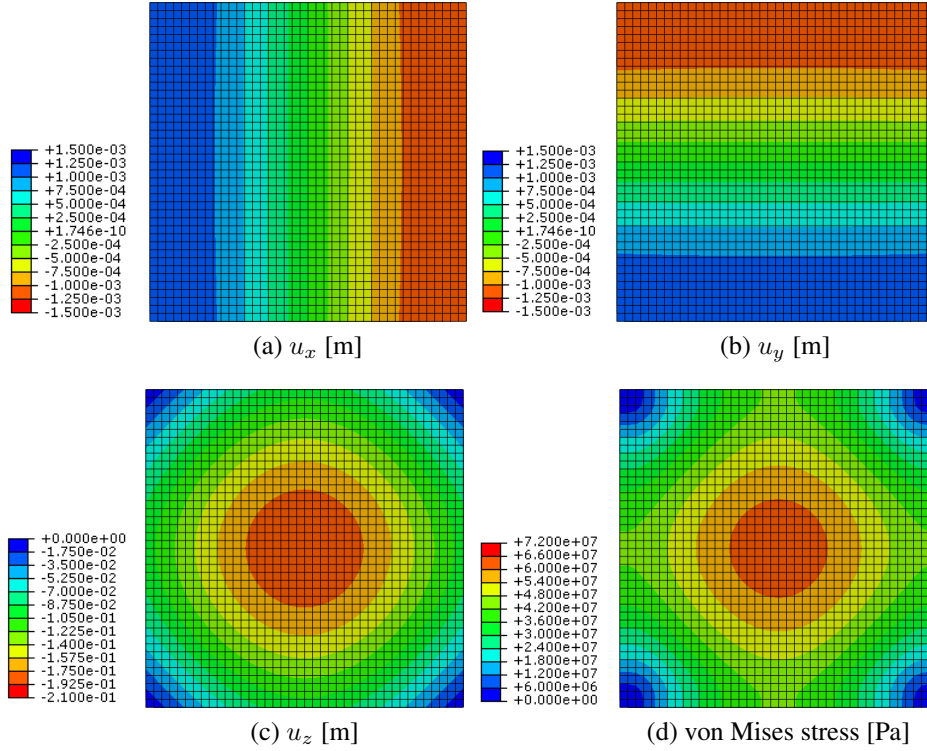


Figure 4.13: Alloy plate: spatial distribution of nodal displacements and von Mises stresses

Regarding the last remark, the uncertainty on \hat{E} for the case of 5×5 partitions is already very close to σ_{E_0} even for $\sigma_\rho = 0.1$ mm, which is a very low value compared to the accuracy of the most market available laser scanners (see tab. 2.1). Therefore, for this application example, it is quite difficult to perform a successful identification with a low level of granularity, i.e a large number of partitions. Anyway, the opposite side of this statement is very positive: a very high precision can be reached when using few partitions. In fact, for a value of $\sigma_\rho = 1$ mm, the ratio $\sigma_{\hat{E}}/E_{\text{true}}$ amounts to 0.03% for one partition, and to 0.71% for 2×2 partitions. For a value of $\sigma_\rho = 2$ mm instead, $\sigma_{\hat{E}}/E_{\text{true}}$ equals 0.06% for one partition, and 0.83% for 2×2 partitions.

Lastly, for a very low ranging noise ($\sigma_\rho = 0.1$ mm, see fig. 4.14) the values of \hat{E} are very scattered across the plate for 3×3 and 5×5 partitions, and the deviations from E_{true} abundantly exceed σ_{E_0} . The probable reason of such effect is that the geometric measurement have a much larger weight within the LSA, and the solution tends to "overfit" the measurement noise.

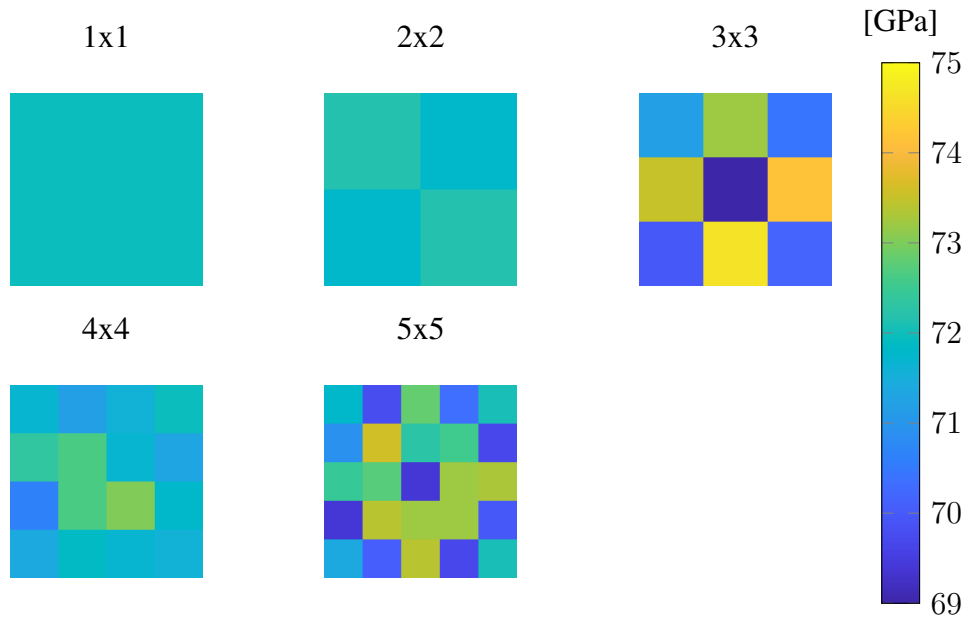


Figure 4.14: Alloy plate, \hat{E} for different numbers of partitions, $\sigma_\rho = 1 \times 10^{-4}$ m, $E_{\text{true}} = 72$ GPa

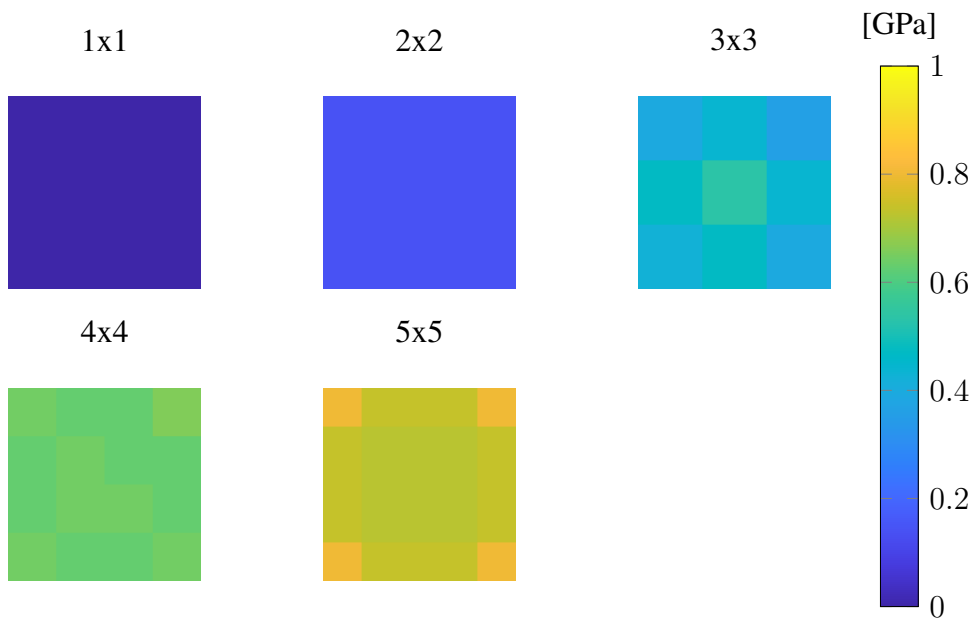


Figure 4.15: Alloy plate, $\sigma_{\hat{E}}$ for different numbers of partitions, $\sigma_\rho = 1 \times 10^{-4}$ m, $E_{\text{true}} = 72$ GPa

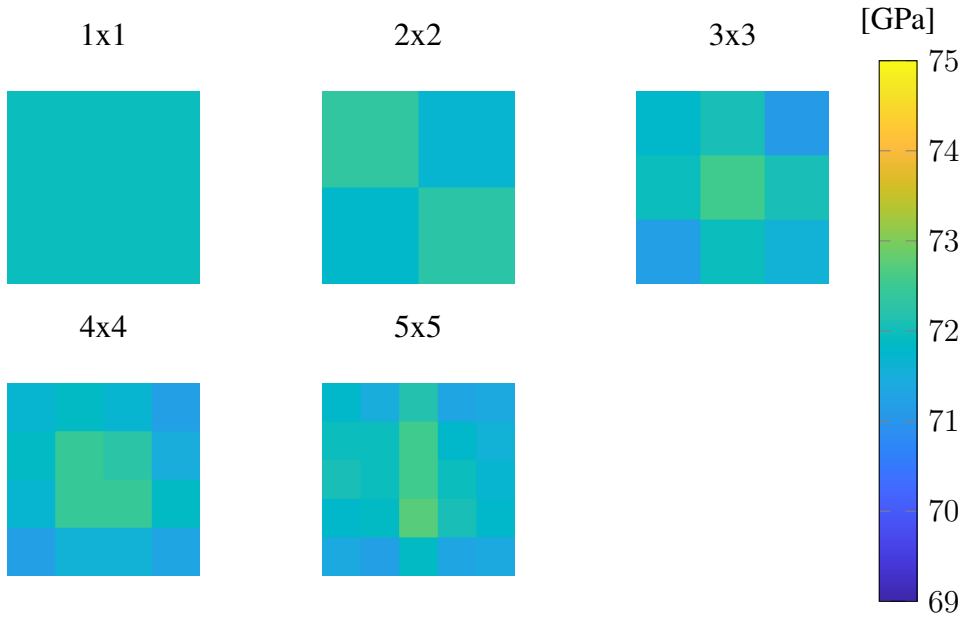


Figure 4.16: Alloy plate, \hat{E} for different numbers of partitions, $\sigma_\rho = 5 \times 10^{-4}$ m, $E_{\text{true}} = 72$ GPa

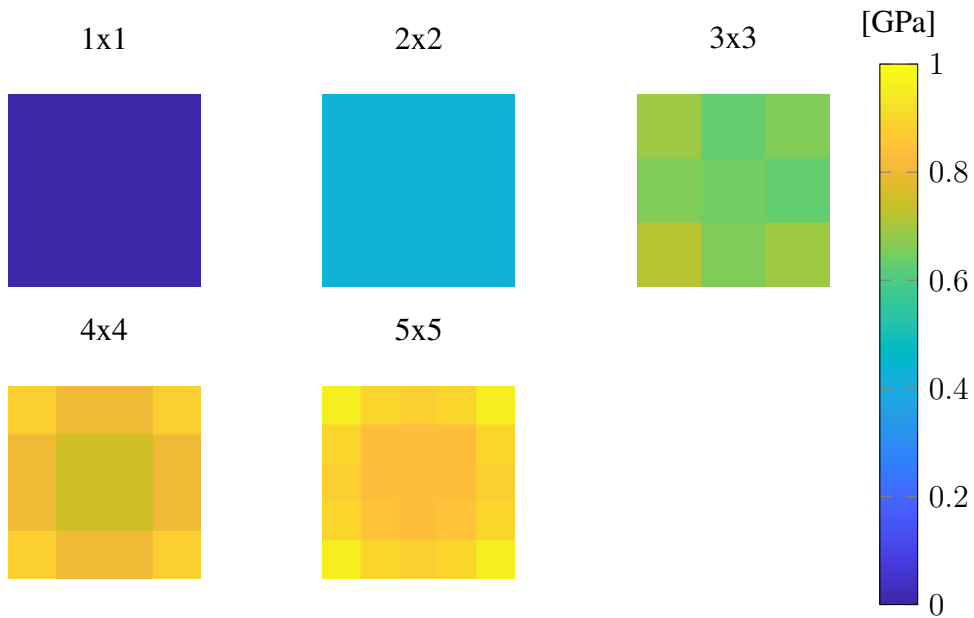


Figure 4.17: Alloy plate, $\hat{\sigma}$ for different numbers of partitions, $\sigma_\rho = 5 \times 10^{-4}$ m, $E_{\text{true}} = 72$ GPa

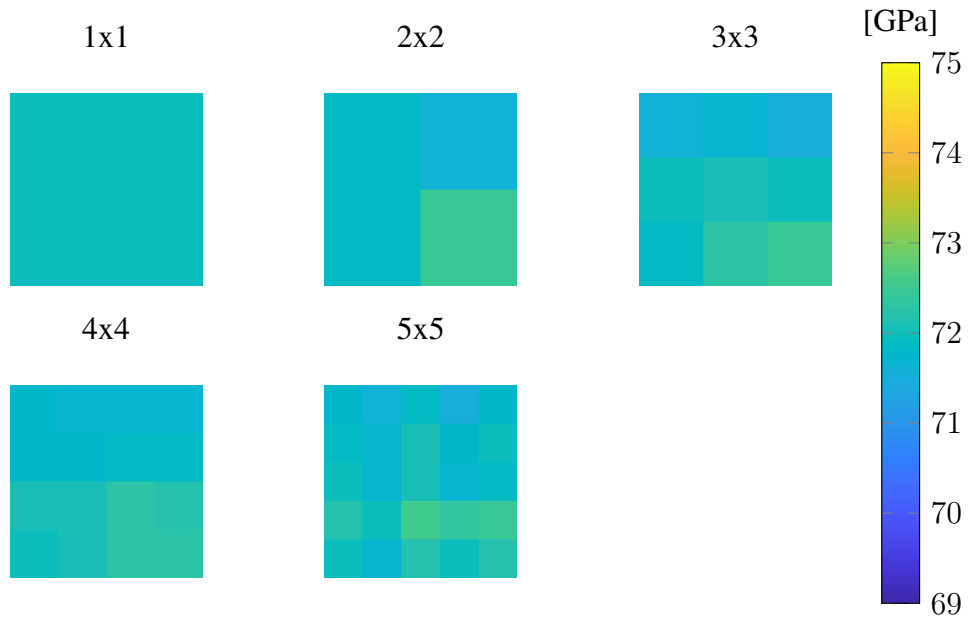


Figure 4.18: Alloy plate, \hat{E} for different numbers of partitions, $\sigma_\rho = 1 \times 10^{-3}$ m, $E_{\text{true}} = 72$ GPa

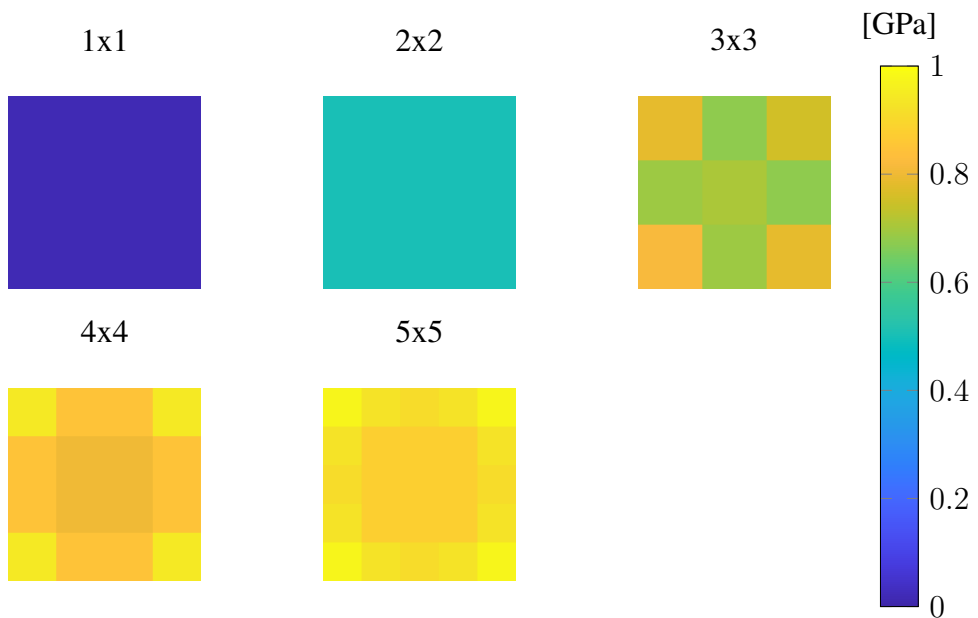


Figure 4.19: Alloy plate, $\sigma_{\hat{E}}$ for different numbers of partitions, $\sigma_\rho = 1 \times 10^{-3}$ m, $E_{\text{true}} = 72$ GPa

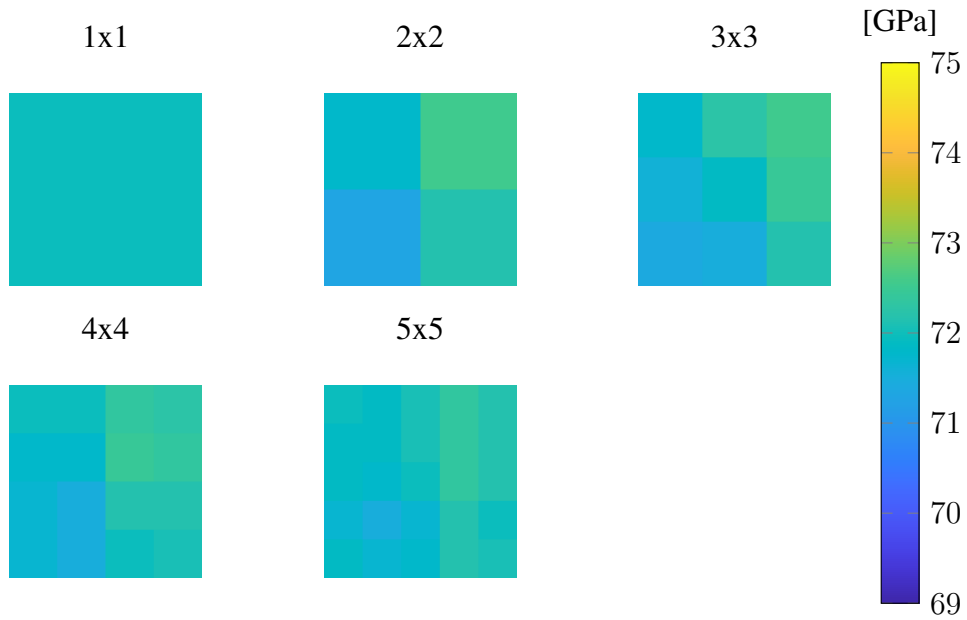


Figure 4.20: Alloy plate, \hat{E} for different numbers of partitions, $\sigma_\rho = 2 \times 10^{-3}$ m, $E_{\text{true}} = 72$ GPa

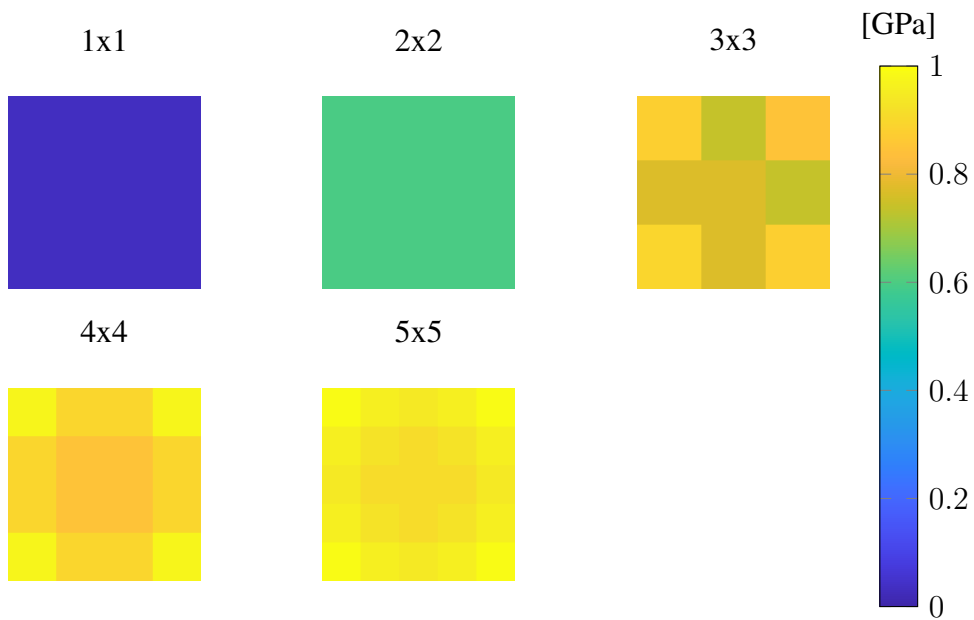


Figure 4.21: Alloy plate, $\sigma_{\hat{E}}$ for different numbers of partitions, $\sigma_\rho = 2 \times 10^{-3}$ m, $E_{\text{true}} = 72$ GPa

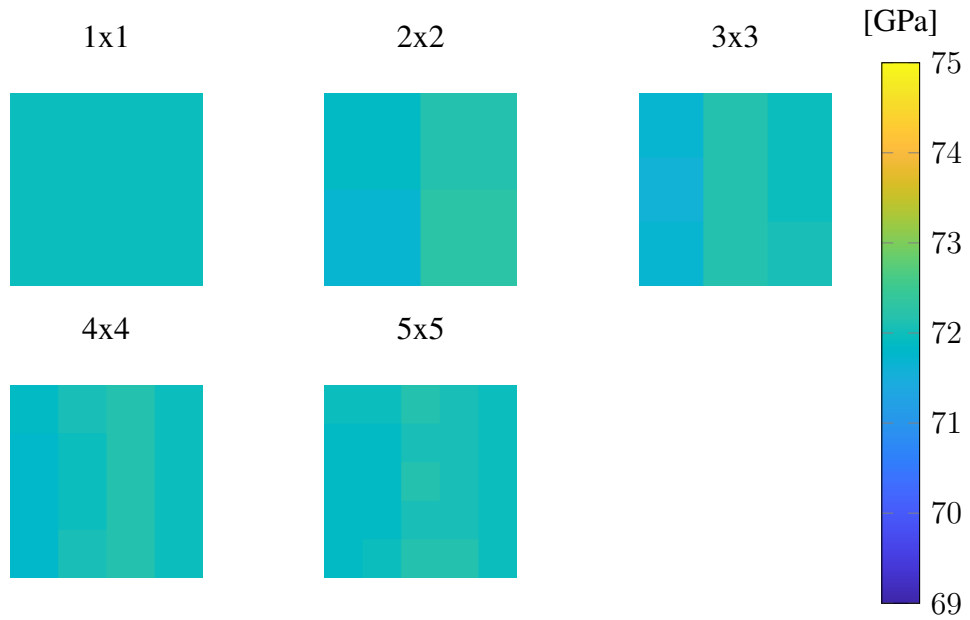


Figure 4.22: Alloy plate, \hat{E} for different numbers of partitions, $\sigma_\rho = 5 \times 10^{-3}$ m, $E_{\text{true}} = 72$ GPa

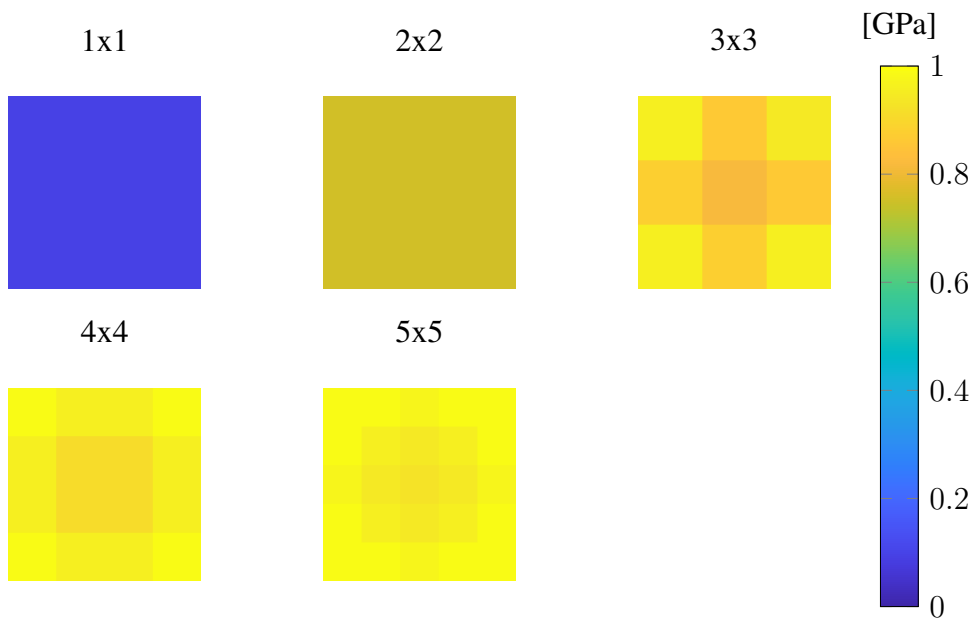


Figure 4.23: Alloy plate, $\sigma_{\hat{E}}$ for different numbers of partitions, $\sigma_\rho = 5 \times 10^{-3}$ m, $E_{\text{true}} = 72$ GPa

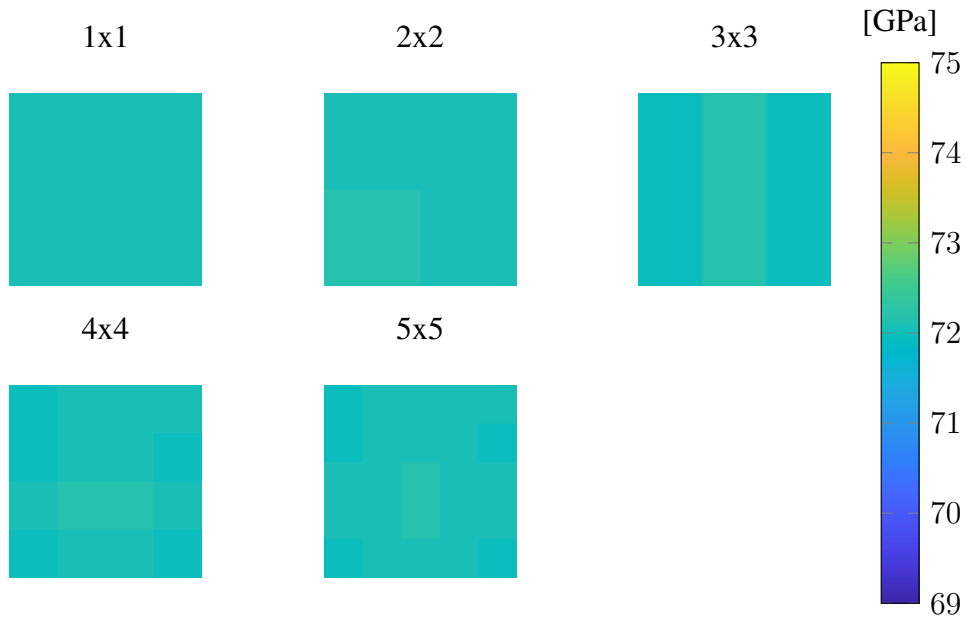


Figure 4.24: Alloy plate, \hat{E} for different numbers of partitions, $\sigma_\rho = 1 \times 10^{-2}$ m, $E_{\text{true}} = 72$ GPa

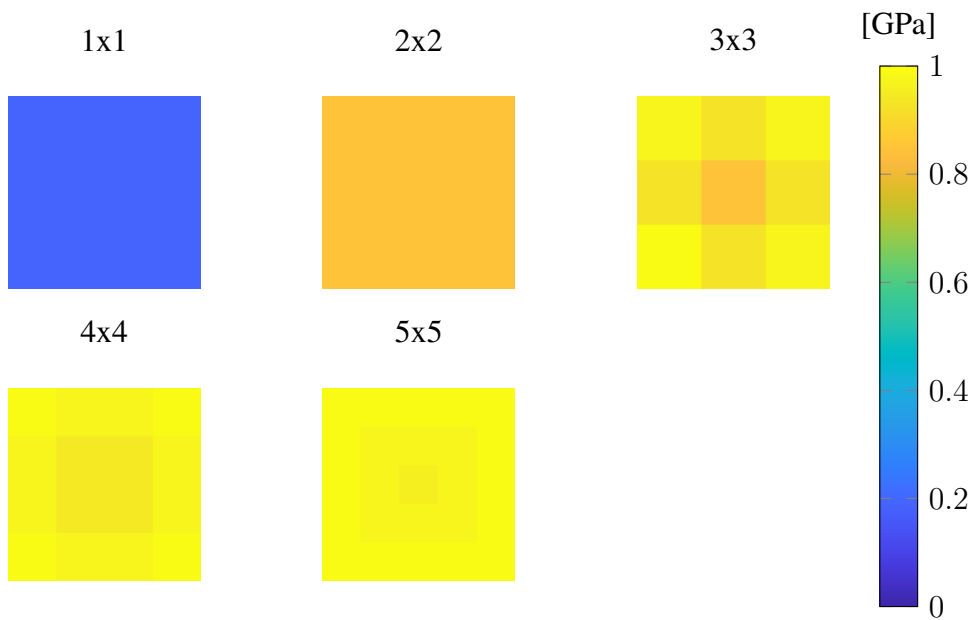


Figure 4.25: Alloy plate, $\hat{\sigma}$ for different numbers of partitions, $\sigma_\rho = 1 \times 10^{-2}$ m, $E_{\text{true}} = 72$ GPa

4.4. Cross-laminated timber slab

This section refers to the publication (Serantoni et al., 2018), in which the Young's and shear modulus of a corner-supported cross-laminated-timber slab have been estimated. The behaviour of this object has been analysed because this slab is the first real-scale, long-term test of an innovative glued connection allowing the bonding of timber slabs parallel to the timber's grain. The slab has been left outdoors for several months, thus undergoing cyclical temperature and humidity changes. More details about the project are provided by Zoellig et al. (2019). As fig. 4.26 illustrates, the monitored CLT slab is composed of four single square slabs glued together, supported by four wooden posts.

4.4.1. Modelling

The cross-laminated timber is a composite material made of several stacked solid wooden boards glued together. The boards are alternatively oriented in two directions, generally 0° and 90° , and their number is often odd. In fact, wood is an orthotropic material, i.e. its mechanical properties differ depending on the direction along which they are measured. CLT structural slabs are often employed in construction as wall and floor elements because they are able to withstand both in-plane and out-of-plane loads. The CLT is an example of engineered wood, and, compared to solid wood, it features more standardised mechanical properties; furthermore, single structural members made of CLT can be manufactured in a wider range of shapes. An overview on the CLT and its mechanical properties is provided by Schickhofer et al. (2016).

For this example application, the material properties have been defined following the standard DIN EN 384:2016, expressing the Young modulus parallel to the grain E_{90} as a function of the mean Young modulus parallel to the grain E_m . Similarly, the rolling shear modulus G_r is expressed as a function of shear modulus G . The values of the three Poisson ratios along the principal directions (see fig. 4.27) are taken from (Bodig and Jayne, 1982). Therefore, the material properties have been defined as shown in tab. 4.3, and the symmetric compliance tensor \mathbf{C} (i.e. the inverse of the stiffness tensor) of the orthotropic material depends only on E and it assumes the following form:

$$\mathbf{C} = \begin{bmatrix} \frac{1}{E} & \frac{-\nu_{RL}}{E/30} & \frac{-\nu_{TL}}{E/30} & 0 & 0 & 0 \\ \frac{-\nu_{LR}}{E/30} & \frac{1}{E/30} & \frac{-\nu_{TR}}{E/30} & 0 & 0 & 0 \\ \frac{-\nu_{LT}}{E/30} & \frac{-\nu_{RT}}{E/30} & \frac{1}{E/30} & 0 & 0 & 0 \\ 0 & 0 & 0 & \frac{1}{E/16} & 0 & 0 \\ 0 & 0 & 0 & 0 & \frac{1}{E/16} & 0 \\ 0 & 0 & 0 & 0 & 0 & \frac{1}{E/160} \end{bmatrix} \quad (4.4)$$

The wood of the analysed CLT is made of spruce, and belongs to the strength class

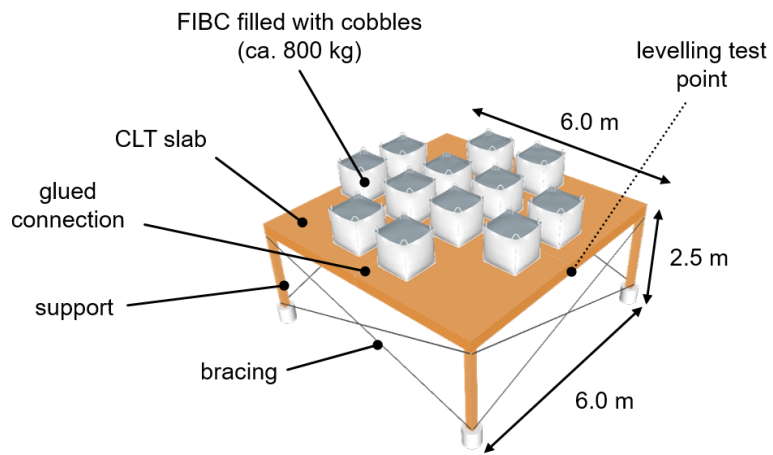


Figure 4.26: Representation of the CLT slab, including the supports and the FIBC. Image courtesy of Marcel Muster

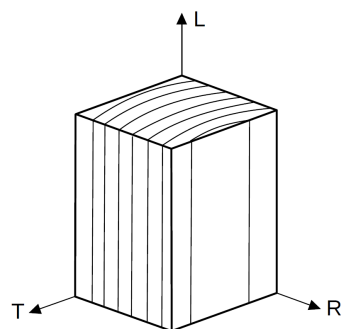


Figure 4.27: Definition of the principal directions of timber: longitudinal (L), transverse (T) and radial (R). Modified from (Fahrni, 2016)

E_0	E_{90}	G	G_r	ν_{LR}	ν_{LT}	ν_{RT}
E_m	$\frac{E_m}{30}$	$\frac{E_m}{16}$	$\frac{G}{10}$	0.37	0.42	0.47

Table 4.3: Timber stiffness relations and values of the Poisson’s ratios. The first index indicates the direction of application of the force, while the second one indicates the direction of the reaction

C24, which denotes a characteristic flexural strength of 24 MPa. Therefore, according to the standards DIN EN 384:2016, its nominal value of E_m is $11\,000 \pm 2249$ MPa. The density of the CLT amounts to 436 kg/m^3 .

4.4.2. Measurements

The slab has been monitored in three epochs: some hours after the construction, with the slab still supported in several locations by shoring props (epoch 0); 20 hours later (epoch 1); and 44 hours later (epoch 2), after the application of 12 flexible intermediate bulk containers (FIBC) filled with cobbles. Thus, between the epochs 0 and 1 the structure was expected to deform because of its own weight only, while the deformations between the epochs 1 and 2 is due to the applied live load. The point cloud has been acquired with a *Faro Focus3D X330* scanner, the specifications of which are listed in tab. 2.1.

The slab’s extrados was scanned from below (see fig. 4.28a). At epoch 0, a single scan was performed. Since some occlusions were noticed while visualising the point cloud of epoch 0, at epochs 1 and 2 the scans were taken from four standpoints. The four scans were registered with the software package *Faro Scene*, with the aid of chequerboard targets mounted at the base of the vertical supports of the slab as stable references within each epoch (see fig. 4.28b).

The supports have likely shortened because of the applied loads, and the measured deformations were corrected for this effect by subtracting the bi-linear form fitting the vertical displacement observed at the four corners. In fact, the rigid motion of the slab is not relevant for the purposes of this analysis, only the slab deformations are. An example of measured displacement field after the correction for the sinking supports is provided in fig. 4.29b.

Moreover, the vertical displacements obtained with the laser scans have been successfully validated against a sample of 19 bolts, the vertical displacement of which has been measured with classical geometric levelling. The comparison of the measured displacements of one example bolt located at mid-span along an edge of the CLT slab is plotted in fig. 4.29a.

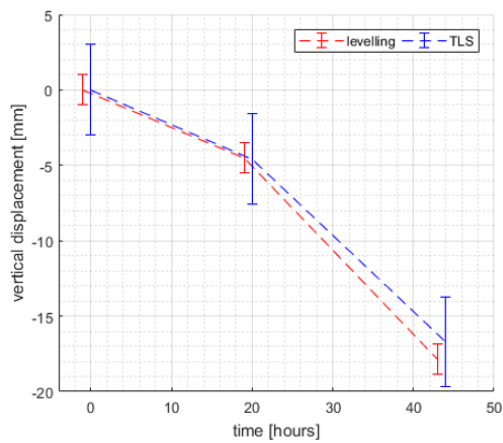


(a) Laser scanner beneath the extrados of the slab

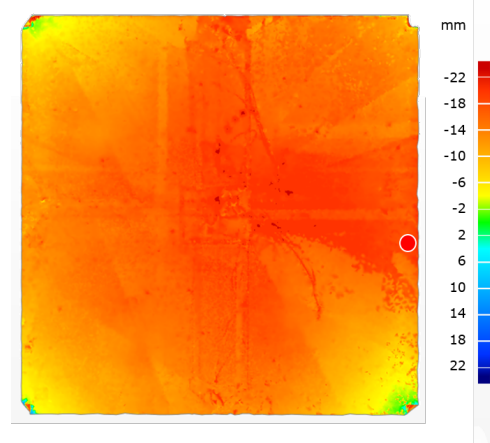


(b) Flat chequer-board target

Figure 4.28: Photos of the TLS monitoring of the CLT slab



(a) Validation of the TLS displacements with levelling, 1σ error bars



(b) Field of displacements between epochs 1 and 2

Figure 4.29: Comparison of the TLS and levelling monitoring of the CLT slab. The position of the levelling bolt, the displacements of which are shown in in sub-figure (a), is represented by a white circle in sub-figure (b) and indicated by an arrow in fig. 4.26

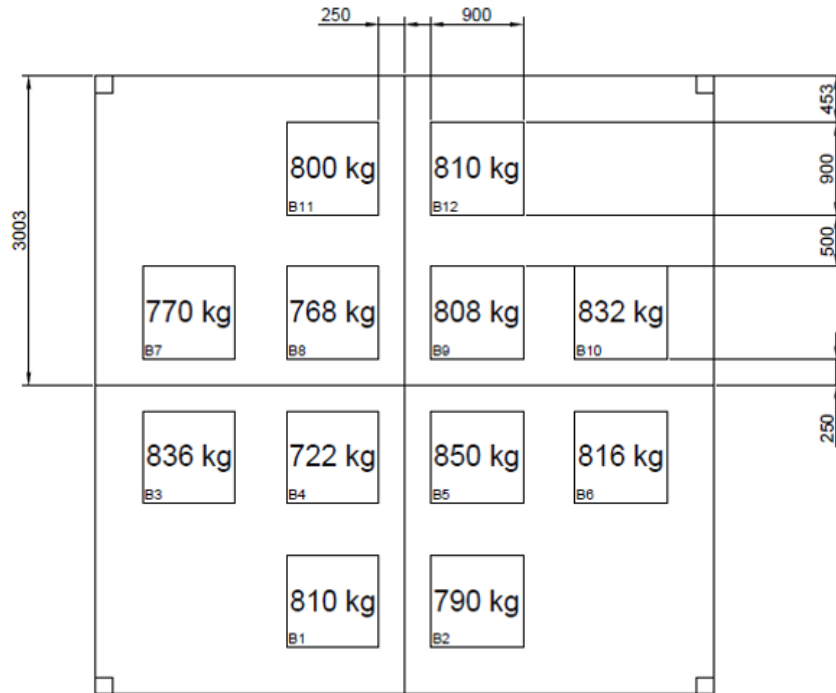


Figure 4.30: Vertical loads applied to the CLT slab. The 12 squares indicate the mass (in kg) and the location of each FIBC. The drawing dimensions are expressed in mm. Image courtesy of Marcel Muster

4.4.3. Analysis

The symmetric CLT slab is $6 \times 6 \text{ m}^2$ large and 26 cm thick. All the layers are 2 cm thick, except the two innermost ones that are 3 cm thick. Each layer of the CLT has been modelled singularly, and the bond between the layers has been assumed to be rigid. The size of the voxels used in the voxelisation step and of the FE elements of type C3D8 is $15 \times 15 \times 1 \text{ cm}^3$.

The total live load amounts to 97.9 kN and includes the vertical pressure exerted by the twelve FIBC filled by cobbles, and by the weight of a plastic cover supported by a light timber shed used to protect the slab from rain and snow. The vertical pressures exerted by each FIBC have been modelled individually, and their individual mass and position is depicted in fig. 4.30.

The main difference between the research presented in (Serantoni et al., 2018) and the analysis presented herein is the use of the integrated monitoring approach as defined by Lienhart (2007) and the identification of distinct material parameters for different partitions of the structure, as described in chapter 3. Moreover, the displacement has been calculated as described in eqn. 3.6, instead of calculating directly the distance between the deformed point cloud and the mesh obtained from the reference point cloud. The range noise σ_ρ is equal to 2 mm herein, corresponding to the range accuracy (1σ) specified in the specification sheet of the used laser

scanner (see tab. 2.1). This is a quite conservative assumption, because the value of range accuracy provided by the specification sheet² is stated to hold for a surface with 10% reflectivity at a distance of 10 m, and the normal of which is pointing towards the sensor. As for the angular accuracy, no data are available. The beam divergence ($1/e$, half angle) is equal to 0.19 mrad, but this value cannot be considered a reasonable proxy for the angular accuracy, as there exists no established relationship between these two quantities. Therefore, an angular accuracy of 0.004° has been assumed, similar to a comparable laser scanner produced by a different manufacturer (Z+F Imager 5016, see tab. 2.1). As a result, because of the modeling of the random deviations described by eqn. 3.12, the spatial distribution of the σ_δ across the slab is rather uniform.

Herein, the surface curvature has been assumed negligible, and the normals over the entire analysed surface area are approximately parallel to the vertical, i.e. the z axis of the coordinate system. Therefore, the interpolation of the node-wise perpendicular displacements can be simplified by projecting the scanned points onto the surface of the reference FE model along the z axis. The distances between each point and its projections are then used as measured values of the signal to be interpolated. In this application case, all the forces are directed vertically and the main direction of the structure's deformations is vertical as well, as no large lateral displacements are expected.

4.4.4. Results for a single partition

The three different scenarios corresponding to the three possible time intervals among the three measured epochs are listed in tab. 4.4. Each scenario is named after the epochs of the scans involved to derive the reference and the deformed point clouds, e.g. the scenario "0:2" encompasses the scans taken at the epochs 0 and 2. The numerical results of the identification for a single partition are presented in tab. 4.4, and they show that the estimated Young's deviate up to 13.7% from the a-priori value, with a minimum deviation of -4.5% for the scenario "0:2". Although plausible, unfortunately it was not possible to validate these results by a planned independent destructive test, which was part of a project at a different chair. Indeed, the destructive test has been postponed to a later date, posterior to the writing of the present thesis.

Table 4.4: CLT slab, results of the three analysed scenarios for a single partition

scenario	loads	E [MPa]	σ_E [MPa]	s_0^2/σ_0^2 [-]
0:1	self-weight	12 287	206.9	0.434
1:2	live load	12 511	68.5	0.704
0:2	self weight + live load	10 509	42.3	0.823

Concerning the accuracy of the model, we observe that the smallest σ_E is obtained for the scenario "0:2". This is plausible because this is the scenario that features

²faro.com

the best signal-to-noise ratio, as the measured displacements are the largest and the sensor accuracy is the same for all scenarios. This phenomenon can be qualitatively appreciated also looking at fig. 4.31 and fig. 4.32, which show the measured and the FE-calculated displacements of the slab, along with the spatial distribution of their differences i.e. the residuals within the LSA. The two figures refer to the scenarios "0:1" and "0:2", respectively. In particular, the displacements vary up to 26 mm, while the deviations between the predicted and the measured displacements never exceed 5 mm, and for the majority of nodes they remain below 1.5 mm.

In addition, the calculated variances are probably underestimated because they do not entirely take into consideration all the error sources of the TLS acquisition, such as mixed pixels. Moreover, the discrepancies between the behaviour of the FE model and the one of the actual structure are also probably present. In fact, the boundary conditions applied to the FE model may be oversimplified, especially as regards the constraints. This hypothesis is also supported by the values of the ratios between the a-priori and the a-posteriori variance factors (see tab. 4.4), which are lower than the unity.

Further, the difference between the estimated and the nominal material parameters could indicate either that their real values slightly differ from the nominal ones, or that the FE model has a limited correspondence to reality. First, the volume occupied by the glue in the vertical joint and between the timber layers has been modelled as filled by timber as well. Second, the cyclical changes in temperature and humidity, provoked some minor superficial cracks, which are not included in the employed FE model. Third, the TLS measurements may have been locally affected by the biasing effect of some mixed pixels located very close to the surface. These mixed pixels are due to cables hanging and to the wooden safety supports below the slab extrados, which were located especially in area beneath the centre of the slab. Since the timber is stiffer than the glue, and the presumed mixed pixels would be located below the slab, these two effects would lead to an underestimation of the slab's stiffness. Other geometric artefacts may also have been generated by surface irregularities scanned from different standpoints. Indeed, the point clouds have been cleaned by only removing the points that recognisably do not belong to it, however no further outlier removal algorithm has been implemented. In order to mitigate the effects of such artefacts, it is possible to follow three strategies: assign in the LSA lower weights to the affected nodes by increasing their associated variances; include in the processing the unbiased deformations only; or implement an outlier detection and removal algorithm. The third option would actually be the preferable one, because the first one would mix the handling of systematic and random deviations, whereas the second one would need detailed prior information about the biases. Although the discussion on outlier detection algorithms is outside the scope of this thesis, for this application example, their implementation within the LSA is not recommended. In fact, outlier detection methods such as data snooping (Baarda, 1968) and Danish method (Krarup, 1980) are computationally expensive because they require multiple iterations of the LSA. Since the available measurements are homogeneous (i.e. vertical positions acquired with TLS and geometrical

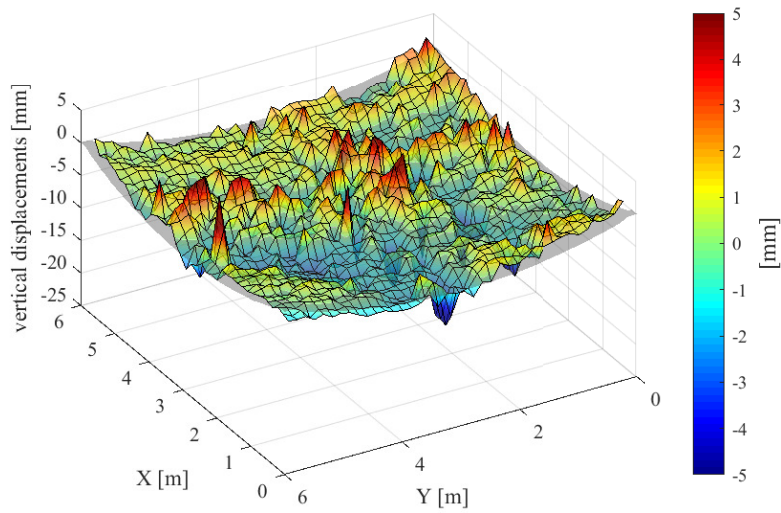


Figure 4.31: CLT slab, scenario 0:1, 1 partition. Spatial distribution of the FE-calculated nodal displacements (grey mesh) and the measured ones (coloured mesh). The colour coding represents their difference

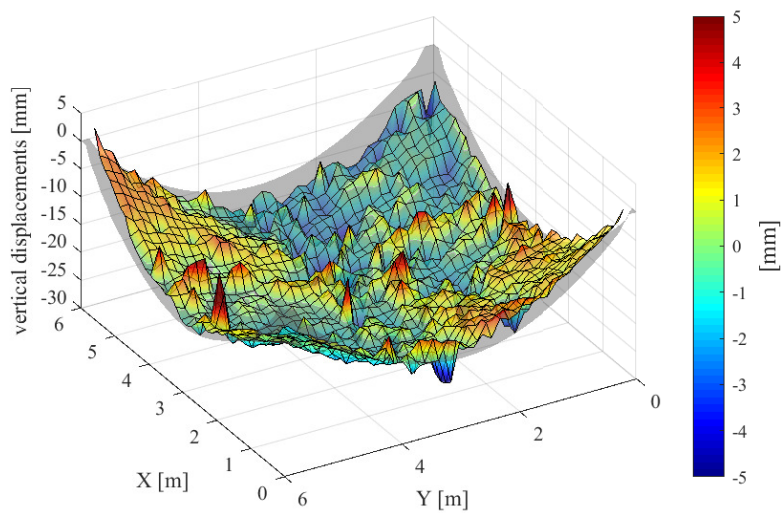


Figure 4.32: CLT slab, scenario 0:2, 1 partition. Same representation as fig. 4.31

levelling), a more sensible option is to screen the outliers at the level of the geometrical observations.

4.4.5. Results for multiple partitions

The three scenarios have been analysed for four sets of partitions (1, 2×2 , 3×3 , 4×4), similar to the simulations described in section 4.3. Also the visualisation of the results is similar: the figs. 4.33 to 4.38 present the estimated Young moduli \hat{E} and their standard deviations $\sigma_{\hat{E}}$ in colour-coded 2D plots. In all the figures depicting \hat{E} , the central value of the colour bar coincides with $E_0 = 11$ GPa. Unlike the results presented in section 4.3, when subdividing the CLT slab in multiple partitions, the $\sigma_{\hat{E}}$ close to the supports is not larger than in the centre of the slab. The reason of this difference could be the spatial distribution of the mentioned mixed pixels, which are actually concentrated below the centre of the slab.

Moreover, the fact that the CLT slab is composed of 4 glued pieces (see fig. 4.26) leads to the reasonable expectation that the variability of \hat{E} within a quarter is smaller than across different quarters. However, this cannot be clearly seen in any of the figs. 4.33, 4.35, and 4.37. What can be observed instead, is that for every scenario, both the patterns of \hat{E} and of $\sigma_{\hat{E}}$ appear to be consistent among the 3 analyses involving more than one partition, suggesting that the pattern of the results depends on the actual distribution of the measurements and not on the local random deviations of the acquired point clouds. For example, the bottom-right quarter appears less stiff than both the bottom-left and the top-right quarters for all the analysed epochs (see figs. 4.33, 4.35, and 4.37). Similar to the application case of the alloy plate (see section 4.3.1), the subdivision in multiple partitioning worsen considerably the formal accuracies $\sigma_{\hat{E}}$.

Lastly, figs. 4.39 and 4.40 show the same kind of results as figs. 4.31 and 4.32. By comparing them, it is possible to see that, despite the partitioning provides more degrees of freedom to the deformed shape, the quality of the fit does not increase remarkably, as the residuals are due mainly to random deviations and point-wise systematic errors.

Summarising, TLS is a suitable technique for this task, on the quite stringent conditions that the FE model accurately reproduces the actual and boundary conditions applied to the monitored structure, and that the systematic measurements errors are properly taken into account.

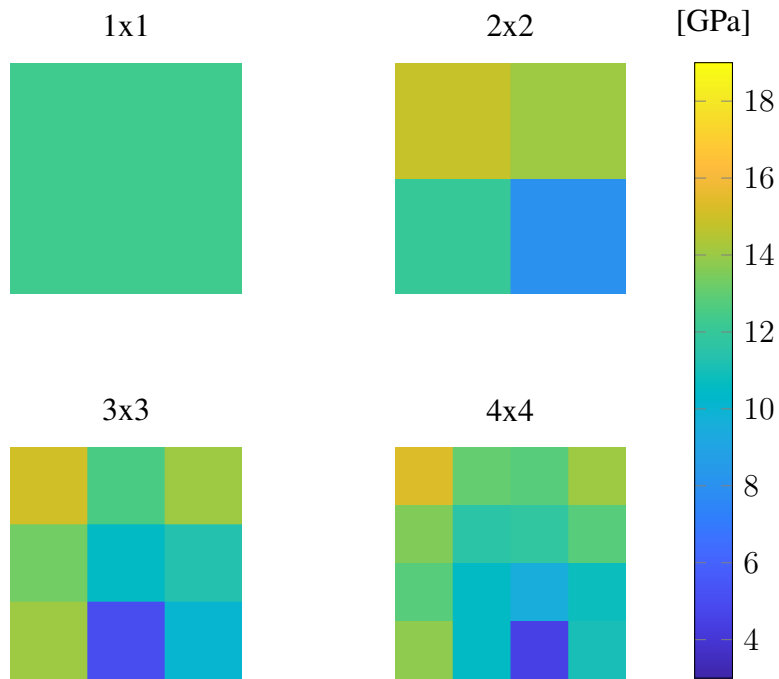


Figure 4.33: CLT slab, \hat{E} , scenario 0:1

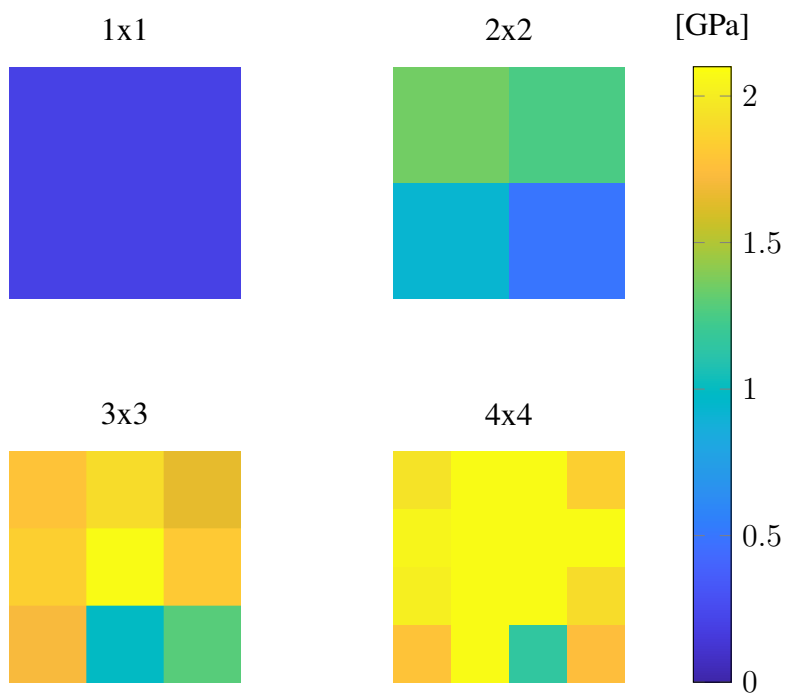


Figure 4.34: CLT slab, $\sigma_{\hat{E}}$, scenario 0:1

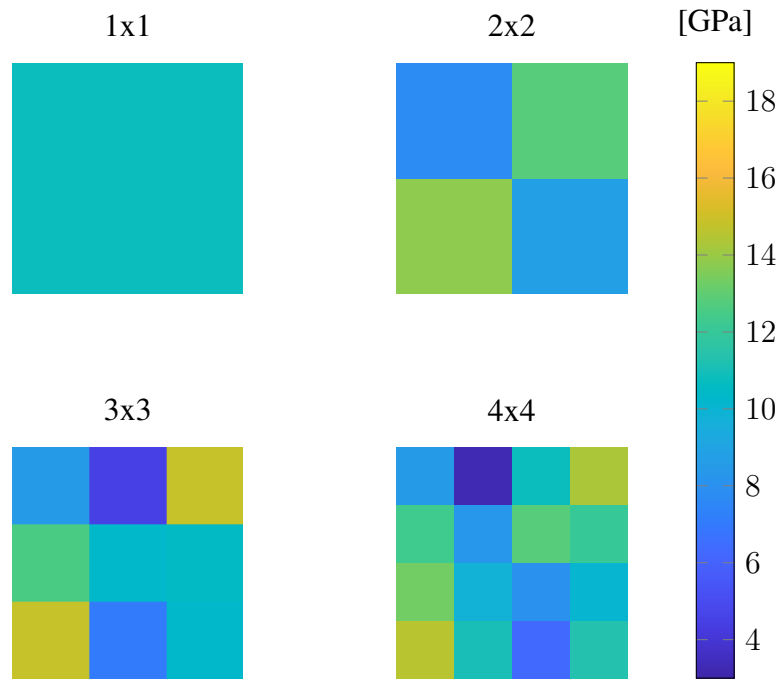


Figure 4.35: CLT slab, \hat{E} , scenario 0:2

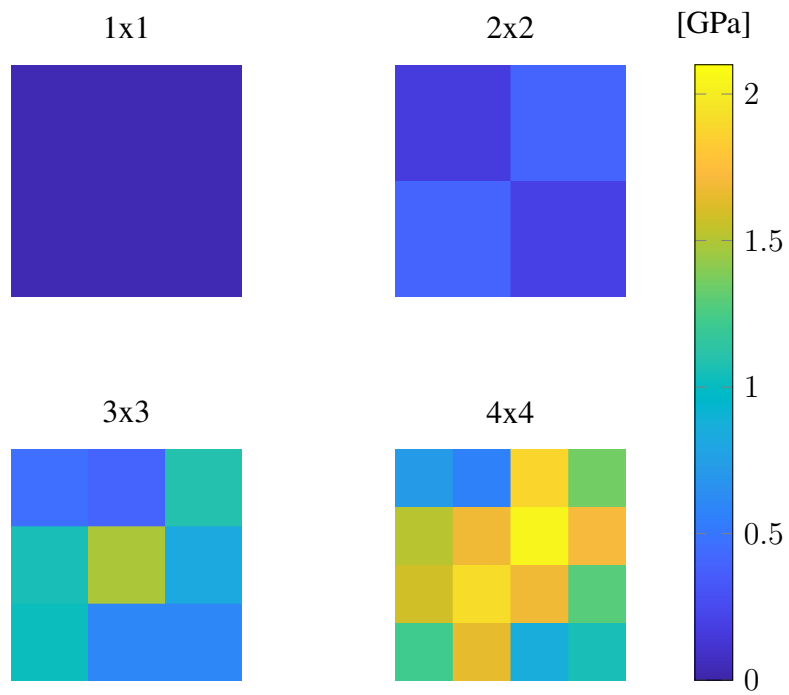


Figure 4.36: CLT slab, $\sigma_{\hat{E}}$, scenario 0:2

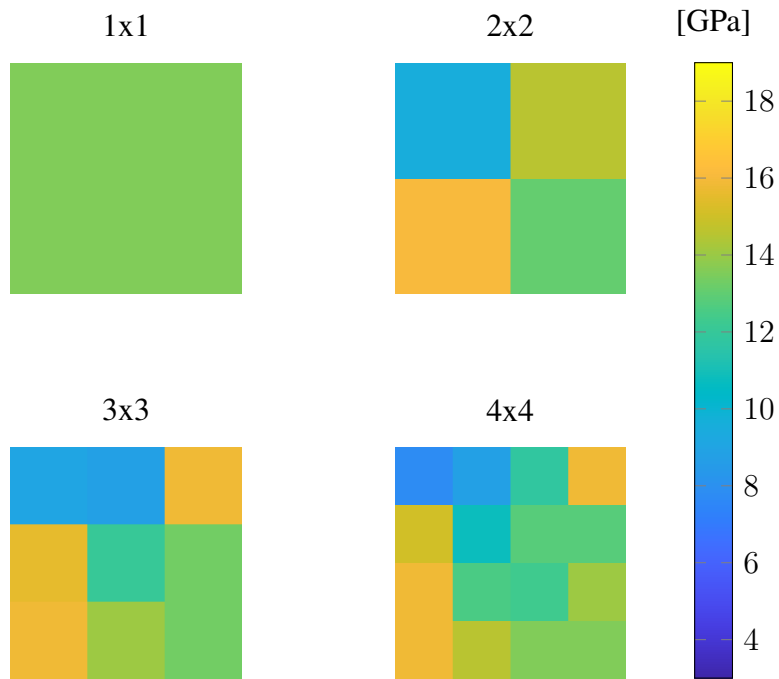


Figure 4.37: CLT slab, \hat{E} , scenario 1:2

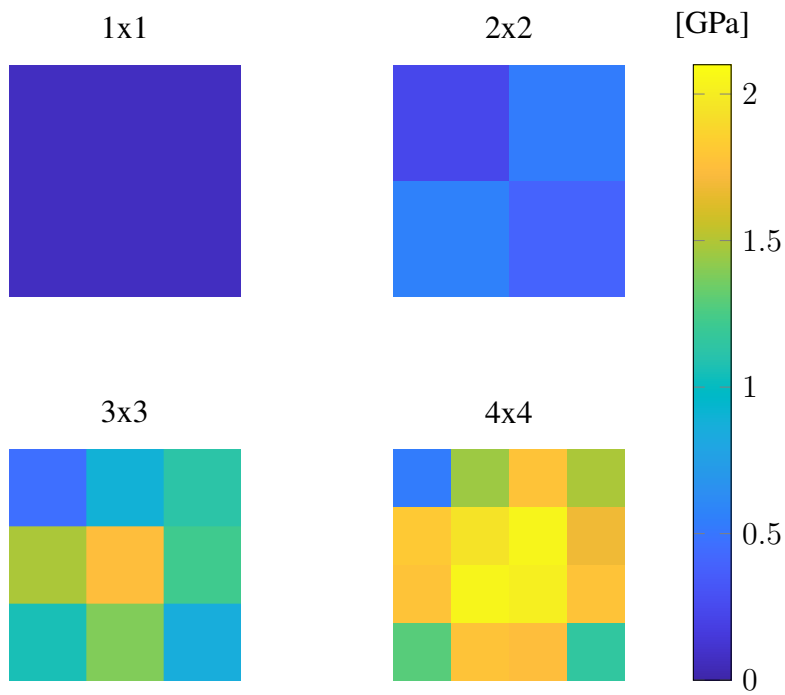


Figure 4.38: CLT slab, $\sigma_{\hat{E}}$, scenario 1:2

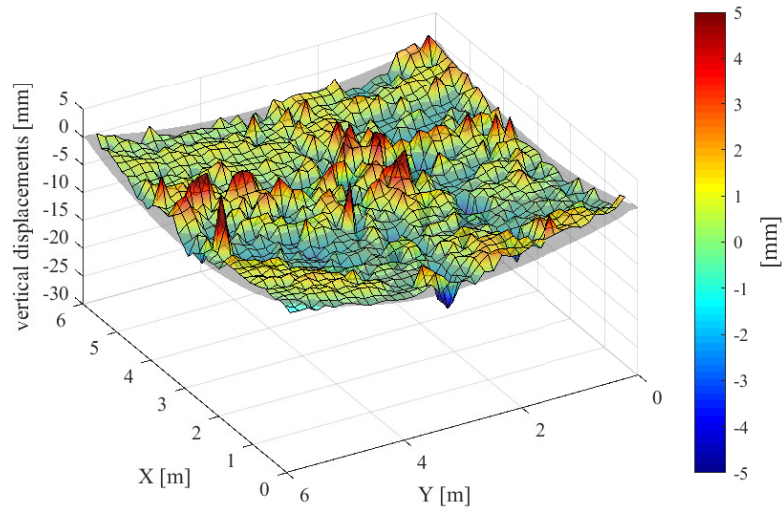


Figure 4.39: CLT slab, scenario 0:1 4×4 partitions. Spatial distribution of the FE-calculated nodal displacements (grey mesh) and the measured ones (coloured mesh). The colour coding represents their difference

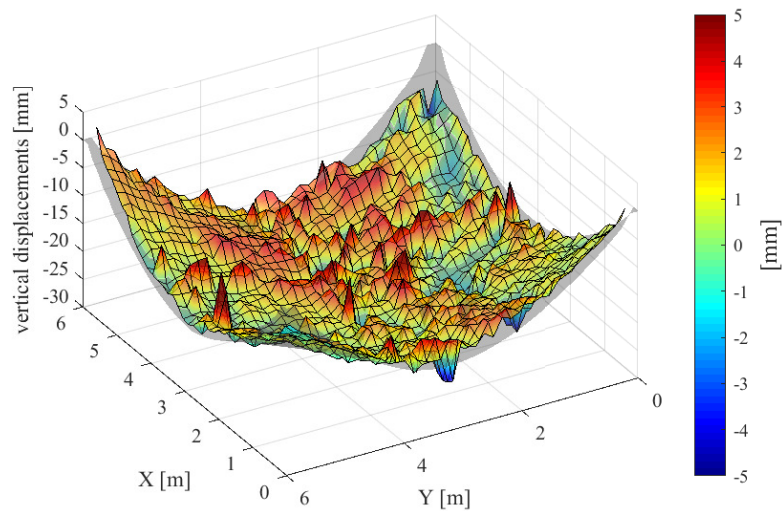


Figure 4.40: CLT slab, scenario 0:2 4×4 partitions. Same representation as in fig. 4.39

5. Conclusion and outlook

This research represents a first step towards the automation and combination of TLS deformation monitoring and its mechanical interpretation, thus shifting and widening the paradigm for geodetic monitoring tasks. More specifically, this work expands the range of applications of the integrated monitoring approach, as it embodies a novel method to perform the numerical identification of structures by using point cloud data acquired with terrestrial laser scanners in multiple epochs.

This method has been developed in the framework of integrated analysis, which relies on the linearisation of a FE model within an iterative LSA. The criterion underlying the LSA is the matching of the FE-calculated displacement with the measured ones. Given the flexibility of the integrated monitoring approach, the method is well suited to process complementary data from additional sensors and sources. For example, sensor fusion could be used to overcome the limitations of TLS in detecting in-plane displacements.

Within the LSA, the functional relationship between forces, displacements, and material parameters is established by linearising the output of the FE model with respect to the desired parameters, which are either nodal forces or material parameters within the stiffness matrix. In this way, the FE model is treated as a "black box", and any FE solver can be theoretically used for the scope. Within this thesis, the software package Abaqus has been used.

Because of the interest in exploiting TLS technology to the best of its capabilities, the point cloud data have been used not only for the determination of the deformations of the investigated object, but also to generate the mesh of the FE model. The generation of the FE model has been conducted by voxelising the volume enclosed by the point cloud of the investigated structure's surface. This method has been developed in order to effectively model free-form 3D objects.

Besides the TLS-measured displacements, which are calculated applying classical methods of geodetic areal deformation monitoring, also their accuracy has been determined and passed as an input to the LSA. In particular, the variance-covariance matrices of the TLS-acquired points have been modelled by considering the accuracy of the two angular measurements, the accuracy of the ranging unit, and the uncertainty increase due to non-perpendicular angles of incidence. This stochastic information has been subsequently interpolated at the FE nodes by using three distinct

approaches: (i) the classical variance propagation, (ii) the Log-Euclidean interpolation, and (iii) the nearest neighbour search. After a comparison of the performance of these three alternative approaches, the approach (iii) has been adopted because of its computational efficiency. However, all three approaches represent viable options and they may be selected according to the assumptions and properties that hold for the specific application case.

The estimation of the parameters has been detailed in its general formulation and for the specific application case of areal displacements. Particular focus has been dedicated to the pre-elimination of the non-observed nodal displacements, and to the possibility of automatically subdivide the FE mesh in several partitions, in order to estimate multiple parameters for different portions of the structure. The LSA has been then validated with closed-loop tests, including a Monte Carlo simulation, which suggested that the hypothesis of equality between the empirical and the formal standard deviations is not rejected for $\alpha > 0.007$.

Moreover, some additional investigations on the numerics of the method implementation lead to the conclusions that (i) an accurate numerical differentiation requires precise FE displacements, e.g. in double precision, (ii) the suitable range for the step size used for the numerical differentiation is from 4 to 2 orders of magnitude smaller than E , and (iii) the size of the numerical biases intrinsic in the implemented realisation of the algorithm is 0.01 mm.

Lastly, the proposed method has been applied on three structures: a simulated steel beam, a simulated alloy plate, and a real CLT slab. The measurements of the two simulated scenarios have been created by using a self-developed synthetic point cloud generator, which takes into account the position of the sensor, its resolution and its accuracy specifications. Additionally, the point cloud generator has been also embedded in a simulation tool that enables to plan the measurements and to predict their expected accuracy before their actual execution.

The application examples showed that the method works and it is particularly accurate when evaluating one value of the Young modulus for the whole structure. For example, when using data from a laser scanner with $\sigma_\rho = 1$ mm, the accuracy of the estimation of E is below 0.5% for two considered application cases. The method shows some limitations when estimating a large number of parameters, as they affects strongly the precision of the results, especially if the a-priori information on the corresponding parameters is far from their actual values. Moreover, a low sensitivity of the different partitions with respect to the sought parameters affects the accuracy of their estimation. Lastly, despite the absence of ground truth data, the results of the application case with real data are plausible, with a deviation of 4.5% from the presumed values of E . Various assumptions have been made across this work and the most critical one is that the structural constraints are explicitly specified in the FE model, relying on the engineer's physical understanding of the investigated structure, as the CLT application case demonstrates.

The developed method could be further extended and validated by implementing

the following improvements.

- The set of modelled error sources that may affect the results should be enlarged, considering further effects such as the registration error, the scanner instability, the atmospheric effects, and the reflectivity- and intensity-dependent biases.
- Although conceptually equivalent to the identification of the material parameters, the determination of the loads acting on the investigated structure (inverse problem) should be tested and validated.
- The simulation tool should be embedded in a multi-dimensional grid search algorithm that determines a-priori the optimal scanning setup (i.e. resolution, accuracy, standpoint location) for a given monitoring case. Additionally, such planning tool could also be used to define a procedure that helps to decide the location and the type of additional geodetic sensors, by analysing the sensitivity of the desired parameters to the available measurements. Such an analysis would not need the acquisition of actual measurements, but only a FE model of the structure.
- The simulation tool should embed a sensitivity analysis module, in order to quantify the relative importance of each scanning setting with respect to each estimated parameter. This could be accomplished with the use of an uncertainty quantification framework such as UQLab (Marelli and Sudret, 2014).
- The method could be tested on a wider range of application cases, including a broader range of materials, shapes, TLS properties, and surface properties. Furthermore, the application of the method to detect and localise damages in a structure could be investigated as well.

To conclude, the presented method extends the range of application of TLS in the field of SHM. In fact, it enables the automatic generation of the geometry of the FE model from TLS data, the extension of the analysis of the monitored structures from the determination of geometrical deformations to the identification of material parameters, and the simulation and the prediction of the expected accuracy before the execution of the actual measurements. The method is effective for the identification of various kind of structures, the geometry and the deformation of which are derived by TLS data. A potential application of the proposed method is the structural health monitoring of structures such as free-form structural members or parts of cultural heritage buildings.

A. Acronyms

AMCW	Amplitude-Modulated Continuous-Wave
ASCII	American Standard Code for Information Interchange
BC	Boundary Condition
BIM	Building Information Modelling
C2M	Cloud-to-Mesh
C2C	Cloud-to-Cloud
CLT	Cross Laminated Timber
FEM	Finite Element Method
FIBC	Flexible Intermediate Bulk Container
GNSS	Global Navigation Satellite Systems
InSAR	Interferometric Synthetic Aperture Radar
LSA	Least Squares Adjustment
NN	Nearest Neighbour
NURBS	Non Uniform Rational B-Splines
PDE	Partial Differential Equation
RMS	Root Mean Square
RS	Reference System

SI	Système International d'unités
SOFO	Surveillance d'Ouvrages par Fibres Optiques
TLS	Terrestrial Laser Scanning
VCM	Variance-Covariance Matrix

List of Figures

1.1	Productivity in the USA, 1947-2010	2
1.2	Productivity in the UK, 1997-2017	3
2.1	Adopted convention for spherical coordinates	10
2.2	Tonti diagram of elastostatics	16
2.3	Examples of Abaqus continuum finite element types	17
3.1	System analysis: input, transfer function, output	20
3.2	The block diagram of the proposed method	21
3.3	illustration of alpha shapes	24
3.4	The discretisation process	24
3.5	The discretisation effect	25
3.6	Relative distribution of FE nodes and TLS measurements	27
3.7	Calculation of distances	29
3.8	Linear triangular interpolation	30
3.9	Skinny triangles	31
3.10	Illustration of VCM interpolation	32
3.11	Local VCM reference system	33
3.12	Cosine deterioration of σ_ρ	34
3.13	Outcomes for variance propagation, Log-Euclidean interpolation, and Nearest Neighbour search for common input data	40
3.14	Outcomes for variance propagation, Log-Euclidean interpolation, and Nearest Neighbour search for common input data, different scale	41
3.15	Example of a partitioned beam	50
3.16	Validation of $\sigma_{\hat{E}}$. $\sigma_d = 1$ mm, $E_0 = 210$ GPa	52
3.17	Validation of $\sigma_{\hat{E}}$. $\sigma_d = 2$ mm, $E_0 = 210$ GPa	53
3.18	Validation of $\sigma_{\hat{E}}$. $\sigma_d = 1$ mm, $E_0 = 220$ GPa	54
3.19	Validation of $\sigma_{\hat{E}}$. $\sigma_d = 10$ mm, $E_0 = 220$ GPa	55
3.20	Visual representation of the entries of \mathbf{A}_p for different numbers of partitions	60
3.21	The function $\mathbf{u} = \mathbf{u}(E)$ for a simply supported beam	62
3.22	Search of a suitable step size for numerical differentiation	63
3.23	Ratio between the prior and the posterior variance factors, for dif- ferent values of σ_d	65

4.1	Noise generation procedure for synthetic scans	70
4.2	Sketch of the simulation setup	72
4.3	3D deformed shape of the steel beam	73
4.4	Steel beam: spatial distribution of displacements in the three directions and von Mises stresses	73
4.5	Full simulation of a beam. $\sigma_\rho = 1$ mm, $E_0 = 210$ GPa	76
4.6	$\bar{\sigma}_{E_i}$ for various number of partitions and various noise levels σ_ρ , $E_0 = E_{\text{true}} = 210$ GPa	77
4.7	σ_{E_i} for various number of partitions and various noise levels σ_ρ from 10^{-6} to 10^{-2} m, $E_0 = E_{\text{true}} = 210$ GPa	78
4.8	Correlation matrices for 3, 8, and 24 partitions and two noise levels σ_ρ . $E_0 = E_{\text{true}} = 210$ GPa	79
4.9	2D view of the measured displacements, the simulated displacements, and the FE nodes in the undeformed configurations. 1 partition	80
4.10	Heatmap of the standpoint-dependent bias	81
4.11	Heatmap of the standpoint-dependent expected accuracy	82
4.12	3D deformed shape of the alloy plate	83
4.13	Alloy plate: spatial distribution of nodal displacements and von Mises stresses	84
4.14	Alloy plate, \hat{E} for different numbers of partitions, $\sigma_\rho = 1 \times 10^{-4}$ m, $E_{\text{true}} = 72$ GPa	85
4.15	Alloy plate, $\sigma_{\hat{E}}$ for different numbers of partitions, $\sigma_\rho = 1 \times 10^{-4}$ m, $E_{\text{true}} = 72$ GPa	85
4.16	Alloy plate, \hat{E} for different numbers of partitions, $\sigma_\rho = 5 \times 10^{-4}$ m, $E_{\text{true}} = 72$ GPa	86
4.17	Alloy plate, $\sigma_{\hat{E}}$ for different numbers of partitions, $\sigma_\rho = 5 \times 10^{-4}$ m, $E_{\text{true}} = 72$ GPa	86
4.18	Alloy plate, \hat{E} for different numbers of partitions, $\sigma_\rho = 1 \times 10^{-3}$ m, $E_{\text{true}} = 72$ GPa	87
4.19	Alloy plate, $\sigma_{\hat{E}}$ for different numbers of partitions, $\sigma_\rho = 1 \times 10^{-3}$ m, $E_{\text{true}} = 72$ GPa	87
4.20	Alloy plate, \hat{E} for different numbers of partitions, $\sigma_\rho = 2 \times 10^{-3}$ m, $E_{\text{true}} = 72$ GPa	88
4.21	Alloy plate, $\sigma_{\hat{E}}$ for different numbers of partitions, $\sigma_\rho = 2 \times 10^{-3}$ m, $E_{\text{true}} = 72$ GPa	88
4.22	Alloy plate, \hat{E} for different numbers of partitions, $\sigma_\rho = 5 \times 10^{-3}$ m, $E_{\text{true}} = 72$ GPa	89
4.23	Alloy plate, $\sigma_{\hat{E}}$ for different numbers of partitions, $\sigma_\rho = 5 \times 10^{-3}$ m, $E_{\text{true}} = 72$ GPa	89
4.24	Alloy plate, \hat{E} for different numbers of partitions, $\sigma_\rho = 1 \times 10^{-2}$ m, $E_{\text{true}} = 72$ GPa	90
4.25	Alloy plate, $\sigma_{\hat{E}}$ for different numbers of partitions, $\sigma_\rho = 1 \times 10^{-2}$ m, $E_{\text{true}} = 72$ GPa	90
4.26	CLT slab	92
4.27	Principal directions of timber	92

4.28	Photos of the TLS monitoring of the CLT slab	94
4.29	TLS and levelling monitoring of the CLT slab	94
4.30	Vertical loads applied to the CLT slab	95
4.31	CLT slab, scenario 0:1, 1 partition	98
4.32	CLT slab, scenario 0:2, 1 partition	98
4.33	CLT slab, \hat{E} , scenario 0:1	100
4.34	CLT slab, $\sigma_{\hat{E}}$, scenario 0:1	100
4.35	CLT slab, \hat{E} , scenario 0:2	101
4.36	CLT slab, $\sigma_{\hat{E}}$, scenario 0:2	101
4.37	CLT slab, \hat{E} , scenario 1:2	102
4.38	CLT slab, $\sigma_{\hat{E}}$, scenario 1:2	102
4.39	CLT slab, scenario 0:1, 4×4 partitions	103
4.40	CLT slab, scenario 0:2, 4×4 partitions	103

List of Tables

2.1	Summary of the main accuracy and resolution specifications for a selection of market-available terrestrial laser scanners	12
3.1	Interpolation methods: comparison of processing time	39
3.2	Results of the Monte Carlo validation	59
4.1	A list of construction materials and their mechanical properties. . .	68
4.2	Choice of the finite elements: comparison of the deflection at mid-span with the analytic solution	72
4.3	Timber stiffness relations and values of the Poisson's ratios	93
4.4	CLT slab, results of the three analysed scenarios for a single partition	96

Bibliography

- D. Adamson, M. Alfaro, J. Blatz, and K. Bannister. Construction and Post-Construction Deformation Analysis of an MSE Wall Using Terrestrial Laser Scanning. In *Geo-Congress 2020: Engineering, Monitoring, and Management of Geotechnical Infrastructure*, pages 767–777, Reston, VA, 2020. American Society of Civil Engineers.
- N. Akkiraju, H. Edelsbrunner, M. Facello, P. Fu, E. P. Mücke, and C. Varela. Alpha shapes: definition and software, 1995.
- R. C. Alves, J. N. Mantilla, C. F. Bremer, and E. V. Carrasco. Application of acoustic tomography and ultrasonic waves to estimate stiffness constants of muiracatiara brazilian wood. *BioResources*, 10(1):1845–1856, 2015.
- I. Amidror. Scattered data interpolation methods for electronic imaging systems: a survey. *Journal of Electronic Imaging*, 11(2):157, 2002.
- Y. An, E. Chatzi, S. H. Sim, S. Laflamme, B. Blachowski, and J. Ou. Recent progress and future trends on damage identification methods for bridge structures. *Structural Control and Health Monitoring*, 26(10):1–30, 2019.
- G. Angjeliu, G. Cardani, and D. Coronelli. A parametric model for ribbed masonry vaults. *Automation in Construction*, 105(March):102785, 2019.
- D. Antón, B. Medjdoub, R. Shrahily, and J. Moyano. Accuracy evaluation of the semi-automatic 3D modeling for historical building information models. *International Journal of Architectural Heritage Conservation, Analysis, and Restoration*, 2018.
- R. Argiolas, A. Cazzani, E. Reccia, and V. Bagnolo. From LiDAR data towards HBIM for structural evaluation. *ISPRS - International Archives of the Photogrammetry, Remote Sensing and Spatial Information Sciences*, XLII-2/W15: 125–132, 2019.
- V. Arsigny, P. Fillard, X. Pennec, and N. Ayache. Log-Euclidean metrics for fast and simple calculus on diffusion tensors. *Magnetic Resonance in Medicine*, 56(2):411–421, 2006.

- W. Baarda. A Testing Procedure for Use in Geodetic Networks. *Publications on Geodesy*, 2(5):97, 1968.
- L. Barazzetti, F. Banfi, R. Brumana, G. Gusmeroli, M. Previtali, and G. Schiantarelli. Cloud-to-BIM-to-FEM: Structural simulation with accurate historic BIM from laser scans. *Simulation Modelling Practice and Theory*, 57:71–87, 2015.
- M. Barbarella, M. Fiani, and A. Lugli. Uncertainty in terrestrial laser scanner surveys of landslides. *Remote Sensing*, 9(2):113, 2017.
- L. L. Beghini, A. Beghini, N. Katz, W. F. Baker, and G. H. Paulino. Connecting architecture and engineering through structural topology optimization. *Engineering Structures*, 59:716–726, 2014.
- P. J. Besl and N. D. McKay. Method for registration of 3-D shapes. In P. S. Schenker, editor, *Sensor Fusion IV: Control Paradigms and Data Structures*, volume 1611, pages 586–606. International Society for Optics and Photonics, 1992.
- A. Bienert. *Automatische Extraktion von 3D-Baumparametern aus terrestrischen Laserscannerdaten*. Dissertation, TU Dresden, 2013.
- G. Bitelli, G. Castellazzi, A. M. D’Altri, S. De Miranda, A. Lambertini, and I. Selvaggi. On the generation of numerical models from point clouds for the analysis of damaged Cultural Heritage. *IOP Conference Series: Materials Science and Engineering*, 364(1):012083, 2018.
- J. Bodig and B. Jayne. *Mechanics of wood and wood composites*. Krieger Publishing Company, 1982.
- R. Brumana, S. Della Torre, M. Previtali, L. Barazzetti, L. Cantini, D. Oreni, and F. Banfi. Generative HBIM modelling to embody complexity (LOD, LOG, LOA, LOI): surveying, preservation, site intervention—the Basilica di Collemaggio (L’Aquila). *Applied Geomatics*, 10(4):545–567, 2018.
- I. Bucur-Horváth and R. V. Saplacan. Force lines embodied in the building: Palazzetto dello sport. *Journal of the International Association for Shell and Spatial Structures*, 54(176-177):179–188, 2013.
- W. F. Caspary. *Concepts of Network and Deformation Analysis*. School of Surveying, The University of New South Wales, 2000.
- S. Chaudhry, D. Salido-Monzú, and A. Wieser. Simulation of 3D laser scanning with phase-based EDM for the prediction of systematic deviations. In *Modeling Aspects in Optical Metrology VII*, volume 11057, page 110570H, Munich, Germany, 2019. International Society for Optics and Photonics.
- Y. Chen and G. Medioni. Object modeling by registration of multiple range images, 1991.

- A. Chrzanowski, Y.-Q. Chen, J. M. Secord, A. Szostak-Chrzanowski, Chen Yong-Qi, J. M. Secord, and A. Szostak-Chrzanowski. Problems and solutions in the integrated monitoring and analysis of dam deformations. *CISM Journal ACSGC*, 45(4):547–560, 1991.
- J. A. Cottrell, T. J. R. Hughes, and Y. Bazilevs. *Isogeometric Analysis : Toward Unification of CAD and FEA*. John Wiley & Sons, 2009.
- F. da Porto, M. Valluzzi, and C. Modena. Use of sonic tomography for the diagnosis and the control of intervention in historic masonry buildings. *International Symposium - Non Destructive Testing in civil engineering, Germany*, 2003.
- Dassault Systèmes. *Abaqus 6.14 Documentation*. 2013.
- A. Deraemaeker and K. Worden, editors. *New Trends in Vibration Based Structural Health Monitoring*. Number 520. Springer, Wien, 1 edition, 2010.
- Y. L. Desnos, M. Foumelis, M. Engdahl, P. P. Mathieu, F. Palazzo, and F. Ramoino. Sentinel-1 mission scientific exploitation activities. In *International Geoscience and Remote Sensing Symposium (IGARSS)*, volume 2017-July, pages 5521–5524. IEEE, 2017.
- G. Dieter. *Mechanical Metallurgy*. McGraw-Hill, New York, 1986.
- C. Dold and C. Brenner. Registration of terrestrial laser scanning data using planar patches and image data. *International Archives of Photogrammetry, ...*, Vol. XXXVI(5):78–83, 2006.
- S. A. Dudani. The Distance-Weighted k-Nearest-Neighbor Rule. *IEEE Transactions on Systems, Man, and Cybernetics 4*, pages 325–327, 1976.
- N. Dunn. *Digital fabrication in architecture*. Laurence King, London, 2012.
- H. Edelsbrunner and E. P. Mücke. Three-Dimensional Alpha Shapes. *ACM Transactions on Graphics (TOG)*, 13(1):43–72, 1994.
- M. Ehrhart. *Applications of image-assisted total stations: Concepts, experiments, results and calibration*. Dissertation, TU Graz, 2017.
- R. Fahrni. *Finite-element modeling of timber connections*. Master thesis, ETH Zurich, 2016.
- C. R. Farrar and K. Worden. An introduction to structural health monitoring. *Philosophical transactions. Series A, Mathematical, physical, and engineering sciences*, 365(1851):303–315, 2007.
- R. Ferrari, F. Pioldi, E. Rizzi, C. Gentile, E. Chatzi, R. Klis, E. Serantoni, and A. Wieser. Heterogeneous sensor fusion for reducing uncertainty in structural health monitoring. *UNCECOMP 2015 - 1st ECCOMAS Thematic Conference on*

Uncertainty Quantification in Computational Sciences and Engineering, 4289 (May):511–528, 2015.

- R. Ferrari, F. Pioldi, E. Rizzi, C. Gentile, E. Chatzi, E. Serantoni, and A. Wieser. Fusion of wireless and non-contact technologies for the dynamic testing of a historic RC bridge. *Measurement Science and Technology*, 27(12), 2016.
- V. Frangez, E. Serantoni, and A. Wieser. Geodetic Monitoring of Digitally Fabricated Structures Early After Construction. In *FIG2020 Working Week: Smart surveyors for land and water management*, Amsterdam, 2020.
- R. Franke. Scattered Data Interpolation: Tests of Some Method. *Mathematics of Computation*, 38(157):181, 1982.
- E. Friedli and A. Wieser. Identification of stable surfaces within point clouds for areal deformation monitoring. In *3rd Joint International Symposium on Deformation Monitoring (JISDM)*, Vienna, Austria, 2016.
- J. D. Gardiner, J. Behnsen, and C. A. Brassey. Alpha shapes: Determining 3D shape complexity across morphologically diverse structures. *BMC Evolutionary Biology*, 18(1):1–16, 2018.
- D. Girardeau-Montaut. *Détection de changement sur des données géométriques tridimensionnelles*. Dissertation, Telecom ParisTech, 2006.
- Z. Gojcic, C. Zhou, and A. Wieser. F2S3 : Robustified determination of 3D displacement vector fields using deep learning. *Journal of Applied Geodesy*, Ahead of p, 2020.
- B. Gordon. *Zur Bestimmung von Messunsicherheiten terrestrischer Laserscanner*. Dissertation, TU Darmstadt, 2008.
- C. Harmening and H. Neuner. A spatio-temporal deformation model for laser scanning point clouds. *Journal of Geodesy*, 94(26), 2020.
- W. He, W. Ma, and H. Zha. Automatic registration of range images based on correspondence of complete plane patches. In *Proceedings of International Conference on 3-D Digital Imaging and Modeling, 3DIM*, pages 470–475, 2005.
- O. Heunecke, H. Kuhlmann, W. M. Welsch, and A. Eichhorn. *Handbuch Ingenieurgeodäsie*. Wichmann, 2. edition, 2013.
- C. Holst and H. Kuhlmann. TLS-basierte Deformationsanalyse unter Nutzung von Standardsoftware. *DVW e.V. (Hrsg.): Terrestrisches Laserscanning 2016 (TLS 2016)*, Band 85/20(November 2006):39–58, 2016.
- C. Holst, D. Schunck, A. Nothnagel, R. Haas, L. Wennerbäck, H. Olofsson, R. Hammargren, and H. Kuhlmann. Terrestrial laser scanner two-face measurements for analyzing the elevation-dependent deformation of the onsala space

- observatory 20-m radio telescope's main reflector in a bundle adjustment. *Sensors (Switzerland)*, 17(8), 2017.
- C. Holst, T. Medic, A. Nothnagel, and H. Kuhlmann. Analyzing shape deformation and rigid body movement of structures using commonly misaligned terrestrial laser scanners: the radio telescope case. In *4th Joint International Symposium on Deformation Monitoring (JISDM)*, Athens, Greece, 2019a.
- C. Holst, A. Nothnagel, R. Haas, and H. Kuhlmann. Investigating the gravitational stability of a radio telescope's reference point using a terrestrial laser scanner: Case study at the Onsala Space Observatory 20-m radio telescope. *ISPRS Journal of Photogrammetry and Remote Sensing*, 149:67–76, 2019b.
- R. G. Holstein, A. N. Palazotto, and R. G. Cobb. Structural design considerations of an inflatable rigidizable space shuttle experiment. *Journal of Aerospace Engineering*, 22(2):123–133, 2009.
- I. Hotz, J. Sreevalsan-Nair, H. Hagen, and B. Hamann. Tensor field reconstruction based on eigenvector and eigenvalue interpolation. *Dagstuhl Follow-Ups*, 1:110–123, 2010.
- L. Hu, J. Xiao, and Y. Wang. Efficient and automatic plane detection approach for 3-D rock mass point clouds. *Multimedia Tools and Applications*, 2019.
- T. J. R. Hughes. *The finite element method : linear static and dynamic finite element analysis*. Dover Publications, 2000.
- T. J. R. Hughes, J. Cottrell, and Y. Bazilevs. Isogeometric analysis: CAD, finite elements, NURBS, exact geometry and mesh refinement. *Computer Methods in Applied Mechanics and Engineering*, 194(39-41):4135–4195, 2005.
- R. Jäger, M. Bertges, J. Reiner, and M. Bertges. Integrierte Modellbildung zum permanenten Monitoring von Bauwerken und geotechnischen Anlagen. In *Beiträge zum 61. DVW-Fortbildungseminar am 27. und 28. September 2004 an der Bauhaus-Universität Weimar*, pages 21–40, Weimar, 2004.
- J. Janßen, T. Medic, H. Kuhlmann, and C. Holst. Decreasing the uncertainty of the target center estimation at terrestrial laser scanning by choosing the best algorithm and by improving the target design. *Remote Sensing*, 11(7), 2019.
- H. C. Jo, H. G. Sohn, and Y. M. Lim. A LiDAR Point Cloud Data - Based Method for Evaluating Strain on a Curved Steel Plate Subjected to Lateral Pressure. *Sensors*, 20(3), 2020.
- C. Johnson. *Numerical solution of partial differential equations by the finite element method*. Dover Publications, 2000.

- J. Jung, S. Hong, S. Yoon, J. Kim, and J. Heo. Automated 3D Wireframe Modeling of Indoor Structures from Point Clouds Using Constrained Least-Squares Adjustment for As-Built BIM. *Journal of Computing in Civil Engineering*, 30(4):04015074, 2016.
- S. Kälber and R. Jäger. Realisierung eines GPS-basierten Online Kontroll- und Alarmsystems (GOCA) und Diskussion adäquater geometrischer und systemanalytischer Ansätze zum online Monitoring im Talsperrenbereich. In *Journal of the University of Applied Sciences Mittweida. Workshop "Messtechnische Lösungen bei der Überwachung von Talsperren"*, volume 2, pages 73–78, 2000.
- G. Kermarrec, H. Alkhatib, J. Bureick, and B. Kargoll. Impact of mathematical correlations on the statistic of the congruency test case study: B-splines surface approximation from bridge observations. In *4th Joint International Symposium on Deformation Monitoring (JISDM)*, Athens, Greece, 2019.
- K. Kim, J. Kim, and H. Sohn. Development and full-scale dynamic test of a combined system of heterogeneous laser sensors for structural displacement measurement. *Smart Materials and Structures*, 25(6):065015, 2016.
- S. Kim, D. Sohn, and S. Im. Construction of polyhedral finite element meshes based upon marching cube algorithm. *Advances in Engineering Software*, 128 (November 2018):98–112, 2019.
- T. Krarup. Gotterdammerung over least squares adjustment. *Proc. 14th Congress of the International Society of Photogrammetry*, 3:369–378, 1980.
- D. Le Bihan, J. F. Mangin, C. Poupon, C. A. Clark, S. Pappata, N. Molko, and H. Chabriat. Diffusion tensor imaging: Concepts and applications. *Journal of Magnetic Resonance Imaging*, 13(4):534–546, 2001.
- H. M. Lee and S. P. Hyo. Stress Estimation of Beam Structures Based on 3D Coordinate Information from Terrestrial Laser Scanning. *Proceedings of the Third International Conference on Control, Automation and Systems Engineering*, pages 81–83, 2013.
- D. D. Lichti. Error modelling, calibration and analysis of an AM-CW terrestrial laser scanner system. *ISPRS Journal of Photogrammetry and Remote Sensing*, 61(5):307–324, 2006.
- D. D. Lichti, S. J. Gordon, and T. Tipdecho. Error Models and Propagation in Directly Georeferenced Terrestrial Laser Scanner Networks. *Journal of Surveying Engineering*, 131(4):135–142, 2005.
- W. Lienhart. *Analysis of Inhomogeneous Structural Monitoring Data*. Dissertation, TU Graz, 2007.

- S. Marelli and B. Sudret. UQLab: A Framework for Uncertainty Quantification in Matlab. In *Vulnerability, Uncertainty, and Risk*, number Bourinet 2009, pages 2554–2563, 2014.
- P. Mazzanti. Remote monitoring of deformation. An overview of the seven methods described in previous GINs, 2012.
- McKinsey Global Institute. Reinventing Construction: A Route To Higher Productivity. Technical report, McKinsey & Company, 2017.
- T. Medić, H. Kuhlmann, and C. Holst. Automatic in-situ self-calibration of a panoramic TLS from a single station using 2D keypoints. *ISPRS Annals of the Photogrammetry, Remote Sensing and Spatial Information Sciences*, 4(2/W5):413–420, 2019.
- T. Mill. Simulation of terrestrial laser scanning errors occurring during deformation monitoring. In *3rd Joint International Symposium on Deformation Monitoring (JISDM)*, Vienna, Austria, 2016.
- T. Möller and B. Trumbore. Fast, Minimum Storage Ray-Triangle Intersection. *Journal of Graphics Tools*, 2(1):21–28, 1997.
- H. Moritz. Least-squares collocation. *Reviews of Geophysics*, 16(3):421–430, 1978.
- W. Mukupa, C. Hancock, G. W. Roberts, K. Al-Manasir, H. de Ligt, and Z. Chen. Visual inspection of fire-damaged concrete based on terrestrial laser scanner data. *Applied Geomatics*, 9(3):143–158, 2017.
- R. Napolitano and B. Glisic. Methodology for diagnosing crack patterns in masonry structures using photogrammetry and distinct element modeling. *Engineering Structures*, 181(November 2018):519–528, 2019.
- G. Neri. Stahlbeton, Seifenblasen und Modelle. *Tec21*, 128(18), 2012.
- A. C. Nguyen and Y. Weinand. Displacement Study of a Large-scale Freeform Timber Plate Structure using an Electronic Total Station and a 3D Laser Scanner (under preparation). *Structural Control and Health Monitoring*, 2019.
- W. Niemeier. *Ausgleichsrechnung*. De Gruyter, Berlin, Boston, 2nd edition, 2012.
- M. Omidizarandi, J. A. Paffenholz, and I. Neumann. Automatic and accurate passive target centroid detection for applications in engineering geodesy. *Survey Review*, 51(367):318–333, 2019.
- E. Oñate. *Structural analysis with the finite element method: linear statics: volume 1: Basis and solids*. Springer Science & Business Media, 2013a.
- E. Oñate. *Structural analysis with the finite element method: linear statics: volume 2: Beams, Plates and Shells*. Springer Science & Business Media, 2013b.

- D. Oreni, R. Brumana, F. Banfi, L. Bertola, L. Barazzetti, B. Cuca, M. Previtali, and F. Roncoroni. Beyond crude 3D models: From point clouds to historical building information modeling via NURBS. *Lecture Notes in Computer Science (including subseries Lecture Notes in Artificial Intelligence and Lecture Notes in Bioinformatics)*, 8740:166–175, 2014a.
- D. Oreni, R. Brumana, S. Della Torre, F. Banfi, L. Barazzetti, and M. Previtali. Survey turned into HBIM: The restoration and the work involved concerning the Basilica di Collemaggio after the earthquake (L’Aquila). *ISPRS Annals of the Photogrammetry, Remote Sensing and Spatial Information Sciences*, 2(5):267–273, 2014b.
- Y. Ou, E. N. Chatzi, V. K. Dertimanis, and M. D. Spiridonakos. Vibration-based experimental damage detection of a small-scale wind turbine blade. *Structural Health Monitoring*, 16(1):79–96, 2017.
- R. Oval, M. Rippmann, R. Mesnil, T. Van Mele, O. Baverel, and P. Block. Feature-based topology finding of patterns for shell structures. *Automation in Construction*, 103:185–201, 2019.
- J. Pandžić, M. Pejić, B. Božić, and V. Erić. Error model of direct georeferencing procedure of terrestrial laser scanning. *Automation in Construction*, 78:13–23, 2017.
- M. Pöchtrager, G. Hochreiner, N. Pfeifer, and T. U. Wien. Processing 3D Point Clouds of Historical Timber Structures for Analysing their Structural Behaviour pressed for Time. In *23rd International Conference on Cultural Heritage and New Technologies*, 2018.
- W. Pusz and S. L. Woronowicz. Functional calculus for sesquilinear forms and the purification map. *Reports on Mathematical Physics*, 8(2):159–170, 1975.
- B. Riveiro, B. Conde, G. Drosopoulos, G. Stavroulakis, and M. Stavroulaki. Fully automatic approach for the diagnosis of masonry arches from laser scanning data and inverse finite element analysis. In *Structural Analysis of Historical Constructions – Anamnesis, diagnosis, therapy, controls*, pages 133–139. Taylor & Francis Group, 2016.
- B. Riveiro, G. Cubreiro, B. Conde, M. Cabaleiro, and R. Lindenbergh. Automated calibration of FEM models using LIDAR point clouds. *The International Archives of the Photogrammetry, Remote Sensing and Spatial Information Sciences*, XLII(June):4–7, 2018.
- R. Rolin, E. Antaluca, J.-L. Batoz, F. Lamarque, and M. Lejeune. From Point Cloud Data to Structural Analysis Through a Geometrical hBIM-Oriented Model. *Journal on Computing and Cultural Heritage*, 12(2):1–26, 2019.

- A. Sánchez-Rodríguez, B. Riveiro, B. Conde, and M. Soilán. Detection of structural faults in piers of masonry arch bridges through automated processing of laser scanning data. *Structural Control and Health Monitoring*, 25(3):e2126, 2018.
- P. Sarti, L. Vittuari, and C. Abbondanza. Laser Scanner and Terrestrial Surveying Applied to Gravitational Deformation Monitoring of Large VLBI Telescopes' Primary Reflector. *Journal of Surveying Engineering*, 135(4):136–148, 2009.
- G. Schickhofer, R. Brandner, and H. Bauer. Introduction to CLT, Product Properties, Strength Classes. *Joint Conference of COST Actions FP1402 and FP1404*, pages 1–22, 2016.
- F. J. Schill. *Überwachung von Tragwerken mit Profilsclannern*. Dissertation, TU Darmstadt, 2018.
- C. Schmitt, H. Neuner, and B. Kromoser. Geodetic surface based methods for structural analysis during construction phase. In *4th Joint International Symposium on Deformation Monitoring (JISDM)*, Athens, Greece, 2019.
- B. Schmitz, H. Kuhlmann, and C. Holst. Investigating the resolution capability of terrestrial laser scanners and its impact on the effective number of measurements. *ISPRS Journal of Photogrammetry and Remote Sensing*, 159(October 2019):41–52, 2020.
- I. Selvaggi. *Surveying and three-dimensional modeling for preservation and structural analysis of cultural heritage*. Dissertation, Università di Bologna, 2017.
- I. Selvaggi, M. Dellapasqua, F. Franci, A. Spangher, D. Visintini, and G. Bitelli. 3D comparison towards a comprehensive analysis of a building in cultural heritage. *International Archives of the Photogrammetry, Remote Sensing and Spatial Information Sciences - ISPRS Archives*, 42(2):1061–1066, 2018.
- I. Selvaggi, G. Bitelli, E. Serantoni, and A. Wieser. Point cloud dataset and FEM for a complex geometry: the San Luzi bell tower case study. *ISPRS - International Archives of the Photogrammetry, Remote Sensing and Spatial Information Sciences*, XLII-2/W11(May):1047–1052, 2019.
- E. Serantoni and A. Wieser. TLS-based Deformation Monitoring of Snow Structures. In *154. DVW-Seminar. Terrestrisches Laserscanning (TLS 2016)*, pages 89–102, Fulda, Deutschland, 2016. DVW.
- E. Serantoni and A. Wieser. Numerical structural identification using 3D laser scanning – a simulation- based case study. In *4th Joint International Symposium on Deformation Monitoring (JISDM)*, Athens, Greece, 2019.
- E. Serantoni, L. Olgiati, and A. Wieser. Terrestrische Laser-Bathymetrie mit MS50. *Geomatik Schweiz : Geoinformation und Landmanagement*, 113(10):403–406, 2015a.

- E. Serantoni, L. Olgiati, and A. Wieser. Batimetria laser terrestre con la MS50. *Geomatik Schweiz : Geoinformation und Landmanagement*, 113(10), 2015b.
- E. Serantoni, I. Selvaggi, and A. Wieser. Areal deformation analysis of a viscoplastic structure using point cloud data. In *Lienhart, W. (Hrsg.): Ingenieurvermessung 17, Beiträge zum 18. Internationalen Ingenieurvermessungskurs*, pages 403–413. VDE Verlag, 2017.
- E. Serantoni, M. Muster, and A. Wieser. Numerical structural identification of a cross-laminated timber slab using 3D laserscanning. In *European Workshop on Structural Health Monitoring*, volume 0065, 2018.
- J. Shan and C. K. Toth, editors. *Topographic Laser Ranging and Scanning: Principles and Processing*. CRC Press, Boca Raton, 2018.
- S. Soudarissanane. *The geometry of terrestrial laser scanning: identification of errors, modeling and mitigation of laser scanning geometry*. Dissertation, TU Delft, 2016.
- S. Soudarissanane, R. Lindenbergh, M. Menenti, and P. Teunissen. Incidence Angle Influence on the Quality of Terrestrial Laser Scanning Points. In *Proceedings ISPRS Workshop Laserscanning*, pages 183–188. ISPRS, 2009.
- E. Q. Sun. Shear Locking and Hourglassing in MSC Nastran, ABAQUS, and ANSYS. In *MSC software users meeting*, pages 1–9, 2006.
- P. Theiler. *Automated Registration of Terrestrial Laser Scanner Point Clouds*. Dissertation, ETH Zürich, 2015.
- E. Tonti and F. Zarantonello. Algebraic formulation of elastostatics: the cell method. *Computer Modeling in Engineering and Sciences (CMES)*, 39(3):201, 2009.
- H. Tran, K. Khoshelham, A. Kealy, and L. Díaz-Vilariño. Shape Grammar Approach to 3D Modeling of Indoor Environments Using Point Clouds. *Journal of Computing in Civil Engineering*, 33(1):1–14, 2019.
- L. Truong-Hong, D. F. Laefer, T. Hinks, and H. Carr. Combining an Angle Criterion with Voxelization and the Flying Voxel Method in Reconstructing Building Models from LiDAR Data. *Computer-Aided Civil and Infrastructure Engineering*, 28(2):112–129, 2013.
- J. Tuszynski. *Triangle/Ray Intersection*. <https://www.mathworks.com/matlabcentral/fileexchange/33073-triangle-ray-intersection>, 2019.
- UK Infrastructure and Projects Authority. Transforming Infrastructure Performance. Technical report, London, 2017.

- E. Valero, A. Adán, and F. Bosché. Semantic 3D Reconstruction of Furnished Interiors Using Laser Scanning and RFID Technology. *Journal of Computing in Civil Engineering*, 30(4):04015053, 2016.
- G. Vosselman and H. Maas, editors. *Airborne and terrestrial laser scanning*. CRC Press, Boca Raton, 2010.
- A. Wagner, W. Wiedemann, and T. Wunderlich. Fusion of Laser Scan and Image Data for Deformation Monitoring – Concept and Perspective. *INGEO - 7th International Conference on Engineering Surveying*, pages 157–164, 2017.
- Q. Wang and M.-K. K. Kim. Applications of 3D point cloud data in the construction industry: A fifteen-year review from 2004 to 2018. *Advanced Engineering Informatics*, 39(September 2018):306–319, 2019.
- Q. Wang, H. Sohn, C.-C. Chang, M.-K. Kim, J.-W. Park, and J. C. Cheng. Automated dimensional quality assurance of full-scale precast concrete elements using laser scanning and BIM. *Automation in Construction*, 72:102–114, 2016a.
- Q. Wang, H. Sohn, and J. C. Cheng. Development of a mixed pixel filter for improved dimension estimation using AMCW laser scanner. *ISPRS Journal of Photogrammetry and Remote Sensing*, 119:246–258, 2016b.
- T. Wangler, E. Lloret, L. Reiter, N. Hack, F. Gramazio, M. Kohler, M. Bernhard, B. Dillenburger, J. Buchli, N. Roussel, and R. Flatt. Digital Concrete: Opportunities and Challenges. *RILEM Technical Letters*, 1:67, 2016.
- W. M. Welsch. Advanced deformation analysis. In *Geodesy-the Challenge of the 3rd Millennium*, pages 393–399. Springer, Berlin, Heidelberg, 2003.
- W. M. Welsch and O. Heunecke. Models and terminology for the analysis of geodetic monitoring observations - Official Report of the Ad-Hoc Committee of FIG Working Group 6.1. *The 10th FIG International Symposium on Deformation Measurements*, pages 390–412, 2001.
- W. Wiedemann, A. Wagner, and T. Wunderlich. Ableitung von 3D-Verschiebungsvektoren aus fusionierten Laserscan- und Bilddaten. *AVN Allgemeine Vermessungs-Nachrichten*, 124(11-12):362–369, 2017.
- K. Worden, C. R. Farrar, G. Manson, and G. Park. The fundamental axioms of structural health monitoring. *Proceedings of the Royal Society A: Mathematical, Physical and Engineering Sciences*, 463(2082):1639–1664, 2007.
- C. C. Wu, S. Weisbrich, and F. Neitzel. Inverse Finite Element Adjustment of Material Parameters from Integrated Analysis of Displacement Field Measurement. *Materials Today: Proceedings*, 3(4):1211–1215, 2016.
- D. Wujanz. *Terrestrial Laser Scanning for Geodetic Deformation Monitoring*. Dissertation, TU Berlin, 2016.

- D. Wujanz, M. Burger, M. Mettenleiter, and F. Neitzel. An intensity-based stochastic model for terrestrial laser scanners. *ISPRS Journal of Photogrammetry and Remote Sensing*, 125:146–155, 2017.
- X. Xiong, A. Adan, B. Akinici, and D. Huber. Automatic creation of semantically rich 3D building models from laser scanner data. *Automation in Construction*, 31:325–337, 2013.
- F. Yang, Y. M. Zhu, I. E. Magnin, J. H. Luo, P. Croisille, and P. B. Kingsley. Feature-based interpolation of diffusion tensor fields and application to human cardiac DT-MRI. *Medical Image Analysis*, 16(2):459–481, 2012.
- H. Yang, X. Xu, and I. Neumann. Optimal finite element model with response surface methodology for concrete structures based on Terrestrial Laser Scanning technology. *Composite Structures*, 183:2–6, 2018.
- M. Zámečníková, A. Wieser, H. Woschitz, and C. Ressler. Influence of surface reflectivity on reflectorless electronic distance measurement and terrestrial laser scanning. *Journal of Applied Geodesy*, 8(4):311–325, 2014.
- S. Zoellig, M. Muster, and A. Themessl. Butt-joint bonding of timber as a key technology for point-supported, biaxial load bearing flat slabs made of cross-laminated timber. *IOP Conference Series: Earth and Environmental Science*, 323(1), 2019.

Curriculum Vitae

Personal data

Name and surname: Eugenio Serantoni
Date of birth: 20th of April, 1989
Place of birth: Bologna (Italy)
Nationality: Italian

Education

Feb 2015 - May 2020 ETH Zürich
Doctorate at the Institute of Geodesy and Photogrammetry
- Chair of Geosensors and Engineering Geodesy

Sep 2012 - Feb 2014 ETH Zürich
MSc in Geomatic Engineering and Planning

Sep 2011 - Jul 2014 Alma Mater Studiorum - Università di Bologna
MSc in Civil Engineering

Sep 2010 - Feb 2011 University of Southampton
Erasmus Scholarship

Sep 2003 - Oct 2008 Alma Mater Studiorum - Università di Bologna
BSc in Civil Engineering

Professional experience

Sep 2014 - Apr 2020 ETH Zürich
Research and Teaching Assistant at the Institute of Geodesy
and Photogrammetry - Chair of Geosensors and Engineer-
ing Geodesy

Mar 2014 - Jul 2014 ETH Zürich
Research and Teaching Assistant at the Institute of Geodesy
and Photogrammetry - Chair of Geodesy and Geodynamics